

Fall 2007

Design and development of microcantilever as a platform for moisture sensing

Qi Chen

Louisiana Tech University

Follow this and additional works at: <https://digitalcommons.latech.edu/dissertations>



Part of the [Chemical Engineering Commons](#), and the [Electrical and Computer Engineering Commons](#)

Recommended Citation

Chen, Qi, "" (2007). *Dissertation*. 506.

<https://digitalcommons.latech.edu/dissertations/506>

This Dissertation is brought to you for free and open access by the Graduate School at Louisiana Tech Digital Commons. It has been accepted for inclusion in Doctoral Dissertations by an authorized administrator of Louisiana Tech Digital Commons. For more information, please contact digitalcommons@latech.edu.

**DESIGN AND DEVELOPMENT OF MICROCANTILEVER AS A
PLATFORM FOR MOISTURE SENSING**

By

Qi Chen, MS

A Dissertation Presented in Partial Fulfillment
of the Requirements for the Degree
Doctor of Philosophy

COLLEGE OF ENGINEERING AND SCIENCE
LOUISIANA TECH UNIVERSITY

November, 2007

UMI Number: 3285245

INFORMATION TO USERS

The quality of this reproduction is dependent upon the quality of the copy submitted. Broken or indistinct print, colored or poor quality illustrations and photographs, print bleed-through, substandard margins, and improper alignment can adversely affect reproduction.

In the unlikely event that the author did not send a complete manuscript and there are missing pages, these will be noted. Also, if unauthorized copyright material had to be removed, a note will indicate the deletion.

UMI[®]

UMI Microform 3285245

Copyright 2007 by ProQuest Information and Learning Company.

All rights reserved. This microform edition is protected against unauthorized copying under Title 17, United States Code.

ProQuest Information and Learning Company
300 North Zeeb Road
P.O. Box 1346
Ann Arbor, MI 48106-1346

LOUISIANA TECH UNIVERSITY

THE GRADUATE SCHOOL

10/16/2007

Date

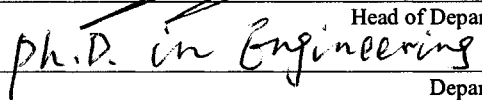
We hereby recommend that the dissertation prepared under our supervision
by Qi Chen

entitled Design and Development of Microcantilever as a Platform for Moisture Sensing

be accepted in partial fulfillment of the requirements for the Degree of
Ph.D. in Engineering



Supervisor of Dissertation Research

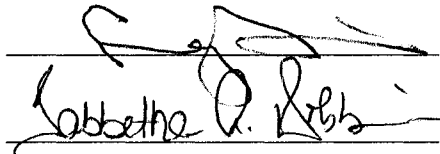


ph.D. in Engineering

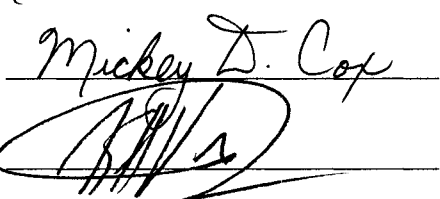
Head of Department

Department

Recommendation concurred in:




Lobbetha D. Lobb



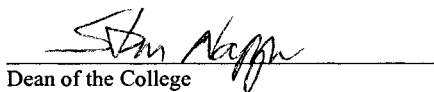
Mickey D. Cox

Advisory Committee

Approved:

Director of Graduate Studies

Approved:

Dean of the Graduate School


Dean of the College

GS Form 13a
(6/07)

ABSTRACT

Ultra-sensitive and selective moisture sensors are needed in various industries for processing control or environmental monitoring. As an outstanding sensor platform, microcantilevers have potential application in moisture detection due to their advantages, such as low-level moisture detection limits, high accuracy, quick response time, high reproducibility, good recovery rate and low in cost. Our research results will lead to the first of its kind for the commercialization of a microcantilever-based moisture sensor used for industrial and household applications. The novelty of the present work is the development of SiO_2 and Si cantilevers, which were fabricated using developed processes and modified with Al_2O_3 , for detecting moisture as low as ppm level.

To increase the deflection of the microcantilever under surface stress induced by specific reactions, a new SiO_2 microcantilever, which consists of two SiO_2 cantilever beams as the sensing and reference elements, two connecting wings and three guard arms, has been developed which features a much lower Young's modulus than conventional Si or SiN_x microcantilevers. For comparing SiO_2 cantilever with Si cantilevers, a model of the cantilever sensor is reported by using both analysis and simulation, resulting in good agreement with the experimental data. The results demonstrate that the SiO_2 cantilever can achieve a much higher sensitivity than the Si cantilever due to its lower Young's modulus. In order to fabricate this device, a new fabrication process using isotropic combined with anisotropic dry etching to release the SiO_2 microcantilever beam by Inductively Coupled

Plasma (ICP) was developed and investigated. This new process not only obtains a high etch rate at 9.1 μm per minute, but also provides good etch profile controllability, and a flexibility of device design. Attributed to its high sensitivity, Al_2O_3 coated SiO_2 microcantilevers demonstrated the capability of detecting moisture concentration levels down to 30 ppm using optical detection methods. It can be seen that the SiO_2 microcantilevers, with appropriate sensing material, can be utilized as ultra sensitive moisture sensors and are potentially able to detect the moisture concentration level as low as 1 to 10 ppm.

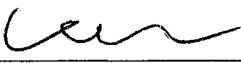
Although optical readout systems are most extensively used for measurement of cantilever deflections in labs, they have some disadvantages, such as its alignment system is expensive and involves great precision. Piezoresistive, capacitive, MOSFET-embedded and frequency readout methods, which are all fit for commercial application, have been investigated both in simulation and experiment. It is found that the Al_2O_3 modified microcantilever operating in frequency mode is able to meet the requirements of detecting low moisture levels. To make this device compatible with IC technology, the piezoelectric microcantilever is chosen as the platform for moisture sensing. A piezoelectric microcantilever vibrates at its resonant frequency upon applying an appropriate AC voltage and provides an electrical signal at the output via piezoelectric coupling, which can be fed back through the phase shift loop to determine the change in resonant frequency caused by any change in mass. In order to fabricate the piezoelectric microcantilever, the sputtering parameters for ZnO were reported and investigated. The piezoelectric microcantilevers, which consists of bottom electrode, ZnO piezoelectric layer, and two separate top electrodes as sensing and actuation elements, were designed

and fabricated using a standard lithography process. Its resonant frequency shift is measured at 1.25 Hz/ppm, based on an optical detection method. Although both SiO₂ and Si piezoelectric cantilevers were fabricated successfully, the latter are more likely to be used in dynamic mode because of the higher fragility of SiO₂. The developed cantilever sensor platform operating in dynamic mode, which can be integrated with on-chip electronic circuitry, is able to provide ultra-sensitive detection, not only for moisture sensing, but also for chemical and biological sensing with appropriate surface modification.

APPROVAL FOR SCHOLARLY DISSEMINATION

The author grants to the Prescott Memorial Library of Louisiana Tech University the right to reproduce, by appropriate methods, upon request, any or all portions of this Dissertation. It is understood that "proper request" consists of the agreement, on the part of the requesting party, that said reproduction is for his personal use and that subsequent reproduction will not occur without written approval of the author of this Dissertation. Further, any portions of the Dissertation used in books, papers, and other works must be appropriately referenced to this Dissertation.

Finally, the author of this Dissertation reserves the right to publish freely, in the literature, at any time, any or all portions of this Dissertation.

Author 

Date 10/16/2007

TABLE OF CONTENTS

ABSTRACT.....	iii
TABLE OF CONTENTS	vii
LIST OF TABLES	x
LIST OF FIGURES	xi
ACKNOWLEDGEMENTS.....	xvii
CHAPTER ONE INTRODUCTION.....	1
1.1 Classification of Moisture Sensors	3
1.2 History of Moisture Sensor.....	5
1.3 Commercial Moisture Sensors.....	12
1.4 A Platform for Moisture Sensor - Microcantilever	15
1.5 Research Objective and Dissertation Outline	16
CHAPTER TWO MICROCANTILEVER AS A SENSOR PLATFORM	18
2.1 Microcantilever.....	18
2.2 Operation Mechanism of Microcantilever	19
2.2.1 Dynamic Mode.....	20
2.2.2 Static Bending Mode.....	23
2.3 Common Readout Schemes of Microcantilever	24
2.3.1 Optical method.....	24
2.3.2 Piezoresistive method	26
2.3.3 Piezoelectric method.....	27
2.3.4 Capacitive method	28
2.3.5 MOSFET-Embedded method.....	29
2.4 Summary	30
CHAPTER THREE SIMULATION AND INVESTIGATION OF READOUT METHOD FOR MICROCANTILEVER AS A MOISTURE SENSOR	32
3.1 Simulation of SiO ₂ Microcantilever for Optical Method	32

3.1.1 Theoretical Analysis.....	33
3.1.2 Simulation Results	35
3.2 Investigation of Piezoresistive Readout Method	37
3.2.1 FEM analysis	37
3.2.2 Simulation Results and Discussion.....	38
3.3 Investigation of MOSFET-Embedded Readout Method.....	40
3.3.1 Mathematic Model.....	40
3.3.1.1 Stress-Induced Bandgap Change	40
3.3.1.2 Stress-Induced Mobilities Change	41
3.3.2 Results and Discussion	43
3.3 Investigation of Frequency Mode	49
3.3.1 Experimental Investigation.....	49
3.3.2 Simulation Investigation	51
CHAPTER FOUR ISOTROPIC ETCH WITH ICP FOR MICROCANTILEVER RELEASE	54
4.1 Introduction.....	54
4.1.1 Vapor phase dry etching without plasma.....	54
4.2 Configuration and principle of ICP operation system	57
4.3 Scanning Electron Microscopy	58
4.4 Experimental Setting.....	60
4.5 Results and Discussion	64
4.5.1 Chamber Pressure	65
4.5.2 ICP source power	67
4.5.3 Substrate power.....	68
4.5.4 SF ₆ flow rate	69
4.5.5 Comparison with traditional RIE.....	70
4.6 Isotropic Etch Summary	71
CHAPTER FIVE DESIGN AND MICROFABRICATION OF SiO ₂ MICROCANTILEVER SENSORS.....	73
5.1 Introduction.....	73
5.2 Microfabrication Facilities and Process.....	74
5.2.1 Mask Design and Fabrication	74
5.2.2 Photolithography.....	75
5.2.2.1 Photolithography Introduction.....	75
5.2.2.2 Resolution in Photolithography	79
5.2.3 ICP Etching.....	81
5.2.4 Thin Film Deposition and Lift-off	81
5.2.4.1 Thin Film Deposition.....	81
5.2.4.2 Lift-off.....	84
5.3 Design and Microfabrication of SiO ₂ Cantilever.....	88
5.3.1 SiO ₂ Microcantilever Introduction.....	88
5.3.2 SiO ₂ Microcantilever Design	89
5.3.3 SiO ₂ Microcantilever Fabrication.....	89

CHAPTER SIX MEASUREMENT OF SiO ₂ MICROCANTILEVER AS MOISTURE SENSORS.....	95
6.1 Measurement Equipment	95
6.2 Control Experiment.....	96
6.3 Moisture Measurement	97
6.3.1 Ethyl Acetate Modified SiO ₂ Microcantilever	97
6.3.2 Aluminum Oxide Modified SiO ₂ Microcantilever	98
6.3.2.1 Experiment Design.....	98
6.3.2.2 Results and Discussion	100
6.4 Conclusion	104
CHAPTER SEVEN DESIGN, FABRICATION AND TESTING OF PIEZOELECTRIC MICROCANTILEVER AS A MOISTURE SENSOR.....	105
7.1 Piezoelectric Zinc Oxide.....	106
7.1.1 Theory of Piezoelectricity.....	106
7.1.2 Piezoelectricity of ZnO	107
7.1.3 ZnO Thin Film Deposition.....	107
7.2 Design and Fabrication of Piezoelectric Microcantilever.....	109
7.2.1 Design of Si Piezoelectric Microcantilever	109
7.2.2 Fabrication of Si Piezoelectric Microcantilever	110
7.2.2 Fabrication of SiO ₂ Piezoelectric Microcantilever	118
7.3 Results.....	119
7.3.1 Fabrication Results.....	119
7.3.2 Experimental Results and Discussion.....	120
CHAPTER EIGHT CONCLUSION AND FUTURE WORK	123
8.1 Conclusions.....	123
8.2 Future Work	124
8.2.1 Future Application of ICP Isotropic Dry Etching	124
8.2.1.1 Metal Microcantilever Fabrication	124
8.2.1.2 Capacitive Microcantilever Fabrication.....	127
8.2.2 Future Work of Moisture Sensor Project	130
REFERENCE.....	131

LIST OF TABLES

Table 1.1 Commercial Moisture Meters	13
Table 3.1 Piezoelectric microcantilever layers design for simulation	52
Table 3.2 Simulation results of different cantilever beam thickness	53
Table 4.1 Process parameters and etching profiles.	66
Table 7.1 Elemental composition of Zn and O in the thin film	109
Table 7.2 Parameters in RIE system for buried SiO ₂ layer etching	118
Table 7.3 Comparison of moisture sensing between our microcantilever and commercial microcantilever.....	122
Table 8.1 Simulation results of capacitance microcantilever.....	127

LIST OF FIGURES

Figure 2.1 Different types of microcantilevers (top view) (a) Rectangular (b).....	18
Figure 2.2 Schematic representation of a chemical or biological sensor based on the microcantilever, whose mechanical characteristic can be changed in response to the presence of a target analyte.	20
Figure 2.3 Schematic of an optical detection system for detecting microcantilever deflection.	25
Figure 2.4 The Wheatstone Bridge Circuit used for the piezoresistive microcantilever.	27
Figure 2.5 Schematic of the interaction between probe and target molecules on an embedded-MOSFET cantilever system. The silicon nitride cantilever is a reference, and the gold-coated one is used as a sensing cantilever. Specific biomolecular interactions between receptor and target bend the cantilever. A magnified view of the embedded MOSFET in cross section shows the stressed gate region when the cantilever bends, resulting in a change in drain current due to conductivity modulation of the channel underneath the gate.....	30
Figure 3.1 Scheme diagram for theoretical analysis.....	35
Figure 3.2 The deflection contour of cantilever beam. (a) SiO ₂ . (b) Si.	36
Figure 3.3 Schematic diagram of a Silicon piezoresistive microcantilever.	37
Figure 3.4 The sensitivity as a function of deflection of the cantilever beam with different beam thickness (a) 1μm (b) 0.75μm (c) 0.5μm (d) 0.25μm and different piezoresistor thickness.....	39
Figure 3.5 Sensitivity as a function of thickness of the cantilever beam corresponding to different force.	39
Figure 3.6 Sensitivity as a function of thickness of the piezoresistor corresponding to different force.	39
Figure 3.7 (a) MOSFET structure, (b) I _d -V _d curve, (c) I _d -V _g curve.....	44

Figure 3.8 The whole MOSFET with length =100 μ m, substrate doping concentration =1e17, source-drain doping concentration =1e20, junction depth =0.2 μ m, and drain voltage =3.0V. (a) Drain current as a function of channel length, (b) Change of Drain current as a function of channel length.....	45
Figure 3.9 The whole MOSFET with length =10 μ m, channel length =5 μ m, substrate doping concentration =1e17, junction depth =0.2 μ m, and the drain voltage =3.0V. (a) Drain current as a function of Source-Drain doping concentration, (b) Change of Drain current as a function of Source-Drain doping concentration.....	45
Figure 3.10 The whole MOSFET with length =10 μ m, channel length =5 μ m, source-drain doping concentration =1e20, junction depth =0.2 μ m, and the drain voltage =3.0V. (a) Drain current as a function of substrate doping concentration. (b) Change of Drain current as a function of substrate doping concentration.....	46
Figure 3.11 The whole MOSFET with length =10 μ m, channel length =5 μ m, source-drain doping concentration =1e20, substrate doping concentration =1e17, and the drain voltage =3.0V. (a) Drain current as a function of junction depth; (b) Change of Drain current as a function of junction depth.....	46
Figure 3.12 The whole MOSFET with length =10 μ m, channel length =5 μ m, substrate doping concentration =1e17, source-drain doping concentration =1e20, junction depth =0.2 μ m, and the drain voltage =3.0V, (a) Drain current as a function of applied stress. (b) Change of Drain current as a function of applied stress.....	47
Figure 3.13 The whole MOSFET with length=10 μ m, channel length =5 μ m, substrate doping concentration =1e17, source-drain doping concentration =1e20, junction depth (Y) =0.2 μ m, and the drain voltage =3.0V, (a) Drain current as a function of MOSFET Width (Z direction); (b) Change of Drain current as a function of MOSFET Width (Z direction).....	47
Figure 3.14 I_d - V_g curve.....	48
Figure 3.15 Drain current change mentioned by (a) T. Chen et al; (b) R. C. Jaeger et al.	49
Figure 3.16 Block Diagram of the micro cantilever based Moisture Sensor.....	50
Figure 3.17 Al modified Au/Si/Au cantilever II using anodization method shows the presence of spontaneous and stable decrease in resonant	

frequency to the randomly injected moisture levels. Initial Frequency: 25475 Hz; Final Frequency: 25025 Hz; 450 Hz change in resonance frequency at 200 ppm level of injected moisture.	51
Figure 3.18 (a) Beam structure of the piezoelectric microcantilever; (b) Magnified part of cantilever beam.....	52
Figure 4.1 A schematic representation of a XeF ₂ Vapor Phase etching system.	56
Figure 4.2 Alcatel system 601E.....	58
Figure 4.3 Schematic view of Alcatel system 601E process module.....	58
Figure 4.4 Schematic illustration of the SEM [54]......	59
Figure 4.5 Schematic diagram of Bosch etch process.	61
Figure 4.6 Mask pattern used to produce microcantilever beams.	62
Figure 4.7 The process sequence for the experiment. (a) Resist lithography (b) BOE etching (c) Resist lithography for cantilever beam release (d) Isotropic etching for 10 minutes.....	63
Figure 4.8 SEM images of the cross section of etched trenches. The mask opening was 200 μm in width, and the etching time was 600s. (a) A trench near the center of the wafer. (b) A trench at the edge of the wafer. The parameters of the etching process were as follows: Pressure = 46 mTorr, Source Power = 1800 W, Substrate Power = 20 W, SF ₆ = 300 standard cubic centimeters per minute (sccm).	64
Figure 4.9 SEM image of the released cantilever beams.....	65
Figure 4.10 Silicon isotropic etching profiles as a function of pressure: (a) Etch rate. (b) Undercut rate. (c) Isotropic ratio. The source power and substrate power were set to 1800 W and 30 W, respectively. The SF ₆ flow rate was set to 300 sccm.....	67
Figure 4.11 Silicon isotropic etching profiles as a function of plasma source power: (a) Etch rate. (b) Undercut rate. (c) Isotropic ratio. The pressure, substrate power, and SF ₆ flow rate were set to 46 mTorr, 30 W, and 300 sccm, respectively.....	68
Figure 4.12 Silicon isotropic etching profiles as a function of substrate power: (a) Etching rate. (b) Undercut rate. (c) Isotropic ratio. The chamber pressure, source power, and SF ₆ flow rate were set to 46 mTorr, 1800 W, and 300 sccm, respectively.....	69

Figure 4.13 Silicon isotropic etching profiles as a function of SF ₆ flow rate: (a) Etch rate. (b) Undercut rate. (c) Isotropic ratio. The chamber pressure, source power, and SF ₆ flow rate were held constantly at 46 mTorr, 1800 W, and 300 sccm, respectively.....	70
Figure 5.1 Schematic of photolithography process.....	77
Figure 5.2 Modes of photolithography. (a) contact printing mode (b) proximity printing mode (c) project printing mode.	81
Figure 5.3 Simplified diagram of an RF magnetron sputter system. Electrons collide with gas atoms causing the atoms to ionize. These ionized atoms then bombard the target and dislodge target atoms which travel as vapor to the substrate or any other surface before condensing and forming a film.	84
Figure 5.4 LOR lift-off process	87
Figure 5.5 Schematic diagram of the novel SiO ₂ microcantilever design	89
Figure 5.6 Pattern of the PR (photoresist) as a mask for cantilever beam release.....	90
Figure 5.7 Process flow for SiO ₂ microcantilever fabrication. (a) Pattern SiO ₂ microcantilever beam by BOE etching (b) Pattern the guide arm by ICP etching (c) Pattern the connecting wing by ICP etching (d) Microcantilever beam released by ICP isotropic etching.....	91
Figure 5.8 SEM image of rectangular cantilever beam.	93
Figure 5.9 Rectangular microcantilever array	93
Figure 5.10 SEM image of SiO ₂ microcantilevers.....	94
Figure 6.1 Measurement setup based on optical methodology.....	96
Figure 6.2 The bending response of the SiO ₂ and Si microcantilevers upon exposure to a 10 ⁻⁵ M solution of aminoethanethiol in ethanol.....	97
Figure 6.3 The response of cantilever beam coated with a layer of ethyl acetate to relative humidity of 1%.....	98
Figure 6.4 Deflection of Al ₂ O ₃ modified microcantilevers versus time at various moisture level in nitrogen at 30 °C. The gas flow rate was 100 mL/min. Insert: Deflection of the microcantilevers versus time after repetitive exposure to 30 ppm moisture in nitrogen.....	101

Figure 6.5 Deflection amplitude of Al ₂ O ₃ modified microcantilevers versus the concentration of moisture in nitrogen.	101
Figure 6.6 Deflection of Al ₂ O ₃ modified microcantilevers versus time upon exposure to 200 ppm of moisture in nitrogen at different temperatures. The flow rate was 100 mL/min.	102
Figure 6.7 Deflection of Al ₂ O ₃ modified microcantilevers versus time upon exposure to 100 ppm of moisture, 100 ppm of alcohol, 100 ppm of moisture, and 100 ppm moisture + 100 ppm of alcohol in nitrogen at 40 °C, respectively. The flow rate was 100 mL/min.	103
Figure 7.1 Piezoelectricity in an ionic crystal.....	106
Figure 7.2 The Hexagonal wurtzite crystal Structure of ZnO. The large red atoms are zinc atoms while the smaller purple atoms are oxygen atoms.	107
Figure 7.3 The SEM image of ZnO thin film	108
Figure 7.4 The EDX analysis spectrum	109
Figure 7.5 The schematic diagram of the piezoelectric microcantilever design.....	110
Figure 7.6 The process began with an SOI wafer. Both sides of the wafer have been thermally oxidized and patterned using the BOE process.....	111
Figure 7.7 Bottom electrode (Cr/Pt layer) was patterned by lift-off process.....	112
Figure 7.8 ZnO thin film was sputtered on the wafer and patterned to form the piezoelectric layer. Afterwards, Cr/Pt were sputtered on the wafer and patterned by the lift-off process to form the top electrode.	114
Figure 7.9 SiO ₂ and SiN were deposited on the wafer and patterned by BOE etching to insulate the top electrode from the sensing Alumina layer. Next, Al was deposited on the wafer and patterned by the lift-off process.	115
Figure 7.10 Top silicon layer was patterned by ICP etching, in which photoresist served as mask, to form microcantilever beam.	116
Figure 7.11 Silicon substrate was deeply etched in ICP system by utilizing Cr as a mask until reaching the buried SiO ₂ etching stop layer.	117
Figure 7.12 The buried SiO ₂ layer was etched by RIE using CF ₄ and H ₂ to eventually release the silicon cantilever beam.	118

Figure 7.13 Top view of mass-produced SiO ₂ piezoelectric microcantilevers taken by Canon digital camera.	119
Figure 7.14 Top view of SiO ₂ piezoelectric microcantilever beam prior to backside release taken by Sony microscope.	120
Figure 7.15 SEM images of the fabricated SiO ₂ piezoelectric microcantilevers. (a) a top-down view (b) a side view.	120
Figure 7.16 Experimental setup of moisture detection system measuring moisture absorption in terms of cantilever deflection.	121
Figure 8.1 Fabrication process for Metal Microcantilever.	126
Figure 8.2 The change rate of capacitance as a function of deflection of microcantilever beam.	128
Figure 8.3 Fabrication process for capacitive microcantilever.	129

ACKNOWLEDGEMENTS

I am very grateful to my dissertation advisor, Dr. Haifeng Ji, for his guidance, encouragement, and support throughout these years at Louisiana Tech University. He not only taught me scientific working style and research skill, but also strict and meticulous scholarship. I am also grateful to Mr. Ji Fang and Dr. Kody Varahramyan, my co-advisors, for their support and insightful direction in my research. Deep gratitude is also for Dr. Tabbetha Dobbins and Dr. Mickey Cox, for their helpful advice and serving on the advisory committee for this dissertation. I sincerely acknowledge Sensidyne Inc. for funding this project and Mr. Wes Davis for his co-operation and support.

I would like to thank all the faculty and staff in the Institute for Micromanufacturing at Louisiana Tech University, especially Mr. Abdul Khaliq, Mr. Donald Tatum, Dr. Alfred Gunasekaran and Dr. Karen Xu, who helped me with simulation, e-beam evaporation, sputtering and metrology instruments.

I thank my research group members, Liu Pan, Xiaolei Shi, Prathima Kapa, Ming Wang, Weisong Wang, Venkata Chivukula, Santosh Mutyala, Deepika Bandhanadham, Pengjun Yao and Xin Yang, for their co-operation and continuous support.

This dissertation is also a present for my family. I thank my wife Yan Liu and my sweetest son Daniel for their everlasting and unconditional support and love. I thank my parents and my brothers for their long-standing love and education.

CHAPTER ONE

INTRODUCTION

In recent years, moisture sensors have been widely used for measurement and control in industrial and household environments. The sensing and control of moisture is very important in various areas and processes of industries such as chemical, petrochemical, food processing, agriculture, textile industries, etc., as the presence of moisture is highly undesirable and deteriorates the quality of the product. The amount of moisture determines the market value of a moisture-sensitive product and the manufacturing and processing costs [1]. For manufacturing highly sophisticated integrated circuits in semiconductor industry, humidity or moisture levels are constantly monitored in wafer processing. There are many domestic applications, such as intelligent control of the living environment in buildings, cooking control for microwave ovens, and intelligent control of laundry etc. In the automobile industry, moisture sensors are used in rear window defoggers and motor assembly lines. In the medical field, moisture sensors are used in respiratory equipment, sterilizers, incubators, pharmaceutical processing, and biological products. In agriculture, humidity sensors are used for green-house air-conditioning, plantation protection (dew prevention), soil moisture monitoring, and cereal storage. In general industry, moisture sensors are used for humidity control in chemical gas purification, dryers, ovens, film desiccation, paper and textile production, and food processing [2].

Industrial gas manufacturers monitor moisture content to meet industry specifications for pure, dry gas. Moisture can appear almost anywhere and is hard to measure with a high degree of accuracy. The accuracy of the best moisture analyzers, for example, does not approach that of an oxygen analyzer. Semiconductor manufacturers control moisture down to the low parts-per-billion (ppb). Probably more important than accuracy is consistency, or reproducibility. All moisture analyzers work slowly by nature [3].

The choice of analyzer typically depends on a particular need which includes maintenance of H₂O in the final product gas consistently at 5 ppm, need to test the exact concentration of H₂O in gas, a need for relatively fast results with reasonable accuracy, a need for a trade off of high accuracy for a lower price or lower operating costs. The effects of moisture in various gases are enumerated below:

For Specialty Gases:

Errors can occur during analysis when the carrier gas has high moisture content.

Columns and detectors in the instruments may be damaged or degraded prematurely by moisture.

Moisture traps must be replaced prematurely.

Loss of end products results when process gases or blanketing gases have high moisture content.

Moisture may react with components in the gases, resulting in false analyses.

For Medical Gases:

Out-of-spec product results when moisture levels are too high or too low.

Reactions with minor components in medical mixtures, such as blood gas or lung diffusion calibration gases and medical monitor calibration gases.

1.1 Classification of Moisture Sensors

The moisture meter or moisture sensor is an electronic instrument used to detect and determine the water content. It consists of a sensor element, an electronic section for conditioning of the signal and a sensor readout section for display or storage of the signals. Moisture sensors can be broadly classified according to the operating principle, the type of sensor used and the electronic measurement system they employ. Three important categories are as follows: sensor based on capacitive change, sensor based on resistance change and the sensor based on optical reflectometry [4].

The capacitive-type moisture sensor is based on a variation of the dielectric constant of the hygroscopic organic material upon absorption of moisture on its surface [4]; a resistive-type moisture sensor detects the moisture by measuring the change in resistance of an element corresponding to the relative humidity. The sensory elements in these types of sensors are usually highly moisture-sensitive materials and are, generally, electrolytic or polymeric or metallic substances. Polyimide is an example of material used in capacitive- type moisture sensor elements [4].

Irrespective of the type of moisture sensor element, the principle involved in the interaction of water molecules with the moisture sensitive material of a sensor can be explained as follows:

At the oxide surface of the moisture sensitive material, metal ions and OH⁻ ions bond together. This bonding results in the formation of a chemically adsorbed layer on the surface. Water molecules are attached to the surface by physical adsorption phenomenon. The continuous adsorption of water molecules builds up a multilayer on the surface.

Water molecules adsorbed on the surface further result in condensation into the pores of the moisture sensitive material. [5]

This condensed water molecules in the pores of the sensing material causes a change in the resistance of the material, a change in the capacitance or even a change in the mass of the material [5].

The response of the capacitive-type sensor is highly non-linear to changes in the moisture, and the sensory elements used, like polymers, are temperature-sensitive and cannot operate in uneven environments [5].

The third kind of moisture sensor uses the principle of optical reflectometry. It works on the principle that each molecule absorbs the incident light at a particular wavelength. Water molecules in the sensing environment absorb the wavelength emitted by incident light. This absorption of light gives an absorption spectrum for the water molecules [5].

Rapid advancements in semiconductor technology, such as thin film deposition, ion sputtering, and ceramic/silicon coatings, have made it possible to fabricate highly accurate moisture sensors with resistance to chemicals and physical contaminants—at economical prices. No single sensor, however, can satisfy every application. Resistive, capacitive, and optical reflectometry sensing technologies each offer distinct advantages. Resistive sensors are interchangeable, usable for remote locations, and cost effective. Capacitive sensors provide wide RH range and condensation tolerance, and, if laser trimmed, are also interchangeable. Optical reflectometry sensors perform well in corrosive environments and at high temperatures. For most applications, therefore, the environmental conditions dictate the sensor choice.

1.2 History of Moisture Sensor

Until the mid 1940s, the primary method used to detect and analyze moisture content was the *volumetric Karl Fischer (KF) titration* for determining free water and water of hydration in most solid or liquid organic and inorganic compounds. This test method is used with automatic titration systems capable of determining the KF titration end point amperometrically. However it is a complex and time-consuming method and does not lend itself to applications that require continuous analysis.

Two basic principles of moisture analysis have been established:

Physical State or Dew Point.

Mole Fraction measurements (e.g., percent, ppm, ppmb): Mole fraction of a gas in a gas mixture is just the number of moles of that gas divided by the total number of moles of all gases in the mixture. For specialty and medical gas industries, mole fraction is the preferred choice.

In the mid 1940s, the *Dew Point Hygrometer*, the chilled mirror instrument, was introduced. Also known as the Bureau of Mines method, it is relatively a simple device and gives primary or absolute measurements. A gas stream flows across a temperature-controlled surface, usually a gold-plated mirror. As the temperature is lowered, the water vapor begins to condense on the mirror surface. This condensation of water vapor is defined as the dew point. In some instruments, an optical sensor detects the dew; in others, it is determined by the operator. Conversion tables can be used to convert dew point to moisture content for a given instrument. The mirror can then be heated, to eliminate all traces of moisture, and the process repeated.

Advantages:

An absolute measurement of moisture content

Recognized transfer standard for National Laboratories

Disadvantages:

Poor accuracy and reproducibility

Non-continuous measurement

Not suited for dirty or corrosive gases, which contaminate the mirror surface

High cost and high maintenance

Need to convert the dew point to volume, which is a nonlinear relationship

There is no simple formula

A few years later, *electrolytic cells* were introduced. These are sensors based on materials, such as phosphorous-pentoxide (P_2O_5) absorbing water and breaking it down to H_2 and O_2 by electrolysis. Sensors measure moisture content according to Faraday's Law, which postulates that 13.2 mA of current equals one ppm of water. These early instruments had externally wound sensors and relied on the moisture reaching equilibrium. As such, they gave relative, rather than absolute measurements, needed calibration and conversion factors from current to moisture content. Because the sensors are in contact with the sample gas, they require a high volume of flow to operate efficiently.

In a paper presented on February 27, 1956 at the Pittsburgh Conference, F.A. Keidel of the DuPont Engineering Research Laboratory described an instrument developed at DuPont that could continuously measure traces of moisture at sub ppm levels by absorbing and electrolyzing the water in a sample stream and converting the electrolysis into a current directly proportional to the moisture concentration. The key component

was a Teflon cell, coated with phosphorous-pentoxide (P_2O_5), which electrolyzed water to H_2 and O_2 . The main feature of this cell was that it produced electrical response only to the electrolysis of water but was inert to other contaminants in the gas stream. It can remove even small amounts of water from the sample. Since the sensor is internal to the cell, it is considered a primary or first principle measurement. This principle, with improvements in cell design and temperature control, is applied in many instruments today.

Advantages:

Relatively low cost

Suitable for online and continuous measurement

Water-vapor specific

Highly repeatable

Self-drying

Broad range capabilities

If internally wound sensor, does not require calibration

Disadvantages:

Free H_2 and O_2 in the sample can recombine, causing measurement error

Needs accurate flow control

High moisture levels may overload the sensor

Very dry gas may destroy the P_2O_5 coating

Some types of electrolytic cells are not compatible with reactive and corrosive gases

Some types of electrolytic cells cannot give accurate measurement of moisture in H_2 or O_2

Also in the 1950s, the *Thin Film Oxide Sensor* was developed. The first material used was aluminum oxide. Silicon was used later as well. It works on the principle that a thin film oxide layer and a very thin gold layer evaporated over it form a capacitor. As water vapor is transported through the gold layer and equilibrates in the oxide layer, the dielectric constant changes and the change in capacitance is related to the moisture concentration.

Advantages:

Low cost

Compatible with most gases

Fast response at high moisture levels

Disadvantages:

Rapid changes in sample pressure can cause electrode delamination

Changes in oxide thickness due to aging may cause inaccuracies

Some thin film oxide sensors are temperature sensitive

Most sensors need periodic sensor recalibration from generated standards

Sensitive to contamination

A later development is the *Quartz Crystal Microbalance and Silicon chip (QCM)* sensors. A quartz crystal is sensitized with a thin coating of hygroscopic material and enclosed in a small chamber. As the crystal is exposed to the gas stream, the coating absorbs or desorbs moisture. Variations in the coating alter the oscillation frequency of the crystal, proportional to the change in moisture concentration. A similar analyzer is based on a silicon chip sensor.

Advantages:

High sensitivity

Fast response time

Broad-range capabilities (ppb to percent)

Can handle high flow rates (flow independent)

Self-controlled pressure

Disadvantages:

Not a primary or first principle device

Relatively high cost

Slow recovery rate

Needs factory calibration and calibration cycle to verify readings

Cannot handle highly corrosive or reactive samples

In the 1980s and 1990s, *optical devices*, primarily IR and FTIR, came into wider use for measurement of low moisture concentrations in gases. The principle is simple: infrared light is absorbed by water molecules in proportion to their concentration in the sample.

Advantages:

A primary or first principle device

The sample does not contact the sensor, so moisture content in highly corrosive and reactive gases can be measured

Very selective, fast response time

High accuracy, plus or minus five percent or better

Disadvantages:

- High cost

- Background moisture in the optical system can cause errors
- Sample pressure dependent
- Temperature dependant
- Needs calibration standard for verification
- Possible interference from other components that absorb at same frequency as H₂O

Tunable Diode Laser Sensors are a variation on optical sensors. This instrument utilizes multiple reflections in the cell using mirrors to increase the path length, and thus achieving greater sensitivity. Measurement is based on Beers Law, and frequent recalibration is not required.

Advantages:

Fast response time

Low detection levels

Compatible with corrosive and reactive gases

Disadvantages:

High cost

High maintenance

Must be selective with sample gas

The *cavity ring-down laser*, one of the newest developments in moisture measurement technology, is a primary measurement device. A short light pulse is coupled to a stable optical cavity formed by two highly reflective mirrors. The fraction of light entering the cavity on one side rings back and forth between the mirrors. Recorded light loss is due to the presence of light absorbing or scattering molecules, in this case H₂O.

Advantages:

Primary or absolute measurement device

Requires no calibration

Measurement is relatively fast, as the sensor does not need to be in contact with the gas

Very low detection levels

Disadvantages:

High cost

Sensitive to mirror contamination and alignment

Can measure moisture in some corrosive and reactive gases but not all

Length-of-stain tubes occupy the low end of this technology. These types of Cavity Ring-Down Laser Sensors (commonly called detector tubes) are manufactured by a number of companies. Their value is that, if we suspect we have a gross error in our H₂O measurements whether due to instrument failure or defective sampling system, this is a quick, low cost, and easy way to confirm it. But these are not analytical devices [5].

With advances in material and microelectronic technology advancing rapidly, manufacturers are finding ways to overcome the disadvantages inherent in these sensors. Microcantilever technology is one of such ways to develop a moisture sensor with low-level moisture detection limits, high accuracy, quick response time, high reproducibility, good recovery rate and low in cost.

In recent years, the micromechanical cantilever has proven to be a potential sensor in wide variety of platforms such as industrial, environmental, pharmaceutical, biomedical, etc.

Research shows that the cantilever can be potentially used as a chemical sensor, biosensor, DNA sensor, etc., when its surface is modified with a suitable material [6].

1.3 Commercial Moisture Sensors

Several companies are supplying moisture meters for the measurement of moisture in solid, liquid and gaseous applications [7]. The detection limit of all these moisture meters ranges from 0-100% relative humidity. The change in detection is because of changes in capacitance, resistivity and permittivity of the sensing materials with absorbed moisture content.

Table 1.1 shows moisture meters manufactured by some companies whose application is mainly in the natural gas field [7].

Several commercial moisture meters are available in market for the measurement of moisture in solid, liquid and gaseous applications. The detection limit of all these moisture meters ranges between 0-100% relative humidity. But, these commercial moisture meters need an improvement in sensory element lifetime, stability in corrosive environment and selectivity to only moisture, when compared to other alcohols and hydrocarbons.

Table 1.1 Commercial Moisture Meters

No	Name	Comp.	Environment	Level	Methods	Response
1	Cermax IS Portable Dewpointmeter	Michell Instruments Ltd, (UK)	petrochemical gas natural gas hazardous area	0.01ppm		A few mins.
2	Promet Process Moisture Analyzer	Michell Instruments Ltd, (UK)	Natural gas			
3	HMT360	Vaisala (Finland)		ppm	Polymer	
4	GMS2100	BIG DIPPER TECH- NOCHEM INSTITUTE		RH:0-100% AH: to 550ppm 25°C		15 secs.
5	AT2123	BIG DIPPER TECH- NOCHEM INSTITUTE	Chemical industry	ppb-1000ppm	Thin film polymer (<70°C)	15 secs.
6	AT2110	BIG DIPPER TECH- NOCHEM INSTITUTE	Chemical industry	ppb-1000ppm	Aluminum-Oxide(>180°C)	2 secs.
7	T_LMSA4814WMF	BIG DIPPER TECH- NOCHEM INSTITUTE	higher chemical multi-gases	0-10~1000ppm	double beam photometer	1 sec.

8	MTO-1001-H2O Patent U.S. Patent # 5,528,040 U.S. Application # 09/998,518	Tiger Optics, LLC.	Inert, Passive, Toxic, and Corrosive Gases	0-5000ppb sensitivity:100ppt	light absorption in accordance with Beer's Law: attuning light rays to the unique molecular fingerprint By measuring the time it takes the light to fade or "ring-down", you receive an accurate molecular count in milliseconds.	50ppb<3mins.
9	ESS-SCVP	Xentaur	Natural gas	1-140ppm	aluminum oxide	
10	SS2000 SS1000 SS3000 SS500	Spectrasensors	Natural gas	10-422ppm	The sensor sends a beam of light through a window in the sample cell and analyzes the resulting changes (absorption) in the beam energy.	4 times/s aver. the results
11	Series400 Series500	Illinois Instrument	Natural gas	0-1000ppm	aluminum oxide phosphorus pentoxide (P2O5)	
12	MP300	Galvanic Applied Sciences Inc.	Natural gas	RH:0-100%	thermoset polymer capacitive sensor	15-60secs.
13	3050 OLV	AMETEK PROCESS INSTRUMENTS	industrial gases	0.1-2500ppm		

1.4 A Platform for Moisture Sensor - Microcantilever

In the last decade, emerging MEMS technology and micromachining techniques have been popular in the miniaturization of sensors. As a result of this technology, new sensing instrumentation has now been developed which is capable of accessing information at a micro-scale level. Importantly, the functionality and reliability of these micro sensors can be increased through their integration with mature logic IC technology and with other sensors.

Microcantilevers have proven to be an outstanding sensor platform for extremely sensitive chemical, biological and environmental sensors [8]-[16]. In general, microcantilever technology has several advantages, besides high sensitivity, which has been confirmed using a commercially available silicon micro-cantilever (200 μ m in length, 1 mm in thickness, Digital instruments) which can respond to a force as low as 10^{-18} N [17]. The entire sensor could fit in an area less than a few millimeters. Because the cantilever bending signal is driven by molecular recognition, the only power required is for the detection and display, allowing use of light-weight battery power or photovoltaic cells [18]. Electronics for operation and control are relatively simple and inexpensive. Microcantilever arrays could be used to record numerous properties, gain specificity and provide replication [19]. The microcantilever moisture sensor, that incorporates a microcantilever coated on one side with a water-absorbent layer, is attracting more and more interest. It has demonstrated a great potential for high sensitivity, high linearity and high stability. In humid conditions, water is absorbed by this layer and this causes a change in the cantilever mass or in the surface stress, from which the humidity may then be determined. This device is attractive since it is capable of providing highly precise humidity sensing results despite its diminutive dimensions. Therefore, developing a high sensitivity moisture sensor based on microcantilevers will

have promising applications in the chemical, petroleum and transportation industries.

In our work, the silicon dioxide (SiO_2) microcantilever, which can provide a much higher mechanical sensitivity compared to its silicon or silicon-nitride counterparts, has been applied to detect moisture concentration for the first time. Although some cantilever-based moisture sensors have already been developed by using the capacitive [20] or optical methods [21], these sensors are not sensitive enough for ppm level moisture detection. The piezoelectric microcantilever operating in dynamic mode was developed in our lab and was capable of detecting the moisture concentration as low as ppm level.

1.5 Research Objective and Dissertation Outline

Based on the overview of moisture sensors and the advantages of the microcantilever, it is of great interest to develop a new microcantilever sensor to exploit its potential for moisture sensing. The objective of our research is to build up and commercialize the microcantilever based moisture sensor system and, in order to realize this, there are several issues, including fabrication of the microcantilever, readout method selection for the microcantilever, sensing material and process method for the microcantilever surface modification, etc, that need to be considered carefully. Taking these issues into consideration, our research plan was divided into three steps:

1. Based on our existing optical measurement system, SiO_2 microcantilevers were developed as a sensor platform and utilized to confirm that microcantilevers are able to detect moisture concentration as low as ppm level.
2. Comparing different readout methods, through simulation and experimental results, and then selecting the one method, which should be sufficiently sensitive as well as easily integrated with IC technologies, for the microcantilever based moisture sensor.

3. Designing, fabricating, measuring and optimizing the overall sensor system.

In this dissertation, microfabrication technologies, in particular ICP dry etching technology, were developed to fabricate microcantilevers, including SiO₂ microcantilever, metal microcantilever and piezoelectric microcantilever, for the purpose of meeting the requirements of moisture detection based on our design. Simulation and experiments have also been done to find out the most effective way for moisture sensing.

The outline of this dissertation is as follows. A brief overview covering application, classification, history and comparison of moisture sensors is introduced in Chapter one, which also suggests that microcantilevers could be a potential platform for moisture detection. Chapter two describes the concept and operational mechanism of the microcantilever sensor. Simulation and experiments to discover a viable way to commercialize the microcantilever based moisture sensor are presented in Chapter three. Fabrication technologies and processes are presented in Chapters four and five. In Chapter six, detailed experimental procedure based on our optical system used to measure moisture and the corresponding analysis of results are described. The dynamic mode was chosen for commercial application, design, fabrication and test of the piezoelectric microcantilevers, which will operate in frequency mode, are presented in detail in Chapter seven. Conclusions and future work are given in Chapter eight.

CHAPTER TWO

MICROCANTILEVER AS A SENSOR PLATFORM

2.1 Microcantilever

A microcantilever is a long and ultra-thin flexible beam that can act as a physical, chemical or biological sensor by detecting changes in cantilever bending or vibrational frequency. It is the miniaturized counterpart of a diving board that moves up and down at a regular interval. This movement changes when a specific mass of analyte is specifically adsorbed on its surface similar to the change when a person steps onto the diving board. But microcantilevers are a million times smaller than the diving board having dimensions in microns and with different shapes, as shown in figure 2.1, which are rectangular-shaped, double-legged-shaped, and triangular-shaped. The typical dimensions of the cantilever are $0.2\mu\text{m}$ to $1\mu\text{m}$ thick, $20\mu\text{m}$ to $100\mu\text{m}$ wide and $100\mu\text{m}$ to $500\mu\text{m}$ long. Silicon, silicon nitride and silicon dioxide are the typical fabricating materials for cantilevers [6]. Other materials, including plastics, complex metals and piezoelectric materials [1], [23], have also been recently utilized for this purpose.

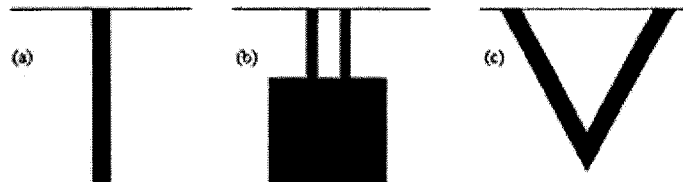


Figure 2.1 Different types of microcantilevers (top view) (a) Rectangular (b)

Double-legged (c) Triangular.

2.2 Operation Mechanism of Microcantilever

Microcantilevers can undergo bending and vibrational frequency changes due to molecular adsorption or absorption, by confining the adsorption and absorption to one side of the cantilever which is coated with a chemically selective layer (figure 2-2). Adsorption or interaction of the target analyte with the chemically selective layer will change the surface characteristics of the microcantilever, or the film volume on the cantilever, and result in bending and resonance frequency changes of the microcantilever. This concept has already been used to demonstrate the feasibility of chemical detection of a number of vapor phase analytes as well as highly sensitive detection of the chemical and biological species in solutions. The changes in humidity, viscosity, pressure, density, temperature, flow rate, pH and the presence of radiation can be measured by detecting changes in the vibrational frequency.

Another way of detecting molecular adsorption is by measuring deflection of the cantilever due to adsorption stress on just one side of the cantilever. Depending on the nature of chemical bonding of the molecule, the deflection can be up or down. Biochips with mechanical detection systems commonly use microcantilever bi-material (e.g. Au-Si) beams as sensing elements. The Au side is usually coated with a certain receptor. Upon the binding of the target analyte (e.g. biological molecules, such as proteins or biological agents) with the receptor, the receptor surface is either tensioned or relieved. This causes the microcantilever to deflect, usually in nanometers, which can be measured using optical techniques. The deflection is proportional to the target analyte concentration.

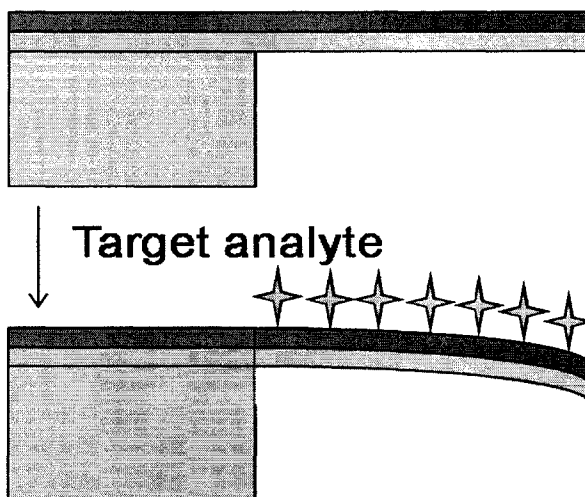


Figure 2.2 Schematic representation of a chemical or biological sensor based on the microcantilever, whose mechanical characteristic can be changed in response to the presence of a target analyte.

2.2.1 Dynamic Mode

Microcantilever sensors, operating in the dynamic mode, are essentially mechanical oscillators, the resonance characteristics of which depend upon the attached mass as well as the viscoelastic properties of the medium. From the simple classical models such as simple harmonic motion, the frequency of an oscillating cantilever, f , can be given in equation (2.1).

$$f = \frac{1}{2\pi} \times \sqrt{\frac{k}{m^*}} \quad (2.1)$$

where k is the spring constant and m^* is the effective mass of the cantilever.

The three main factors that may change the resonating frequency of the cantilever are adsorbate-induced mass loading, viscosity of the media-induced damping, and environmentally induced elasticity changes in microcantilever material. Since the frequency changes due to the viscosity of the medium, and the elasticity changes of the cantilever material are insignificant in many sensor applications, the analyte mass

binding to the cantilever can be related to a shift in the cantilever resonance frequency, f , from f_0 to f_1 as expressed in equation (2.2) [23].

$$\Delta m = \frac{k}{4\pi^2} \left[\frac{1}{f_1^2} - \frac{1}{f_0^2} \right] \quad (2.2)$$

where Δm is the additional suspended mass; k is the cantilever spring constant.

The resonant operation has the advantage that it can potentially provide mass detection at the single molecule level, although adsorption-induced stresses were extensively explored as a transduction principle in many microcantilever sensors. In order to achieve high operational frequencies, the cantilevers used in this mode should be short and stiff. The dynamic mode is preferable as a measurement technique in most of the experiments because of simplicity in set-up and possibility of integration with electronics. The excitation of the cantilever in the frequency mode can be applied by piezoelectric materials or by biomorph effect.

In gas sensors, change in resonance frequency will occur because of the change in density of the sensitive substance on the cantilever surface which further results because of change in mass of the surface of the cantilever when the detectable substance comes in contact with the surface of the cantilever. Higher sensitivity is achieved from the low mass resonators [23].

The absolute minimum detectable mechanical shift in resonant frequency is given by equation (2.3) as shown below

$$\Delta f_{\min} = \frac{2}{X_0} \sqrt{\frac{f_0 k_B T f_{BW}}{kQ}} \quad (2.3)$$

where X_0 is the oscillation amplitude, k is the spring constant, Q is the mechanical quality factor, k_B is Boltzmann constant and f_{BW} the measurement bandwidth.

And minimum detectable mass can be given as

$$\Delta m_{\min} = \frac{4m}{X_0} \sqrt{\frac{k_B T f_{BW}}{f_0 k Q}} \quad (2.4)$$

The above equation (2.4) helps to calculate the sensitivity and detection limit of the gaseous sensors.

When an axial load is applied uniformly on the entire beam of the cantilever, the resulting surface stresses will either compress or stretch the cantilever beam, which further results in an increase or decrease in the resonant frequency of the cantilever at any bending mode.

Chen et al. [6] have developed a relation which predicts i th-mode resonant frequency, which results with the addition of surface stress, as given in equation (2.5)

$$f_i^{+\sigma} = \frac{1}{2\pi\sqrt{3}} \left[1 + \frac{2\sigma L^3}{EI\pi^2} \right]^{\frac{1}{2}} \left(\frac{\alpha_i}{L} \right)^2 \sqrt{\frac{EI}{\rho_b w t}} \quad (2.5)$$

where E is beam elastic modulus, w is width, I is the second moment of cross-sectional area, α_i is determined from the frequency relation for a freely vibrating cantilever beam. The bracketed term in the above equation shows that the influence of the surface stress either compressive or tensile, will tend to increase or decrease microcantilever resonant frequencies.

The change in surface stress of the microcantilever before and after adsorption can be determined from in equation (2.6)

$$\sigma = \left[\left(\frac{f_i^{+\sigma}}{f_i} \right)^2 - 1 \right] \frac{EI}{2L^3} \quad (2.6)$$

where σ is the surface stress of the cantilever and I is the moment of cross sectional area [6].

2.2.2 Static Bending Mode

If external gravitational, magnetic and electro-static forces are absent, the deflection of a cantilever is unambiguously related to a gradient of mechanical stress generated on the cantilever. When the molecular adsorption is confined to one side of the cantilever surface, there is an adsorption-induced differential stress on the cantilever, which can be observed as the cantilever deflection.

Several surface modification coatings can provide chemical responses for cantilevers working in the static bending model. Three distinctive models are usually considered. The first model is most adequate when interactions between the cantilever and its environment are purely surface confined. The second model is applicable when a micro-cantilever is modified with an analytic permeable coating that is much thicker than a monolayer. The third model is relevant to structure interfaces and coatings. In fact, much detailed research has been applied to the first model.

Adsorption-induced surface stress on the microcantilever can be predicted using Stoney's Formula, as given in equation (2.7)

$$\frac{1}{R} = 6 \left(1 - \frac{\nu}{Et^2} \right) \delta s \quad (2.7)$$

where R is the cantilever's radius of curvature, E is Young's modulus for the substrate, ν is Poisson's ratio, t is the thickness of the cantilever, L is the length of the cantilever, and δs is the differential stress on the cantilever [24].

The observed deflection (ΔZ) at the end of a rectangular cantilever can be related to the change in surface stress, as shown in equation (2.8)

$$\Delta Z = \left[3(1 - \nu) \frac{L^2}{Et^2} \right] \delta s \quad (2.8)$$

where ν is Poisson's ratio of the substrate, L is length of the cantilever, E is Young's modulus for the substrate, t is thickness of the cantilever and δs is the film stress change.

The deflection mode or static bending mode was used extensively in the majority of the recent studies on micro-cantilever sensors. However, resonating microcantilever can offer uniquely high mass sensitivity that can not be achieved by using the static bending mode. Therefore, resonating microcantilevers may be indispensable in applications where species to be detected and analyzed are available in very minute quantities.

2.3 Common Readout Schemes of Microcantilever

Operation of any microcantilever sensors relies on real-time measurements of microcantilever deflections with at least nanometer accuracy. Thus, a readout system capable of monitoring changes directly related to microcantilever deflection is very important for any microcantilever sensor. Optical, piezoresistive, piezoelectric, capacitance, or MOSFET-embedded methods could serve to measure the deformations and resonance frequency shifts of microcantilever sensors with sufficient precision. All these methods are compatible with array formats.

2.3.1 Optical method

Optical methods are most extensively used for measurements of cantilever deflections in applications. The optical method [25], as shown in figure 2.3, employs a laser beam of very low power of the order that does not affect the molecules coated on the surface of the microcantilever or the position sensitive photodetector (PSD). A laser beam is focused on the free end of the cantilever and gets reflected because the gold layer coated on the surface of the cantilever gives an almost mirror like finish. The

reflected beam falls on the PSD. When the cantilever is undeflected i.e. it is not coated with any molecule, the laser beam would fall on a particular spot on the PSD. As the cantilever deflects, the position of the beam changes, which, in turn, is calculated using appropriate electronics. A most common type of PSD is based on a quadrant photodiode that consists of four cells: A, B, C, and D. Each of the cells is coupled to the input of a separate transimpedance amplifier the output voltages of which, V_A , V_B , V_C , and V_D , are proportional to the illumination of the respective quadrants. The normalized differential output, $V_{out} = [(V_A + V_C) - (V_B + V_D)] / (V_A + V_B + V_C + V_D)$, depends linearly on the vertical displacement of the weighted center of the light spot projected by the cantilever. This particular optical detection scheme can discern extremely small changes in the cantilever bending. Measurements of 10^{-14} m displacements have been reported [26]. But, this method also has its own disadvantages. The presence of a focused laser beam in a liquid cell environment can result in additional thermal management issues giving rise to extraneous readings. Secondly, the alignment system is expensive and involves great precision, which can ultimately raise the cost of the whole diagnostic kit. In addition, it also reduces the kit's portability.

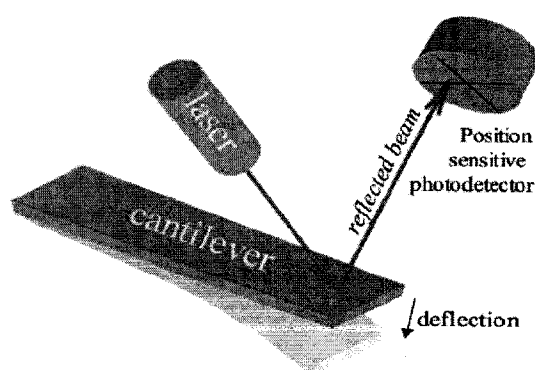


Figure 2.3 Schematic of an optical detection system for detecting microcantilever deflection.

2.3.2 Piezoresistive method

The piezoresistive method [27], [28], [29] involves the embedding of a piezoresistive material near the top surface of the cantilever to record the stress change occurring at the surface of the cantilever. When the microcantilever is deformed, it undergoes a stress change that will apply strain to the piezoresistor, thereby causing a change in resistance that can be measured by electronic means.

The piezoresistor material in the beam, which commonly is doped single crystal silicon or doped polysilicon, must be localized as close to one surface of the cantilever as possible for maximum sensitivity. The type of doping being used for fabrication of the piezoresistive material is an important factor. The piezoresistive coefficient of N-type silicon is greater than that for P-type. The resistance of a piezoresistive material changes when strain is applied to it. The relative change in resistance as function of applied strain can be written as:

$$\frac{\Delta R}{R} = K_l \delta_l K_t \delta_t \quad (2.9)$$

where K denotes the Gage Factor, which is a material parameter. The subscripts l and t refer to the longitudinal and the transversal part of the Gage Factor [30].

The sensitivity of a piezoresistor varies proportionally to the thickness t and the radius of curvature. The Gage Factor is proportional to Young's Modulus, E , which is the intrinsic characteristic of the material. The gage factor can also be calculated directly from equation (2.10) by straining the cantilevers and measuring the resistance change.

$$GF\delta = \frac{\Delta R}{R} \quad (2.10)$$

where δ is the strain in the material and R is the resistance. For a sensitive device, the gage factor should be of the order of 100 [30].

The piezoresistive cantilever beam can be used as an arm of the Wheatstone Bridge circuit, as shown in figure 2.4. The resistance of the variable resistance arm ($R_0 + \Delta R$) in figure 2.4 can be determined by using the common voltage divider formula which as is shown below:

$$\Delta V = V_0 \left\{ \frac{R_2}{R_1 + R_2} - \frac{R_3}{R_0 + \Delta R + R_3} \right\} \Rightarrow R_0 + \Delta R = R_3 \left\{ \frac{V_0(R_1 + R_2)}{R_2 V_0 - \Delta V(R_1 + R_2)} - 1 \right\} \quad (2.11)$$

There would be a resistance change whenever the cantilever is subjected to a deflection.

The advantage of the piezoresistive method is that the readout system can be integrated on the chip. The disadvantage is that the deflection resolution for the piezoresistive readout system is only one nanometer compared with one Angstrom for the optical detection method. Another disadvantage with the method is that a piezoresistor has to be embedded in the cantilever. The fabrication of such a cantilever with a composite structure is more complicated [30].

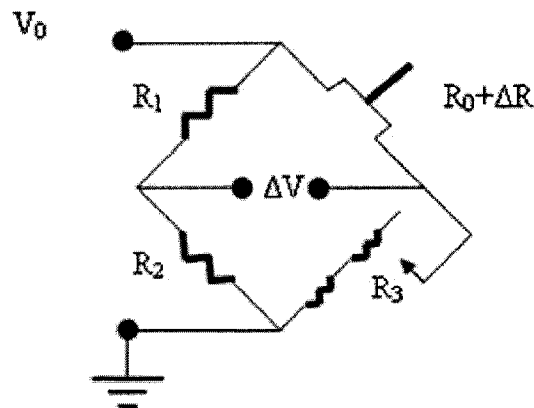


Figure 2.4 The Wheatstone Bridge Circuit used for the piezoresistive microcantilever.

2.3.3 Piezoelectric method

The piezoelectric readout technique requires the deposition of piezoelectric

material, such as ZnO, on the cantilever. Due to a piezoelectric effect, transient charges are induced in the piezoelectric layer when the cantilever is deformed [26].

The main disadvantage of the piezoelectric as well as piezoresistance readout is that they require electrical connections to the cantilever. An additional disadvantage of the piezoelectric technique is, that in order to obtain large output signals, the thickness of the piezoelectric film needs to be well above the values that correspond to optimal mechanical characteristics. Furthermore, the piezoelectric readout is inefficient when slowly changing cantilever deflections need to be measured. Because of the aforementioned disadvantages, the application of the piezoelectric readout to MEMS sensors is somewhat limited. However, a piezoelectric microcantilever employing a piezoelectric component, can vibrate at its resonant frequency upon the application of an appropriate AC voltage and provide an electrical signal at the output via piezoelectric coupling [31]. This electrical transduction leads to a simplified miniaturization of an integrated device, as compared with conventional complex transducers.

2.3.4 Capacitive method

Capacitance readout is based on measuring the capacitance between a conductor on the cantilever and another fixed conductor on the substrate that is separated from the cantilever by a small gap [26]. Changes in the gap due to cantilever deformation result in changes in the capacitance between the two conductor plates. The relationship is shown in the following equation:

$$C = \epsilon \frac{A}{d} \quad (2.10)$$

According to equation (2.12), the capacitance of a flat capacitor is inversely proportional to the separation distance, thus, sensitivity of this method relies on a

very small gap between the cantilever and the substrate. Capacitance readout suffers from interference from variations in the dielectric constant of the medium. While differential schemes may eliminate this interference, electrically conductive media, such as electrolytes, make capacitance readout more challenging [26]. One of the main advantages of capacitance readout is that it can be used in integrated MEMS devices that are fully compliant with standard CMOS technology. But this technique is limited in its application to sensing because it is very difficult to manipulate a very small gap between cantilever beam and the adjacent conductor to achieve high sensitivity.

2.3.5 MOSFET-Embedded method

Recently, G. Shekhawat, et al. [32] provided a promising readout approach, a MOSFET-Embedded method for microcantilever sensors. The MOSFET-Embedded readout is used to measure the deflection of the microcantilever by embedding a metal-oxide semiconductor field-effect transistor (MOSFET) into the base of the cantilever and recording changes in the drain current. The MOSFET-embedded microcantilever detection approach is illustrated in figure 2.5. When a microcantilever bends as a result of adsorption-induced surface stress, modulation of the channel current underneath the gate region results from alteration in the channel mobility of the transistor, due to increased channel resistance. As fixed biased voltages are applied to the gate and source-drain region of the transistor, any change in channel mobility will result in a change in the drain current of the transistor. Therefore, a bending of the microcantilever by as little as 5 nanometers could be detected by measuring changes in the drain current of the MOSFET.

The MOSFET detection method offers a number of advantages over traditional piezoresistive or capacitive sensor elements because of its small size, high sensitivity,

and uncomplicated current measurement as well as its full and seamless compatibility with direct monolithic integration for application-specific integrated circuits. But the fabrication process of this method is more complicated compared to other methods.

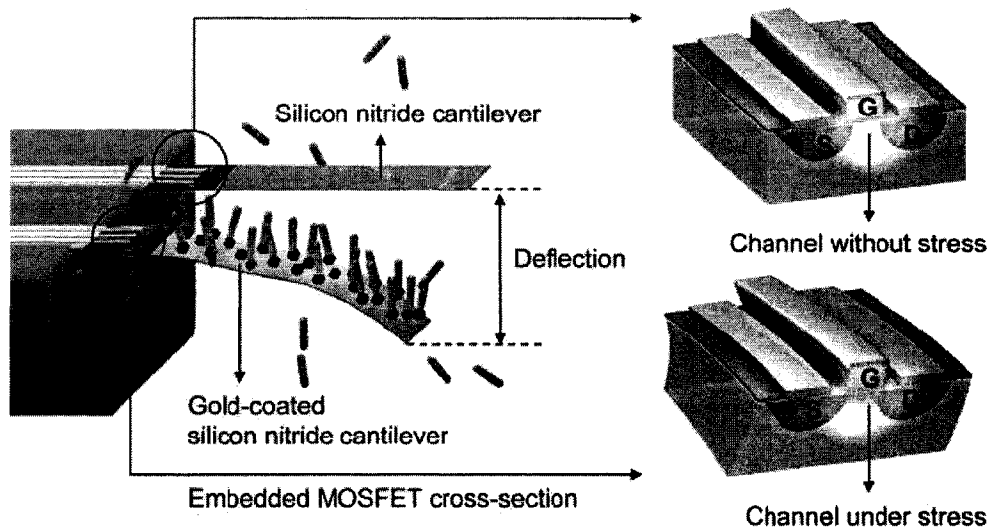


Figure 2.5 Schematic of the interaction between probe and target molecules on an embedded-MOSFET cantilever system. The silicon nitride cantilever is a reference, and the gold-coated one is used as a sensing cantilever. Specific biomolecular interactions between receptor and target bend the cantilever. A magnified view of the embedded MOSFET in cross section shows the stressed gate region when the cantilever bends, resulting in a change in drain current due to conductivity modulation of the channel underneath the gate.

2.4 Summary

Microcantilevers are recognized as a promising platform for the next generation of physical, chemical and biological sensors. The major advantages of employing microcantilevers as sensing mechanisms over conventional sensors include their high sensitivity, low cost, low analyte requirement (in μl), non-hazardous procedure with fewer steps (obviating the need for labels), quick response and low power requirement. Another unique advantage of microcantilever sensors is that deformation and resonance frequency shifts are measured simultaneously, providing complementary information about the interactions between the transducers and the environment. Both

static and dynamic responses of cantilever sensors can be measured with very high precision using several readout techniques based on optical beam deflection, interferometry, electron transfer, piezoresistance, capacitance, and piezoelectric properties. It is anticipated that microfabricated cantilevers can provide an outstanding platform for real-time, *in situ* measurements of moisture in industrial or household environment.

CHAPTER THREE

SIMULATION AND INVESTIGATION OF READOUT METHOD

FOR MICROCANTILEVER AS A MOISTURE SENSOR

3.1 Simulation of SiO₂ Microcantilever for Optical Method

In order to develop the microcantilever as a sensor platform using the optical method, its sensitivity is mainly dependent on the deflection of the cantilever beam caused by surface stress. Due to the relatively large Young's modulus of silicon material, the bending response of the silicon microcantilever is too weak to be measured when the surface stress change is rather small. The silicon dioxide (SiO₂) microcantilever can provide a much higher mechanical sensitivity compared to its silicon or silicon-nitride counterparts, as a thermally grown SiO₂ film features a much lower Young's modulus than single-crystalline silicon or silicon nitride [1], [34]. It can be clearly seen that [35] lists Young's modulus values of thermal SiO₂, single crystalline Si and LPCVD (low pressure chemical vapor deposition) Si₃N₄ as 57–79 GPa, 170 GPa and 290–380 GPa, respectively. The high mechanical sensitivity leads to a large surface-stress-induced bending of the cantilever. To compare the Si and SiO₂ cantilevers, the deflections of both microcantilever beams induced from uniformly applied surface stress are analyzed. The simulation results proved that the SiO₂ cantilever beam has a higher sensitivity compared to the Si beam.

3.1.1 Theoretical Analysis

To prove that a microcantilever made of silicon dioxide could give the larger bending amplitude under the same surface stress as a silicon cantilever, simulation and theoretical analysis have been conducted.

Cantilevers intended for use as chemical sensors are typically modified such that one of the sides is relatively passive while the other side exhibits high affinity to the targeted analyte. In fact, the sources of surface stress can be the surface reconstruction, or the interactions between a surface and its ambient environment etc. In many cases, adsorbate-induced deformations of cantilever beams can be predicted by the model shown in figure 3.1(a), in which the beam tip is under a uniformly distributed loading, σ . The unit of σ is Newton/meter, not Pascal and $\sigma > 0$ is tensile. A concentrated moment M applied at the cantilever beam's free end can be on behalf of this surface stress effect. Therefore, the relationship between the moment and deflection function of the cantilever beam is expressed as [36]

$$E^* I \frac{d^2 y(x)}{dx^2} = M \quad (3.1)$$

The boundary conditions are given as

$$\begin{cases} y(x) \Big|_{x=0} = 0 \\ \frac{dy(x)}{dx} \Big|_{x=0} = 0 \end{cases} \quad (3.2)$$

Here, E^* is the biaxial modulus. E^* is defined as $E^* = E/(1-\nu)$. E and ν represent the cantilever beam Young's modulus and the Poisson's ratio, respectively. The area moment of inertia I is expressed as [36]

$$I = \frac{1}{12} wt^3 \quad (3.3)$$

where t is the thickness of the cantilever beam, and $y(x)$ represents the deflection

function of the cantilever beam. According to figure 3.1(b), the concentrated moment M is derived as

$$M = \Delta\sigma wt / 2 \quad (3.4)$$

$\Delta\sigma$ represents differential surface stress, and $\Delta\sigma = \sigma^+ - \sigma^-$, σ^+ and σ^- are surface stresses on the top and bottom surfaces of the cantilever beam, respectively.

Combining equation (3.1) and boundary condition (3.2), the deflection is derived as

$$y = \frac{Mx^2}{2E^*I} \quad (3.5)$$

Generally, the curvature κ of the deflected beam is approximately assumed as $\kappa = d^2y/dx^2$ because of the linear analysis of a small deflection. Then, the curvature κ and the radius of microcantilever curvature are given as

$$\kappa = \frac{1}{R} = \frac{M}{E^*I} = \frac{6\Delta\sigma(1-\nu)}{Et^2} \quad (3.6)$$

In fact, the equation above is the famous Stoney's formula. Knowing the radius of curvature R , the deflection at the end of the cantilever beam can be expressed as

$$y_{\max} = \frac{L^2}{2R} = \frac{3L^2(1-\nu)}{Et^2} \Delta\sigma \quad (3.7)$$

Even though Stoney's formula serves as a cornerstone for curvature based analysis and a technique for the measurement of surface stress, it does not agree well with the experimental data for structures under larger deflection or a 'thick' film coating on the substrate [37], [38]. In addition, the above model that regards the surface stress as a moment applied at the beam's free edges and does not take into account the influence of the surface stress on structure stiffness. Thus, Y. Zhang et al. [39] provided a new model which is demonstrated in figure 3.1(b). This model assume an area stress s uniformly distributed on the top surface of the beam. They modeled this as a uniformly distributed axial stress s_w along the beam's neutral axis and a uniformly distributed bending

moment m along the beam. In terms of this, they derived the governing equation as

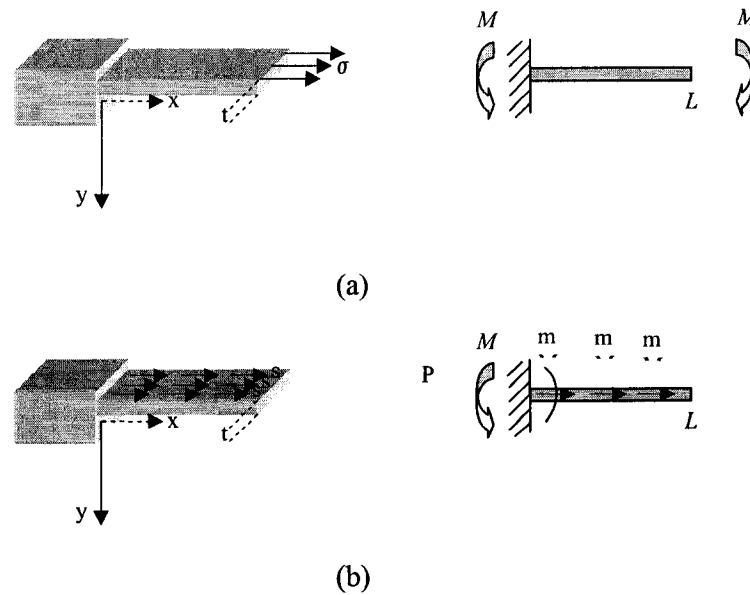


Figure 3.1 Scheme diagram for theoretical analysis

$$E^* I \frac{d^4 y}{dx^4} - sw(L-x) \frac{d^2 y}{dx^2} + sw \frac{dy}{dx} = 0 \quad (3.8)$$

and boundary conditions as

$$\left\{ \begin{array}{l} y(x) \Big|_{x=0} = 0 \\ \frac{dy}{dx} \Big|_{x=0} = 0 \\ \frac{d^2 y}{dx^2} \Big|_{x=L} = 0 \\ E^* I \frac{d^3 y}{dx^3} \Big|_{x=L} + m = 0 \end{array} \right. \quad (3.9)$$

In most cases, equation (3.8) is solved by the numerical method since its analytical solution is very difficult to obtain.

3.1.2 Simulation Results

This second model based on equation (3.8) models the surface stress effect better. A beam module ($L=250 \mu\text{m}$, $w=100 \mu\text{m}$, $t=1 \mu\text{m}$) was simulated in CoventorWare (Coventor Inc., Cary, NC) to compute the mechanical deformation induced by uniform

surface stress through the finite element method (FEM). Actually, to calculate the amount of deflection at the tip of a microcantilever beam, the differential equation (3.1) is employed in most finite element analysis. When applying boundary conditions to the meshed model, we divided the load force applied on the beam surface into a uniform concentrated force in each element, which is equivalent to the conditions described in the aforementioned second model. If the cantilever is made of silicon dioxide, Young's modulus $E=73.0$ GPa, Poisson's ratio $\nu=0.17$, and the maximum deflection at the end of the silicon dioxide beam is 16.49 nm. On the other hand, if the cantilever beam is made of silicon, Young's modulus $E=169.0$ GPa, Poisson's ratio $\nu=0.3$, and the maximum deflection of the cantilever beam is 6.96 nm. The simulation results of beam deflection are shown in figure 3. The SiO_2 beam can give a 2.37 times larger bending amplitude under the same conditions compared with the silicon beam. A higher sensitivity could be achieved through using the silicon dioxide instead of silicon as the cantilever beam.

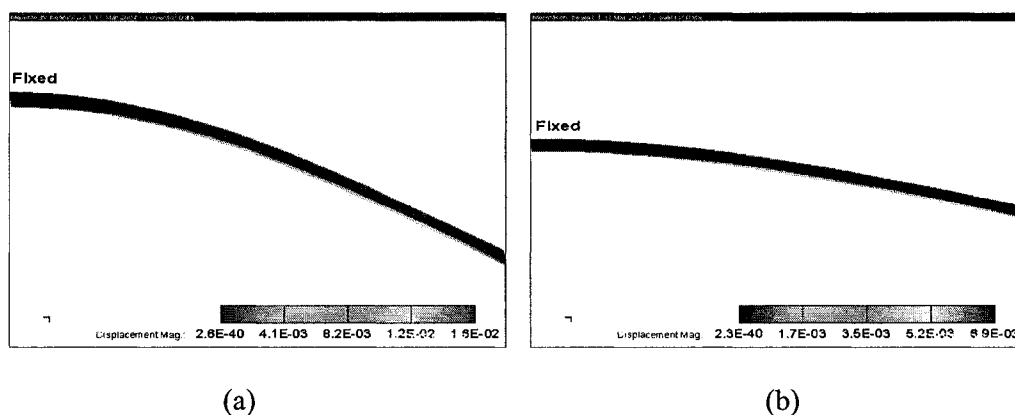


Figure 3.2 The deflection contour of cantilever beam. (a) SiO_2 . (b) Si.

Optical readout systems are most extensively used for measurements of cantilever deflections in labs and can meet the company's requirement for measuring the moisture level ranging from 1ppm to 100ppm. For use in an industrial application, it still has some disadvantages, such as its alignment system is expensive and involves great

precision, and is not compliant with IC technology and, consequently, is not portable. Therefore, it is very important to find one operational mode with an appropriate readout system that is fit for commercial applications and which requires that this microcantilever sensor system not only has the capability of detecting low moisture level but is also portable.

3.2 Investigation of Piezoresistive Readout Method

3.2.1 FEM analysis

The geometry of a silicon piezoresistive microcantilever in our simulation is shown in figure 3.3. The MemPZRmodule in CoventorWare computes the change in resistivity of a piezoresistive material subject to mechanical deformations through the finite element method (FEM). The piezoresistive phenomenon in semiconductors is linked to a change in the resistivity of the silicon materials in response to an applied stress. Ohm's Law, in the stress-free state, represents this effect mathematically [40]

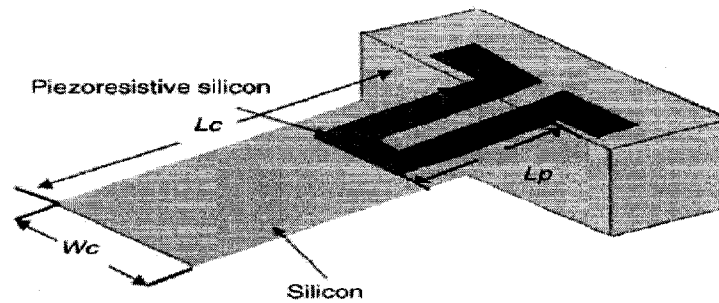


Figure 3.3 Schematic diagram of a Silicon piezoresistive microcantilever.

$$\begin{bmatrix} E_1 \\ E_2 \\ E_2 \end{bmatrix} = \rho_0 \begin{bmatrix} 1 & 0 & 0 \\ 0 & 1 & 0 \\ 0 & 0 & 1 \end{bmatrix} \begin{bmatrix} i_1 \\ i_2 \\ i_3 \end{bmatrix} \quad (3.10)$$

where E_i , i_i are the electric field and current density, respectively, parallel to the x_i crystallographic axis and ρ_0 is the stress-free resistivity, which may be a tensor in

general.

When a stress field is applied, the resistivity is modified and becomes anisotropic. The change in resistivity is related to the stress tensor through the empirically determined piezoresistive coefficient. For the silicon material, there are three independent piezoresistive coefficients π_{11} , π_{12} , and π_{44} , where the subscripts physically represent the electric field, current density, and stress along the three crystallographic directions for cubic crystal silicon. The change in resistivity is related to the surface stress through the empirically determined piezoresistive coefficient. N-type doped silicon was used as the piezoresistor and the default material properties were employed in this work.

3.2.2 Simulation Results and Discussion

The cantilever sensitivity can be expressed as the fractional change of resistance of the cantilever ($\Delta R/R$). The cantilever thickness is a critical parameter that affects sensitivity. Therefore, the sensitivity of four kinds of Si microcantilever, whose beam thickness are $1\mu\text{m}$, $0.75\mu\text{m}$, $0.5\mu\text{m}$ and $0.25\mu\text{m}$ respectively, were investigated as a function of cantilever deflection. The dimensions of the cantilever are $250\mu\text{m}$ in length and $100\mu\text{m}$ in width and the unit of deflection is μm . The solid round line, dash round line, solid triangular line and dash triangular line represent different thickness of piezoresistor respectively, whose value can be seen on the left top corner of each figure in figure 3.4. Finite element analysis (figure 3.4) shows that sensitivity increases almost linearly with increasing deflection of the cantilever. It (figure 3.5) also describes that the sensitivity is enhanced when the thickness of the piezoresistor decreases. This is probably due to (a) larger bending when the piezoresistor is thinner and/or (b) the resistivity change is larger for thin Si materials because of the quantum size aspects of the piezoresistor [41]. Figure 3.6 demonstrates that the sensitivity

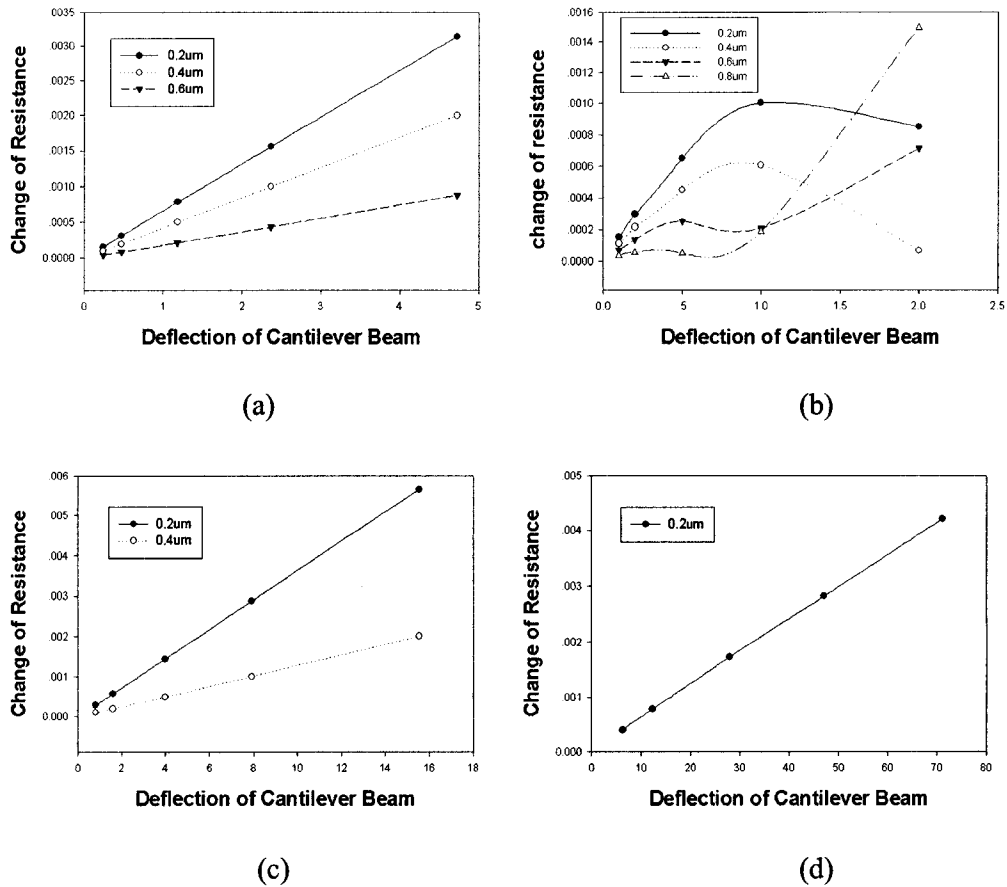


Figure 3.4 The sensitivity as a function of deflection of the cantilever beam with different beam thickness (a) 1µm (b) 0.75µm (c) 0.5µm (d) 0.25µm and different piezoresistor thickness.

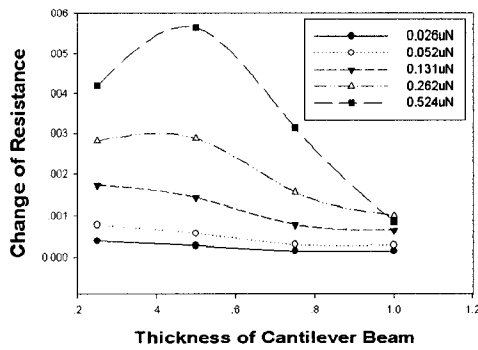


Figure 3.5 Sensitivity as a function of thickness of the cantilever beam corresponding to different force.

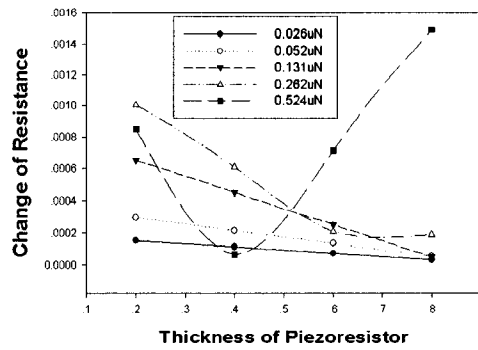


Figure 3.6 Sensitivity as a function of thickness of the piezoresistor corresponding to different force.

decreases with increasing thickness of the cantilever beam. The spring constant of the cantilever beam would be raised with an increase in the thickness of the cantilever beam and, thus, the deformation of that cantilever beam would be decreased, which causes less change of resistance in the piezoresistor. Actually, the deflection of a 1 μm thick cantilever beam is less than 100nm, if the moisture level as low as 1 to 10 ppm. According to the simulation results, even using a 0.25 μm thick beam with a 0.2 μm thick piezoresistor under the same applied force, which causes 0.1 μm bending of a 1 μm thick beam, the sensitivity is just 0.03991%, which is too small to be detected in the experiment. Therefore, the piezoresistive method is not feasible to detect extremely low moisture levels.

3.3 Investigation of MOSFET-Embedded Readout Method

As we mentioned in the previous Section 2.3.5, the MOSFET detection method is a good alternative to piezoresistive or capacitive method in applications for microcantilever sensors. So, the possibility to measure such low moisture levels in our project needs to be analyzed in detail.

3.3.1 Mathematic Model

Stress applied on the MOSFET will induce two types of change in the device, which are bandgap change and mobility change. Models of these two changes are described as follows.

3.3.1.1 Stress-Induced Bandgap Change

Mechanical stress and strain in silicon regions can cause variations in the bandgap in both Taurus Device & Process. Under Boltzmann statistics, the change in the conduction and valence band edges are as follows [42]:

$$\Delta E_c = -kT \ln \left(\sum_{i=1}^3 \frac{\exp\left(\frac{-\Delta E_{ci}}{kT}\right)}{3} \right) \quad (3.11)$$

$$\Delta E_V = kT \ln \left(\frac{x_0}{1+x_0} \exp\left(\frac{\Delta E_{Vl}}{kT}\right) + \frac{1}{1+x_0} \exp\left(\frac{\Delta E_{Vh}}{kT}\right) \right) \quad (3.12)$$

where:

- ΔE_{Ci} is the shift in the band edge of the i^{th} ellipsoidal conduction minima
- ΔE_{Vl} and ΔE_{Vh} are the shifts in the band edges for the light and heavy hole maxima, respectively, that make up the valence band.
- x is given by $(MLO/MHO)^{3/2}$
- The band edge shifts are computed using the deformation potential theory from Bir and Pikus [43]:

$$\Delta E_{Ci} = D(\varepsilon_{11} + \varepsilon_{22} + \varepsilon_{33}) + U\varepsilon_{ii} \quad (3.13)$$

$$\Delta E_{V(h,l)} = A(\varepsilon_{11} + \varepsilon_{22} + \varepsilon_{33}) \mp \sqrt{\varphi} \quad (3.14)$$

where

$$\varphi = B^2/2 \{(\varepsilon_{11} - \varepsilon_{22})^2 + (\varepsilon_{22} - \varepsilon_{33})^2 + (\varepsilon_{33} - \varepsilon_{11})^2\} + C^2(\varepsilon_{12}^2 + \varepsilon_{13}^2 + \varepsilon_{23}^2) \quad (3.15)$$

and ε is the strain tensor in the crystallographic coordinate system. The deformation potential constants, **D**, **U**, **A**, **B**, and **C** can be adjusted from their default values on the **Physics** command.

The spatial variations of E_C and E_V result in an adjustment to the electric field terms that are used in the transport equations. Therefore, the current density will be changed due to this adjustment.

3.3.1.2 Stress-Induced Mobilities Change

Mechanical stress and strain in silicon regions can also cause variations in electron and hole mobilities in both Taurus Device & Process. This model must be used in conjunction with the stress-induced bandgap model described above. Although both

models influence the electrical characteristics of MOSFET, the mechanical stress induced change in the mobility will affect the drain current much more than stress induced change in bandgap [44]. Due to the very different band structure of the conduction and valence bands, the effect of stress of the electron and hole mobilities is very different. Using the model from Egley [42], the electron mobility becomes anisotropic under stress and can be written as a diagonal tensor in the crystallographic coordinate system as:

$$\mu'_n = \mu_{n0} \begin{pmatrix} 1 + \beta_1 & 0 & 0 \\ 0 & 1 + \beta_2 & 0 \\ 0 & 0 & 1 + \beta_3 \end{pmatrix} \quad (3.16)$$

where μ_{n0} is the nominal, isotropic mobility without stress and

$$\beta_i = \left(\frac{1 - MLMT}{1 + 2MLMT} \right) \left(\frac{\exp\left(-\frac{\Delta E_{Ci}}{kT}\right)}{\exp\left(-\frac{\Delta E_C}{kT}\right)} - 1 \right) \quad (3.17)$$

where:

- ΔE_{Ci} is the net effective shift in the conduction band
- $MLT.STR = m_L/m_T$ is the ratio of the longitudinal and transverse effective masses.

During device simulation, the mobility tensor must be transformed to the device coordinate system using a similarity transformation:

$$\mu'_n = \mu_{n0} \begin{pmatrix} \mu_{xx} & \mu_{xy} & \mu_{xz} \\ \mu_{xy} & \mu_{yy} & \mu_{yz} \\ \mu_{xz} & \mu_{yz} & \mu_{zz} \end{pmatrix} = A \mu'_n A^{-1} \quad (3.18)$$

where A is the transformation from the crystallographic coordinate system to device coordinate system as determined by the substrate orientation. For an arbitrary substrate orientation, the mobility tensor in the device coordinate system contains, in general, off-diagonal components. Similar to the inclusion of anisotropic transport in the Anisotropic Material Advance Application Module, however, these off-diagonal components are neglected in the discretization of the continuity equations.

Under certain circumstances, however, the transformed mobility tensor in (3.18) remains diagonal and is thus treated exactly. This occurs, for example, for a device under planar strain with a substrate orientation of $\langle 100 \rangle$ and an x-axis orientation of $\langle 110 \rangle$.

In the model from Egley, the hole mobility remains isotropic and is given by:

$$\mu = \mu_{p0} \left\{ 1 + (MUL0) \frac{x_0}{1+x_0} \left[\exp\left(\frac{\Delta E_{vl} - \Delta E_{vh}}{kT}\right) \right] - 1 \right\} \quad (3.19)$$

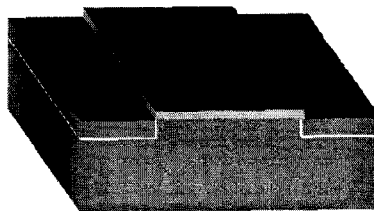
where:

- μ_{p0} is the nominal hole mobility without stress
- $MUL0 = \mu_{pl} / \mu_{p0}$ is the ratio of the unstressed light hole mobility to the total hole mobility

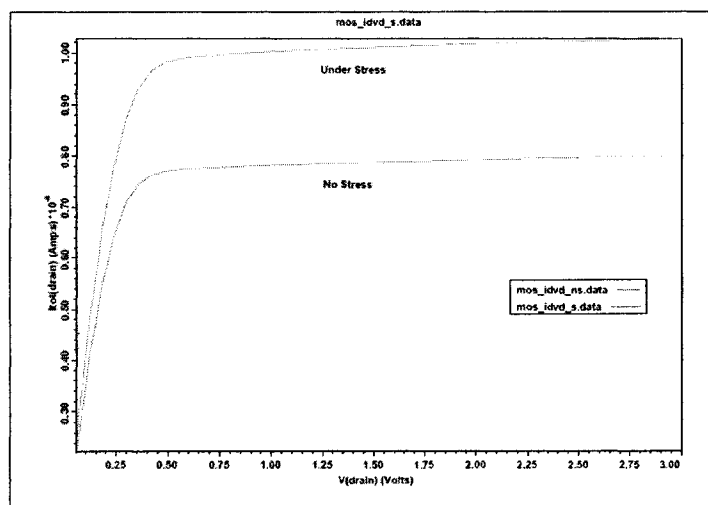
3.3.2 Results and Discussion

We investigate the influence of different parameters in the MOSFET (including channel length, source-drain doping concentration, substrate doping concentration, junction depth, applied stress and MOSFET width in 3-D) on drain current and its' percentage of changes caused by mechanic stress.

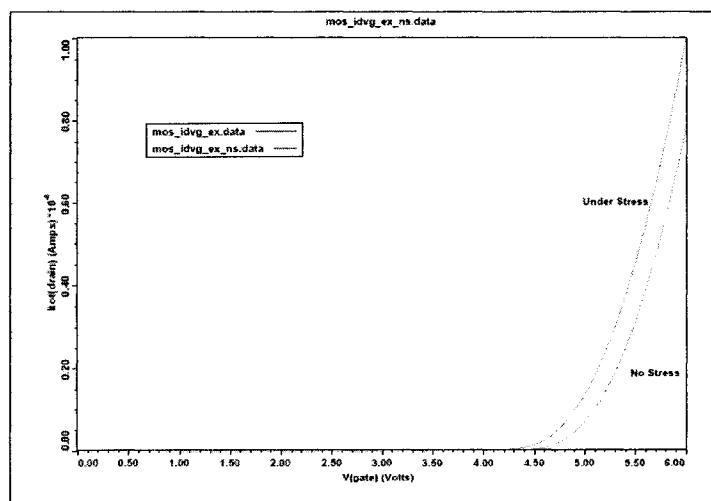
Figure 3.7 shows (a) MOSFET structure, (b) I_d - V_d curve, (c) I_d - V_g curve for the whole MOSFET with length =10 μ m, channel length =5 μ m, substrate doping concentration =1e17, source-drain doping concentration =3e20, junction depth =0.2 μ m, and drain voltage =3.0V.



(a)



(b)



(c)

Figure 3.7 (a) MOSFET structure, (b) I_d - V_d curve, (c) I_d - V_g curve.

Figure 3.8 (a) shows that the drain current both under stress and under no stress, decreased as the channel length increased. In Figure 3.8 (b), the changes in drain

current due to stress were almost stable at 28%, except one point at $10\mu\text{m}$, with increasing channel length.

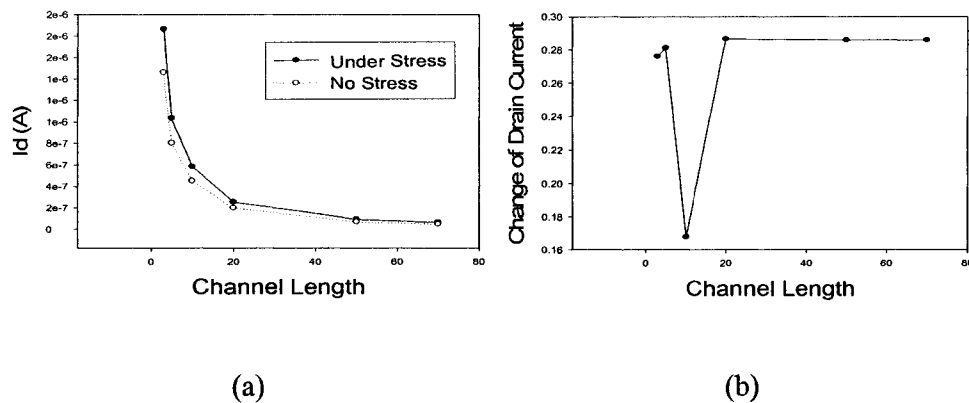


Figure 3.8 The whole MOSFET with length $=100\mu\text{m}$, substrate doping concentration $=1e17$, source-drain doping concentration $=1e20$, junction depth $=0.2\mu\text{m}$, and drain voltage $=3.0\text{V}$. (a) Drain current as a function of channel length, (b) Change of Drain current as a function of channel length

Figure 3.9 (a) shows that the drain current, both under stress and under no stress, did not change much as the Source-Drain doping concentration increased. In Figure 3.9 (b), the changes in drain current due to stress were also stable at 28% with increasing Source-Drain doping concentration.

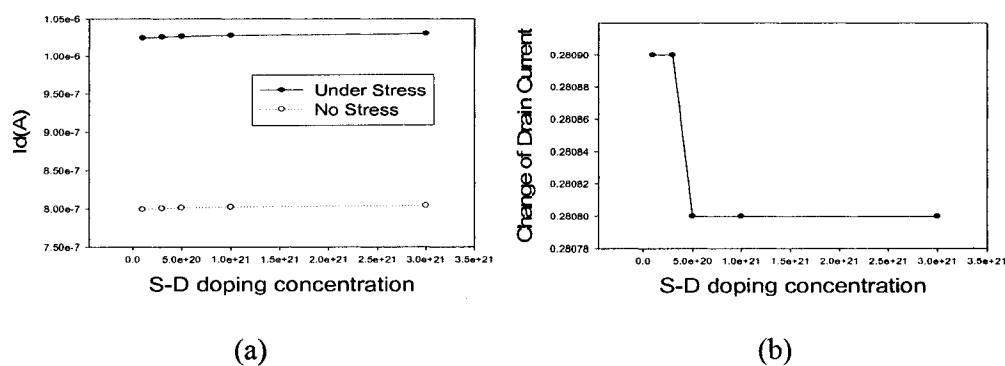


Figure 3.9 The whole MOSFET with length $=10\mu\text{m}$, channel length $=5\mu\text{m}$, substrate doping concentration $=1e17$, junction depth $=0.2\mu\text{m}$, and the drain voltage $=3.0\text{V}$. (a) Drain current as a function of Source-Drain doping concentration, (b) Change of Drain current as a function of Source-Drain doping concentration.

Figure 3.10(a) shows that the drain current both, under stress and under no stress, varied as substrate doping concentration increased. In Figure 3.10 (b), the changes in drain current due to stress has a highest point = 38% at 3.0×10^{17} doping concentration with increasing substrate doping concentration.

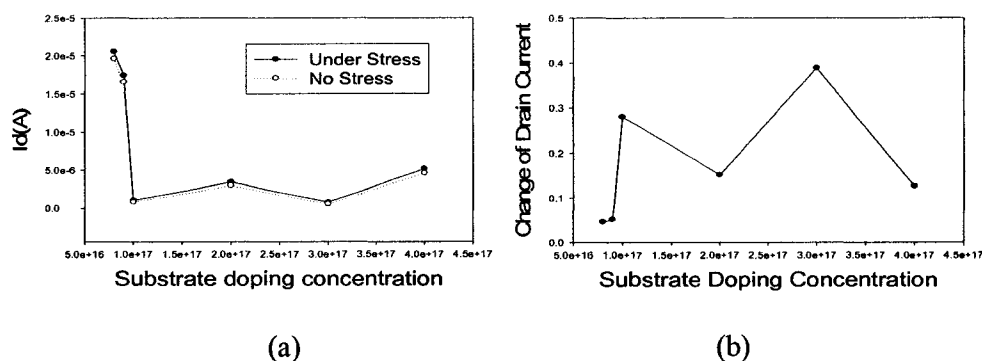


Figure 3.10 The whole MOSFET with length = $10 \mu\text{m}$, channel length = $5 \mu\text{m}$, source-drain doping concentration = 1×10^{20} , junction depth = $0.2 \mu\text{m}$, and the drain voltage = 3.0V . (a) Drain current as a function of substrate doping concentration. (b) Change of Drain current as a function of substrate doping concentration

Figure 3.11 (a) shows that the drain current, both under stress and under no stress, increased a little as junction depth increased. In Figure 3.11 (b), the changes of drain current due to stress were also stable at 28% with increasing junction depth.

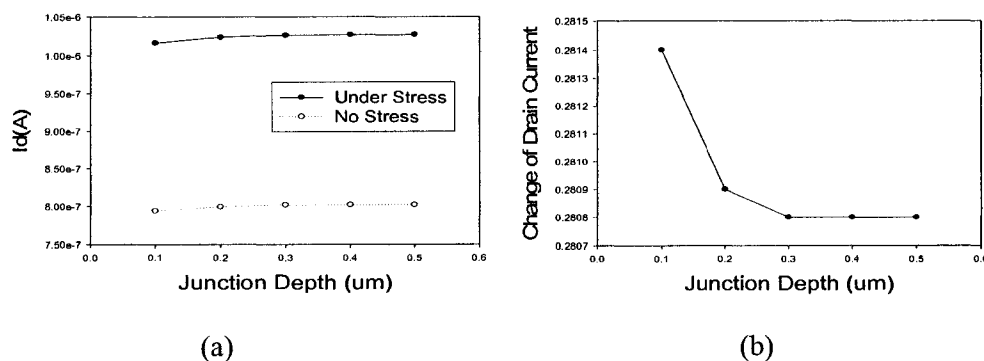


Figure 3.11 The whole MOSFET with length = $10 \mu\text{m}$, channel length = $5 \mu\text{m}$, source-drain doping concentration = 1×10^{20} , substrate doping concentration = 1×10^{17} , and the drain voltage = 3.0V . (a) Drain current as a function of junction depth; (b) Change of Drain current as a function of junction depth.

In this report, we investigate drain current and its percentage of change as a function of change in applied stress in the MOSFET.

Figure 3.12 (a) shows that the drain current increased under stress as the applied stress increased. In Figure 3.12 (b), the changes in drain current also increased with increasing applied stress.

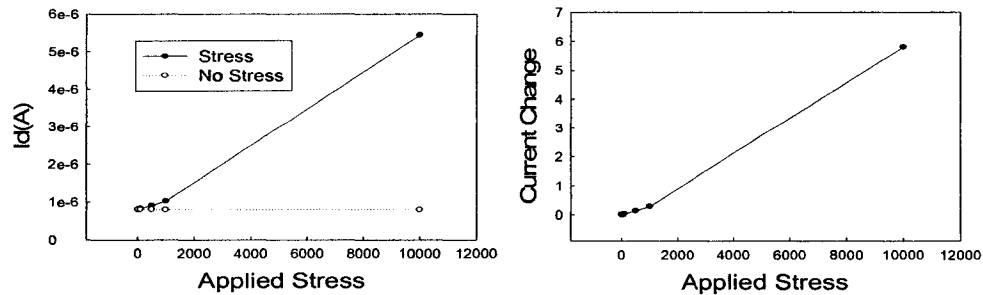


Figure 3.12 The whole MOSFET with length = $10\mu\text{m}$, channel length = $5\mu\text{m}$, substrate doping concentration = 1×10^{17} , source-drain doping concentration = 1×10^{20} , junction depth = $0.2\mu\text{m}$, and the drain voltage = 3.0V , (a) Drain current as a function of applied stress. (b) Change of Drain current as a function of applied stress.

From Figure 3.13, we can find that the drain current increased linearly with increasing MOSFET Width. As a matter of fact, the 2D simulation is based on the assumption that the MOSFET Width of the 2D MOSFET model is $1\mu\text{m}$. Therefore, in order to achieve higher drain current, the MOSFET width should be increased.

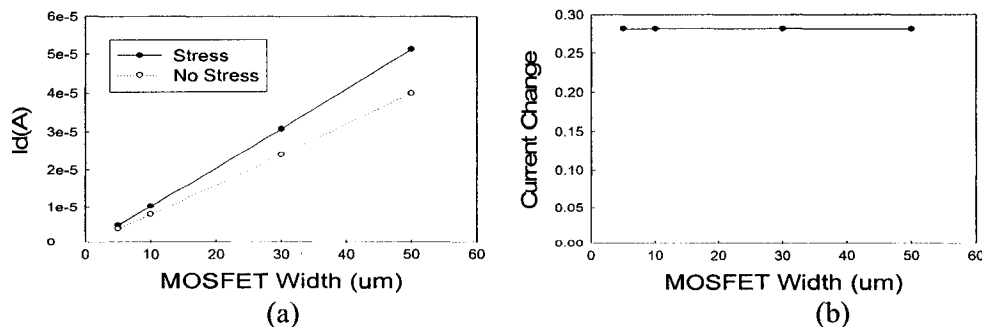


Figure 3.13 The whole MOSFET with length = $10\mu\text{m}$, channel length = $5\mu\text{m}$, substrate doping concentration = 1×10^{17} , source-drain doping concentration = 1×10^{20} , junction depth (Y) = $0.2\mu\text{m}$, and the drain voltage = 3.0V , (a) Drain current as a function of MOSFET Width (Z direction); (b) Change of Drain current as a function of MOSFET Width (Z direction).

Figure 3.14 shows I_d - V_d curve for a stress=100 MPa, on the whole MOSFET with length =4 μ m, channel length =2 μ m, substrate doping concentration =3e17, source-drain doping concentration =3e20, junction depth =0.2 μ m. While the drain voltage =3.0V, in figure 3.14, the $I_d(s)$ = 1.5090e-6, $I_d(ns)$ = 1.4598e-6; the current change between stress and no stress is 3.8%. Compared to the experimental results mentioned by T. Chen et al. [45] and R. C. Jaeger et al. [46], which showed that the drain current change of PMOS [110] under compressive stress of 60 MPa and 22.5 MPa is about 2.6% (figure 3.15a) and 1.5% (figure 3.15b), respectively, our simulation results have the same level change and appears reasonable. Actually, the mechanical stress applied on the cantilever caused by low level moisture, such as 1-10 ppm, is far less than 100 MPa, resulting in an extremely small relative saturation drain current deviation which is difficult to be detected.

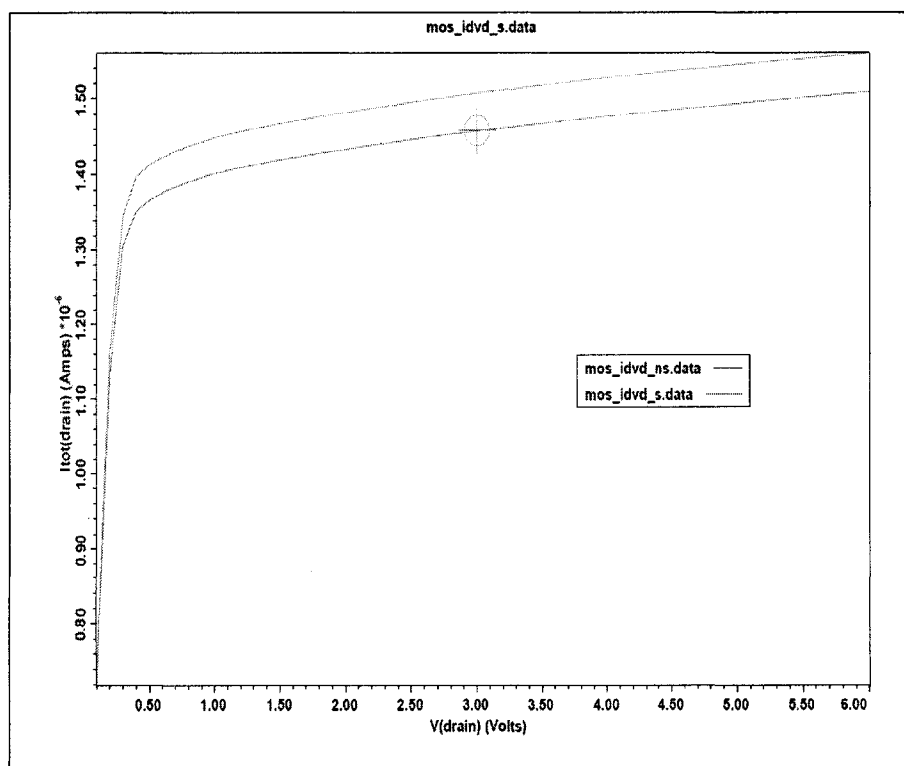


Figure 3.14 I_d - V_d curve.

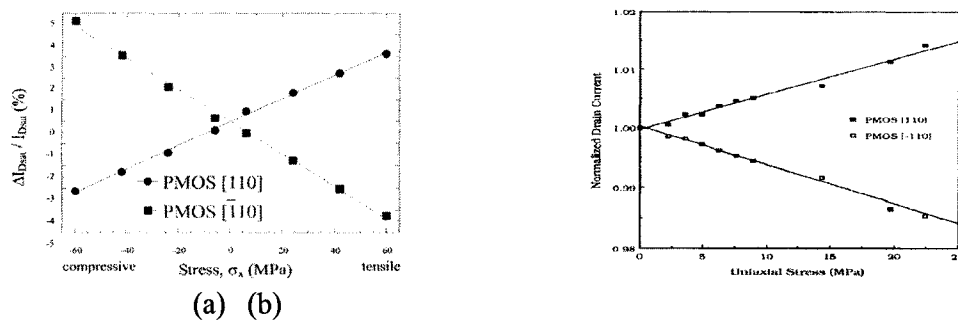


Figure 3.15 Drain current change mentioned by (a) T. Chen et al; (b) R. C. Jaeger et al.

3.3 Investigation of Frequency Mode

3.3.1 Experimental Investigation

Since higher sensitivity is achieved from low mass resonators, and, microcantilever sensors operating in the frequency mode are essentially low mass mechanical oscillators, it could be expected that a microcantilever operating in the frequency mode would possess high sensitivity as a moisture sensor. A basic block diagram of the moisture sensor using a microcantilever operating in the frequency mode is shown in the figure 3.16.

The basic principle of operation of a micro-cantilever (32kHz) based moisture sensor is detecting the resonance frequency of the cantilever due to the absorbance of moisture by the alumina surface. As shown in figure 3.16, an alumina modified micro-cantilever is placed into a glass flow cell which holds the cantilever. This glass flow cell is placed in an Atomic force microscopy (AFM) scanner which consists of PZT material on the scanning tube. An optical laser light, emitted by the AFM is focused on cantilever tip and the position is reflected back to the position sensitive photodiode. The optical signal from the position sensitive photodiode is converted into an electrical signal. The signal conditioning i.e., amplification and filtering is

done by the amplifier. Frequency analyzer (HP 3460A) shows the respective sharp frequency peak before and after moisture injection. The microcantilever oscillates at its resonance frequency and when there is an increase in the mass of the cantilever due to the absorbance of moisture, it bends, thereby changing the resonance frequency. This change in resonant frequency and change in surface stress of the cantilever is detected by a position sensitive photodiode measured by a frequency analyzer (HP 3460A) and HP data logger after signal conditioning.

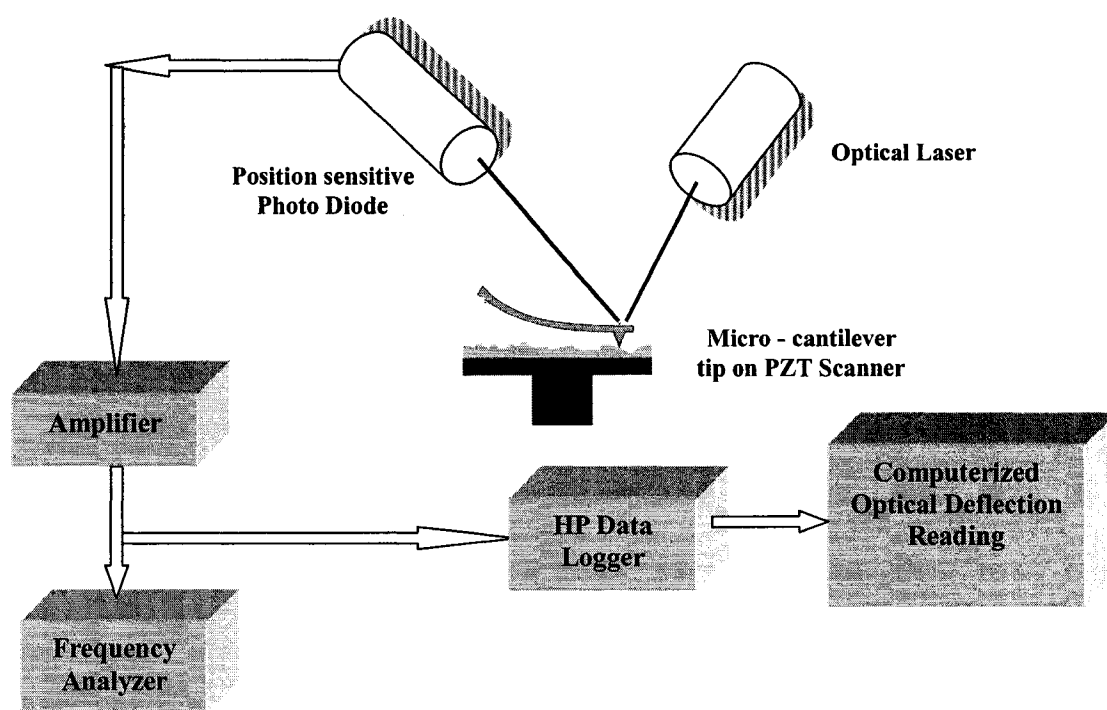


Figure 3.16 Block Diagram of the micro cantilever based Moisture Sensor.

The response of the commercial silicon cantilever in terms of resonant frequency was initially tested for low levels of moisture. This test confirms the presence of a spontaneous and significant reduction in resonant frequency of the microcantilever with the change in moisture levels. The spontaneous decrease in frequency that was observed for different moisture levels are shown in Figure 3.17. For the cantilever as

shown in Figure 3.17, the initial resonant frequency was at 25575 Hz and its resonance frequency was decreased to 25025 Hz at 200 ppm level and gradually increased and reached its initial frequency with the increase in moisture levels. This decrease in resonance frequency to the different levels of moisture content confirms the ability of microcantilever in response to show significant resonant frequency change for low levels of moisture content.

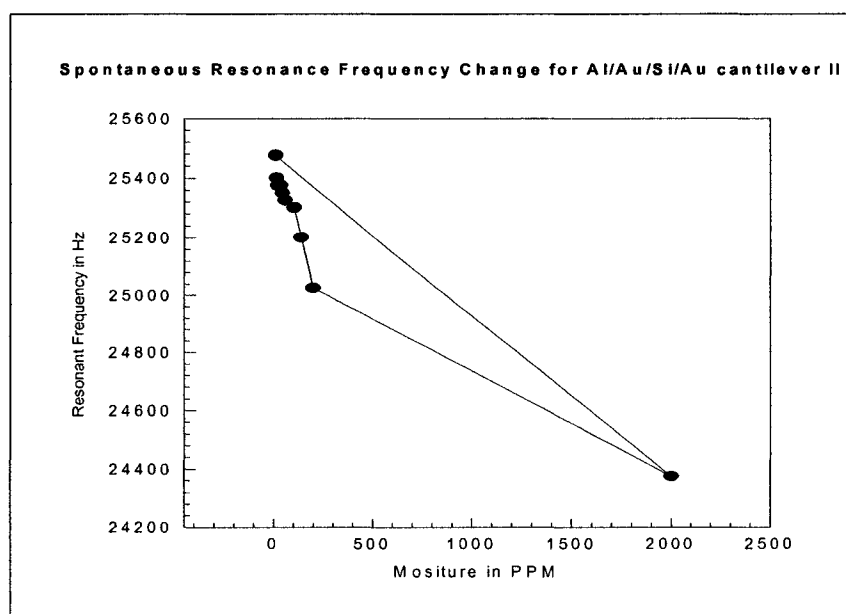


Figure 3.17 Al modified Au/Si/Au cantilever II using anodization method shows the presence of spontaneous and stable decrease in resonant frequency to the randomly injected moisture levels. Initial Frequency: 25475 Hz; Final Frequency: 25025 Hz; 450 Hz change in resonance frequency at 200 ppm level of injected moisture.

3.3.2 Simulation Investigation

The simulation of the frequency deviation of the Al_2O_3 modified piezoelectric microcantilever was also conducted by using ConvectorWare in IfM's simulation lab. The piezoelectric microcantilever is designed for the purpose of detecting and actuating the microcantilever operating in the resonant mode. The structure of its beam is presented in figure 3.18 and the thicknesses of its different layers are given in table 3.1.

Different thicknesses for the silicon beam layer were brought into our simulation to observe the relationship between beam thickness and its sensitivity. In the simulation, the density of the Al₂O₃ sensing layer was changed to correspond to the mass shift of this layer caused by water absorption on the surface of the Al₂O₃ layer. The results are shown in table 3.2.

Table 3.1 Piezoelectric microcantilever layers design for simulation

Silicon Beam layer	from 1 to 3 um
SiO ₂ insulator layer	30nm
Bottom gold electrode layer	30 nm
ZnO piezofilm layer	400nm
Top gold electrode layer	30nm
SiO ₂ insulator layer	30nm
Al ₂ O ₃ sensing layer	50nm

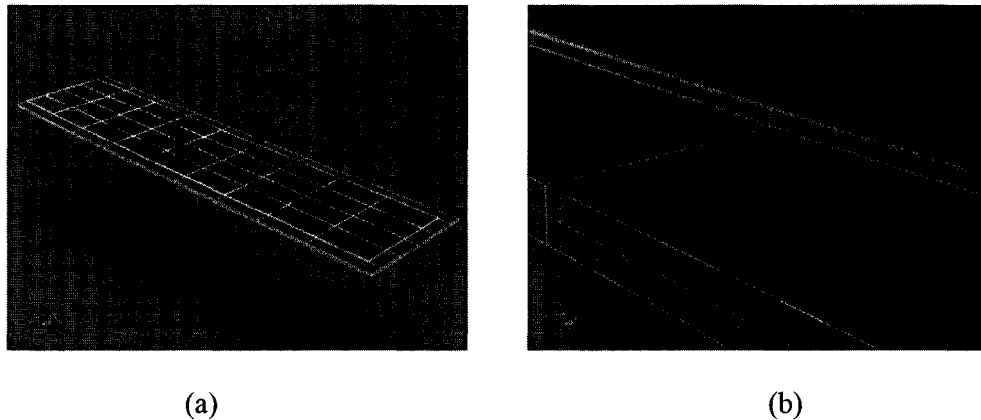


Figure 3.18 (a) Beam structure of the piezoelectric microcantilever; (b) Magnified part of cantilever beam.

According to table 3.2, the sensitivity goes up with increasing beam thickness, and a 2.9717×10^{-12} grams change in mass can cause a one hertz shift in the resonant frequency of this microcantilever. In fact, in terms of our experimental results, 200 ppm level of moisture could cause a 41.76×10^{-11} grams change in the mass of the alumina modified surface of the cantilever. Thus, it could be expected that this Al₂O₃ modified microcantilever possess the ability to detect moisture at very low levels. According to

both experimental and simulation results, the Al_2O_3 modified microcantilever, operating in dynamic mode, can be employed as the potential moisture sensor in our project.

Table 3.2 Simulation results of different cantilever beam thickness

Beam Size	Initial Resonance Frequency f_0 (Hz)	Changed resonance frequency f_1 (Hz)	Sensitivity (g/Hz)
200X100X1 um	5.73e04	5.71e04	3.12e-12
200X100X2 um	9.59e04	9.57e04	2.99e-12
200X100X3 um	1.33e05	1.33e05	2.97e-12

CHAPTER FOUR

ISOTROPIC ETCH WITH ICP FOR MICROCANTILEVER

RELEASE

4.1 Introduction

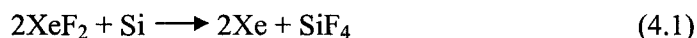
As we mentioned previously, the SiO₂ cantilever beam has a higher sensitivity compared to the Si beam based on the optical method. Therefore, the SiO₂ cantilever was chosen to be fabricated for our existing optical system.

In the fabrication of micromechanical freestanding microstructures and microcantilevers, a critical etching step is the release of the suspended microstructures at the final stage. Wet etching is usually involved in the fabrication of microcantilever structures for releasing the cantilever beam from the substrate. However, surface tension-induced stiction during the release and the drying step is a big challenge for the wet etching process. Although some preventive measures are taken to avoid this problem [47], the processing conditions are hard to control [33], especially for the fabrication of SiO₂ microcantilevers, due to the low etching selectivity of SiO₂ : Si using either KOH or EDP etchants. This makes it inefficient to release relatively large sacrificial layers as required for microcantilevers or microbridges.

4.1.1 Vapor phase dry etching without plasma

An alternative solution is the Silicon Sacrificial Layer Dry Etching method [48]. In this process, single crystal, polycrystalline or sputtered amorphous silicon sacrificial

layers are isotropically dry etched in a XeF₂ vapor phase reaction chamber, which does not require a plasma to generate the etching species. A typical XeF₂ vapor phase etching system configuration is shown in figure 4.1. XeF₂ is a white solid with a room-temperature vapor pressure of about 4 Torr, which reacts readily with Si. The Si etch occurs in the vapor phase at room-temperature and at pressures between 1 and 4 Torr, which is established by a vacuum pump throttled to the right pressure. The etch process has the following steps. First, the expansion and etching chambers are evacuated to pressures below 1 mTorr. After disconnecting the expansion and etching chambers from each other, the expansion chamber is filled with XeF₂ gas by connecting it to the XeF₂ crystal chamber. When the pressure inside the expansion chamber reaches the desired value (approximately 3 Torr), the expansion chamber is disconnected from the crystal chamber. Silicon etching starts when the etching chamber is connected to the expansion chamber. To stop the etch, the etching chamber is evacuated to a pressure below 1 mTorr. The exothermic etch reaction is given by:



with only Si in the solid phase.

The extreme selectivity of XeF₂ to silicon over silicon dioxide and silicon nitride are well reported as a main advantage from a process perspective. A vapor phase etching system is often described as an inexpensive technique, from a hardware perspective, since it does not use any power supply for plasma generation. However, it requires more sophisticated gas handling hardware for low pressure and hazardous gas materials, and also utilizes costly gas forming material (the cost of high purity XeF₂ crystal was estimated at about \$15 per gram in 2003) [48]. Unlike plasma etching, it has different parameters, such as undercut rate, etch rate or etch depth, that are more difficult to control because of the simplicity of the gas phase etching process [49]. Hence, vapor

phase etching is generally unsuitable when the etching accuracy is critical. In addition, one crucial problem is that water and HF, which may unintentionally react with SiO_2 , are formed because XeF_2 reacts with water [50].

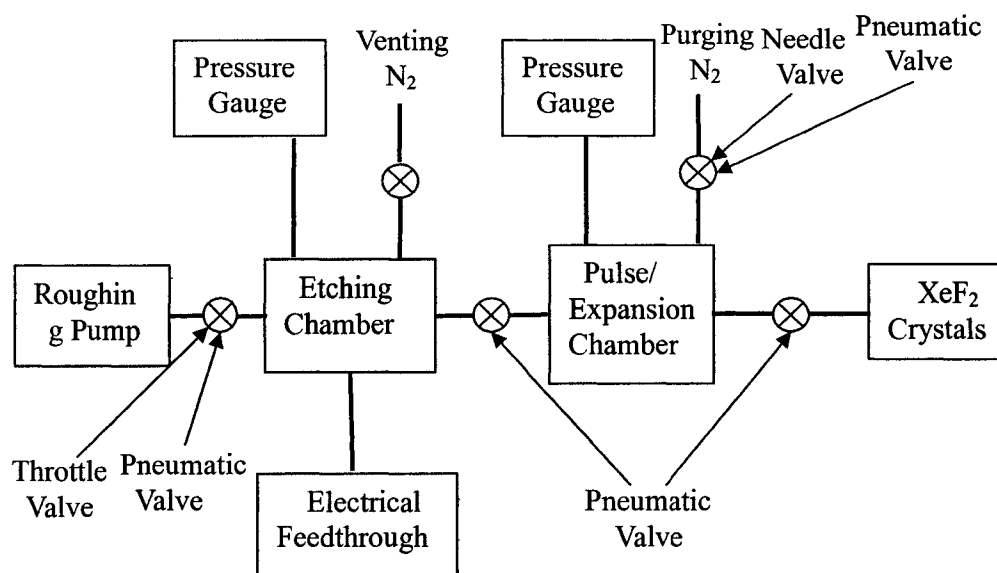


Figure 4.1 A schematic representation of a XeF₂ Vapor Phase etching system.

In addition to the two methods mentioned above, microcantilevers are normally formed by using a silicon anisotropic dry etching release process from the backside of the wafer. Silicon dry etching technology has been used as a standard method for the fabrication of large-scale integrated circuits and MEMS over the last 20 years. Considerable effort has been devoted to the high aspect ratio anisotropic etching properties of radio-frequency (RF) inductively coupled plasma (ICP), especially on ways to diminish or eliminate the isotropic influence during processing [51], [52], [53]. To completely release the cantilever beam, the anisotropic dry etching must go through the 500- μm -thick sacrificial silicon from the backside of the wafer. Common photoresist can not be used as an etching mask in this processing because the ion or

electron bombardment will destroy the mask layer during the long processing time. Therefore, the etching mask material must be carefully selected.

In our present work, we developed a dry isotropic plasma etching process using ICP for front-sided releasing of the cantilever beam. In our special mask design, the SiO₂ cantilever beams were completely covered by photoresist, and have been released intactly with a high etch rate of about 9.1 μm per minute. The investigations in this work covered the effects of chamber pressure, ICP plasma source power, substrate power, and SF₆ flow rate on the etch rate, undercut rate, and isotropic ratio.

4.2 Configuration and principle of ICP operation system

At the Louisiana Tech University Institute for Micromanufacturing (IfM), a high-density ICP system (Alcatel 601E, figure 4.2) [54], [55] was used in these experiments. Figure 4.3 illustrates the construction of the process module itself. The plasma was generated by a 13.56 MHz RF power supply and diffused down to a low pressure chamber where a <100> wafer was processed. Ion energy was independently controlled from the ion flux by RF power applied to the chuck. The wafer was mechanically clamped on the wafer chuck, which was cooled with liquid nitrogen and thermally regulated with a heating element. The temperature can be adjusted from -180 °C to 50 °C. A pressure controlled helium film ensures better heat transfer between the chuck and the wafer. A load chamber optimizes load/unload processing of the wafer without breaking the process chamber vacuum.

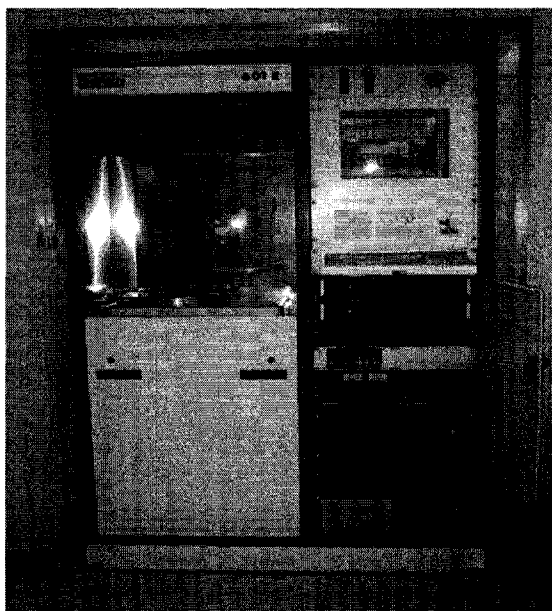


Figure 4.2 Alcatel system 601E

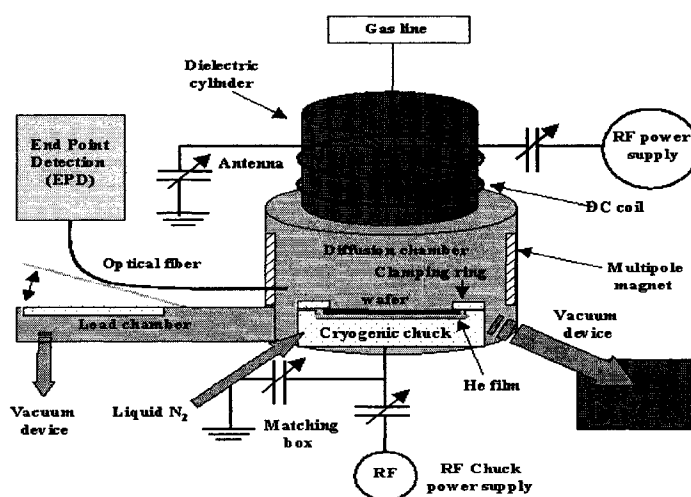


Figure 4.3 Schematic view of Alcatel system 601E process module

4.3 Scanning Electron Microscopy

A scanning electron microscope (SEM) system was employed to characterize the etching profile in this experiment. The SEM (Figure 4.4) generates a beam of electrons from a (Tungsten, LaB₆ or field emission) filament in a vacuum chamber. The beam is

collimated by electromagnetic condenser lenses, focused by an objective lens, and scanned across the surface of the sample by electromagnetic deflection coils. The primary imaging method is by collecting secondary electrons that are released from the sample surface. The secondary electrons are detected by a scintillation material that produces photons from the electrons interacting with the detector. The photons are then detected and amplified by a photomultiplier tube.

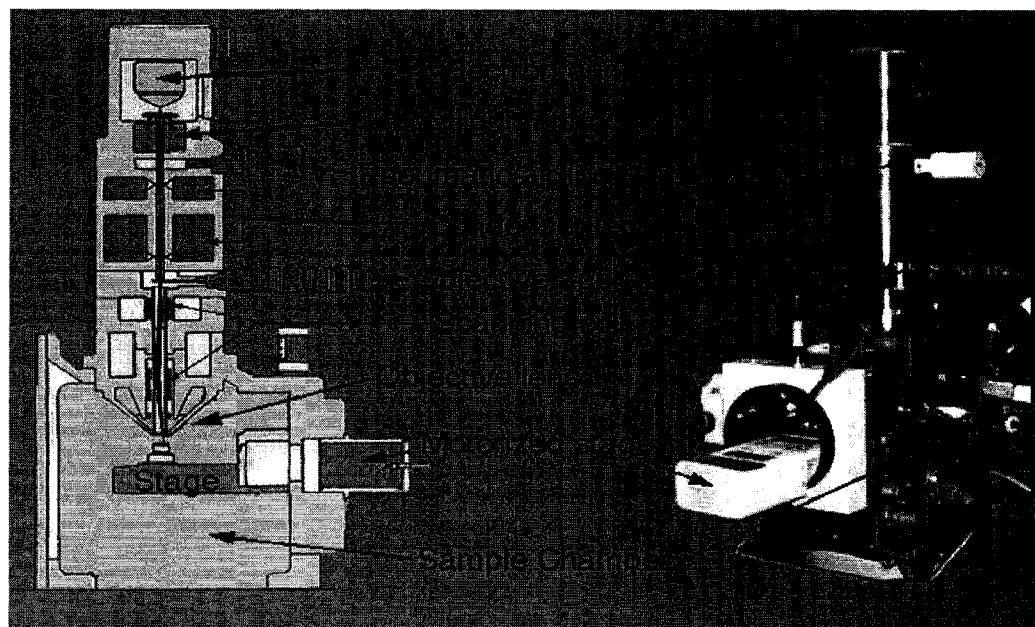


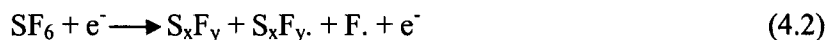
Figure 4.4 Schematic illustration of the SEM [56].

The scanning electron microscope (SEM) uses accelerated electrons instead of visible light which is used in optical microscopes. Optical microscopes have their resolution limited by the diffraction of light. Visible light has wavelengths from 400 to 700 nanometers, while electrons accelerated to 10,000 KeV have a wavelength of 0.12 Angstroms. Hence, the scanning electron microscope breaks through the resolution limitation of optical microscopy. Moreover, the large depth of field of the SEM produces images with a 3D effect.

The SEM requires a conductive sample surface and a vacuum chamber. These disadvantages limit the application of the SEM.

4.4 Experimental Setting

The Bosch process [57], [58] is one of the widely accepted processes for anisotropic etching, especially in an ICP system. Through alternate etching and passivation steps, this process can achieve high aspect ratio single crystal silicon structures with vertical sidewalls [59]. A schematic diagram of Bosch process is demonstrated in figure 4.5. Briefly, the process starts with an etching step under a low pressure SF_6 plasma generated from an RF source. Fluorine radicals generated in the SF_6 plasma react with silicon to form volatile SiF_x . The equations, which indicate the mechanism that F uses to etch silicon, is presented as follows:



Then a passivation step allows C_4F_8 gas molecules to dissociate and form an ultrathin polymeric layer over all the exposed silicon surface. In the subsequent etching step, this layer is preferentially etched on the horizontal surface rather than on the sidewalls. These steps are repeated until a desired silicon layer etching process is completed. Typically, this process is terminated with a final etch step to ensure the last passivation coating is cleaned.

The silicon isotropic plasma etching procedure was modified from the standard Bosch process [60], [61]. In this modified process, the passivation step was dismissed and SF_6 was the only process gas. Because no passivation layer was formed along the sidewall of the trench, the ions reacted freely with the silicon atoms under the mask

horizontally. Isotropic etching was realized largely by ion-enhanced chemical etching after C_4F_8 was dismissed in the etching process.

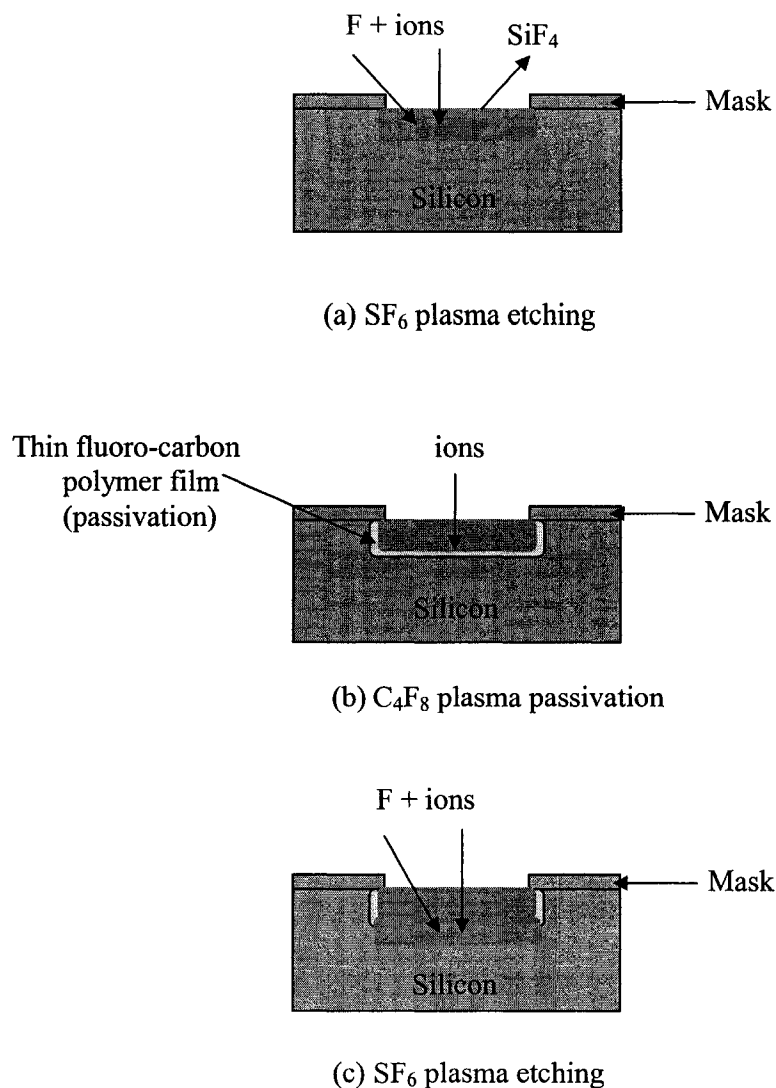


Figure 4.5 Schematic diagram of Bosch etch process.

In order to investigate the isotropic plasma etching properties of the ICP system, two masks were used in the experiments. The wafer substrate was $520\ \mu\text{m}$ in thickness, with $1\ \mu\text{m}$ -thick SiO_2 layers on both sides. Figure 4.6 shows the pattern of the combined two masks. The dash line shadowed region was Mask 1 and the solid line shadowed area was Mask 2. Mask 1 was used to transfer the cantilever beam pattern to SiO_2 . The

width of the cantilever beam was designed at $100\ \mu\text{m}$. The Mask 2 was to pattern the photoresist, which served as an ICP etching mask, to release the SiO_2 cantilever beam from the bulk silicon. In order to protect the edges of the cantilever beam, the

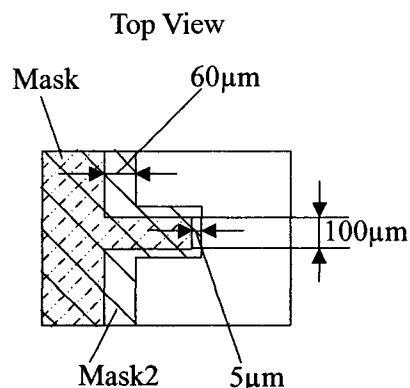


Figure 4.6 Mask pattern used to produce microcantilever beams.

photoresist pattern covering on the cantilever beam was about $5\ \mu\text{m}$ longer along the three edges than the SiO_2 beam. This also compensated for any slight alignment errors. Therefore, the photoresist beam width was designed at $110\ \mu\text{m}$. In fact, fluorine atoms alone do not etch silicon dioxide or nitride, though it does etch these dielectrics in the presence of ion or electron bombardment and under UV radiation [62]. The SiO_2 beam could be almost unaffected because the photoresist protects it from ion or electron bombardment and UV radiation. To ensure that the cantilever beam released completely and the foot of the beam remained at the expected position after release, the photoresist pattern at the foot of beam was $60\ \mu\text{m}$ longer than in Mask 1.

The fabrication process flow for releasing the cantilevers is shown in figure 4.7. First, after baking for 30 minutes at 250°C , the wafer was spin-coated with a $1\ \mu\text{m}$ -thick layer of Shipley 1813 positive tone photoresist. Then the photoresist was patterned by the photolithography process using Mask 1 (figure 4.7(a)). Next, the SiO_2 cantilever beams were formed by wet etching with buffered oxide etchant (BOE $\text{HF}:\text{NH}_4\text{F}=1:6$ in volume). Then the photoresist was removed from the surface of the wafer (figure 4.7b).

A 3 μm thick layer of photoresist 1813 was spun onto the wafer and patterned with Mask 2 (figure 4.7(c)). Finally, the isotropic etching processing was conducted in the ICP system to release the cantilever (figure 4.7(d)).

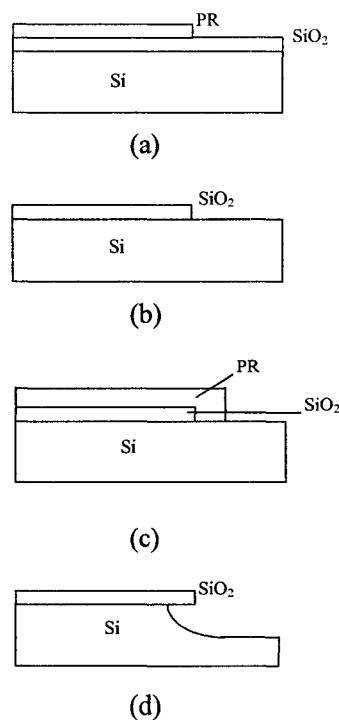


Figure 4.7 The process sequence for the experiment. (a) Resist lithography (b) BOE etching (c) Resist lithography for cantilever beam release (d) Isotropic etching for 10 minutes.

For the best result of cantilever beam release, the isotropic etching process was investigated with a series of 16 recipes. Each processing was initiated with an oxygen cleaning process to remove impurities in the chamber, which would influence the isotropic etching. This cleaning step was applied on a dummy wafer for 10 minutes. The chamber preconditioning process was followed after 10 minutes with the next recipe. Next, a processing substrate was loaded into the system for isotropic etching. Pure SF₆ was the only process gas used for silicon isotropic etching. A 10-minute etching time was used for all testing processes in these experiments in order to compare

the process parameters for isotropic etching. The process parameters varied over the following ranges: chamber pressure (14-66 mTorr), ICP source power (800-1800 W), substrate power (0-30 W), and SF₆ flow rate (150-300 sccm).

The profiles of the released cantilevers were observed by SEM. The resulting SEM images were analyzed using Matlab software. The etching depths were measured by a KLA tencor profilometer (TENCOR Alpha step 500 profiler; TENCOR Inc.) with a precision of $\pm 0.01 \mu\text{m}$.

4.5 Results and Discussion

Figure 4.8 (a, b) shows a SEM images of the cross section of an etched trench at the center of the wafer and at the edge (about 7 mm from the wafer edge) of the wafer after isotropic etching. The microcantilever beams were successfully released (figure 4.9). Table 4.1 lists the details for the processing testing recipes and testing results.

Table 4.1 showed that the chamber pressure, ICP source power, ICP substrate power, and SF₆ flow rate did affect the cantilever profiles, which will be discussed in detail in the following sections.

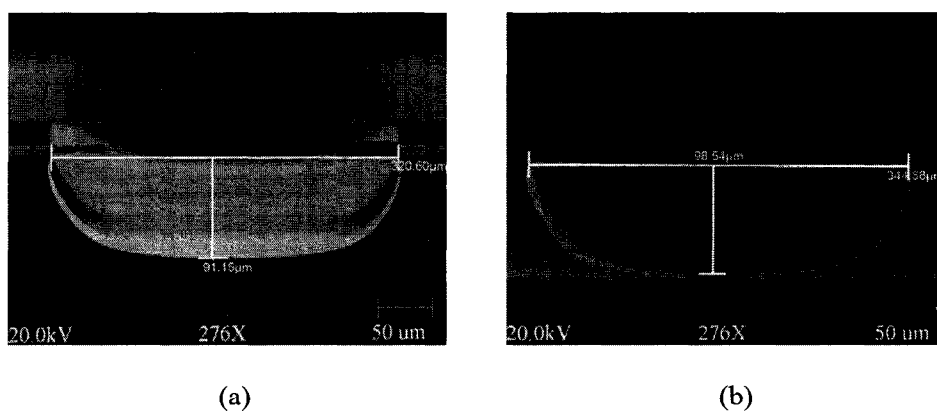


Figure 4.8 SEM images of the cross section of etched trenches. The mask opening was 200 μm in width, and the etching time was 600s. (a) A trench near the **center** of the wafer. (b) A trench at the **edge** of the wafer. The parameters of the etching process were as follows: Pressure = 46 mTorr, Source Power = 1800 W, Substrate Power = 20 W, SF₆ = 300 standard cubic centimeters per minute (sccm).

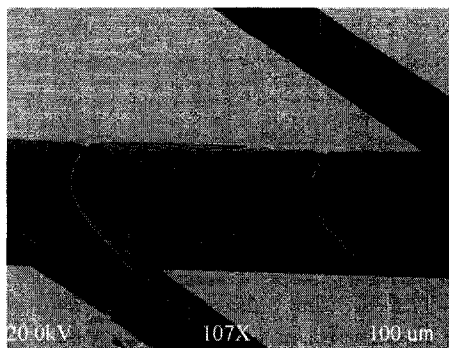


Figure 4.9 SEM image of the released cantilever beams.

4.5.1 Chamber Pressure

The chamber pressure has a great impact on the plasma isotropic etching results, as shown in figure 4.10. Both the etch rate and undercut rate increased as the pressure was increased from 14 to 46 mTorr. At higher pressures, the etch rate kept the same but the undercut rate dropped slightly (figure 4.10(a, b)). Under the pressure range from 14 to 46 mTorr, the increases in etch rate and undercut rate were due to the higher plasma density (especially the higher number of fluorine radicals) in the chemical reaction at higher pressure [63], [64]. When the pressure was higher than 46 mTorr, the chemical reaction tended to be saturated and higher pressure would increase the collision frequency, which resulted in the reduction of ion energy [64].

The isotropic ratio, A , in table 4.1, was defined as

$$A=x/y, \quad (4.6)$$

where x is the horizontal dimension extent of the foot edge from the mask edge, or the undercut rate, and y is the vertical etched depth, or the etch rate.

The ratio of undercut rate over etch rate gave an isotropic ratio, as shown in Figure 4.10(c). The highest isotropic ratio appears at 23 mTorr. In the 14-23 mTorr range, the isotropic ratio increased when the pressure increased, indicating that the enhanced

chemical reaction rate exerted more impact on the undercut rate than on the etch rate.

Above 23 mTorr, the isotropic ratio decreased when the pressure increased, showing a

Table 4.1 Process parameters and etching profiles.

Recipe ID	1	2	3	4	5	6	7	8	9	10	11	12	13	14	15	16
Pressure (mTorr)	14	18	23	28	35	46	66	46	46	46	46	46	46	46	46	46
Source Power(W)	1800	1800	1800	1800	1800	1800	1800	800	1000	1500	1800	1800	1800	1800	1800	1800
Substrate Power(W)	30	30	30	30	30	30	30	30	30	30	0	10	20	30	30	30
Flow rate SF ₆ (sccm)	300	300	300	300	300	300	300	300	300	300	300	300	300	150	200	250
Chuck temperature (°C)	20	20	20	20	20	20	20	20	20	20	20	20	20	20	20	20
Etch depth y at center(μm)	56	59	61	65	81	91	91	42	62	82	82	81	91	57	70	86
Etch depth y at edge(μm)	59	62	67	72	92	103	104	47	71	90	94	87	99	63	75	93
Undercut x at center(μm)	35	38	48	50	58	59	54	31	44	54	52	51	60	46	53	58
Undercut x at edge(μm)	36	39	53	54	63	68	65	28	50	57	67	55	72	47	54	60
Etch Uniformity	0.95	0.95	0.91	0.90	0.88	0.88	0.88	0.90	0.87	0.91	0.87	0.93	0.92	0.91	0.94	0.93
Etch rate at center(μm/m)	5.6	5.9	6.1	6.5	8.1	9.1	9.1	4.2	6.2	8.2	8.2	8.1	9.1	5.7	7.0	8.6
Undercut rate(μm/m)	3.5	3.8	4.8	4.7	5.8	5.9	5.4	3.1	4.4	5.2	5.2	5.1	6.0	4.6	5.3	5.8
Isotropic ratio at center	0.63	0.64	0.79	0.77	0.72	0.65	0.60	0.74	0.71	0.66	0.63	0.63	0.66	0.81	0.76	0.67
Isotropic ratio at edge	0.61	0.63	0.79	0.75	0.68	0.66	0.63	0.60	0.71	0.63	0.71	0.63	0.73	0.75	0.72	0.65

decreased difference between undercut and etch rates. The interactions of the reactive plasma with surfaces often involves two components: physical and chemical interactions. The lateral etch rate (undercut rate) mainly depends on the horizontally oriented chemical plasma reaction with the silicon substrate reported by Jae-Ho Min etc [60]. Both the physical and the chemical etching contribute to the overall etch rates, especially in the vertical direction [60]. These results suggested that the physical etching rate in the vertical direction increased faster than in horizontal direction when the pressure was higher than 23 mTorr.

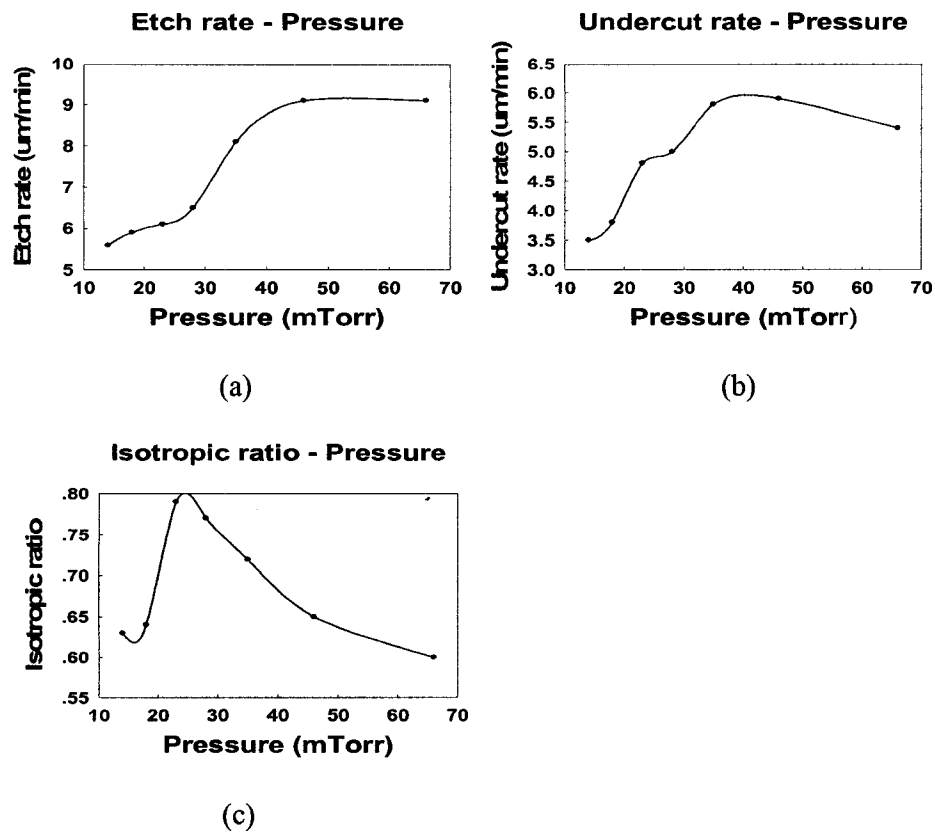


Figure 4.10 Silicon isotropic etching profiles as a function of pressure: (a) Etch rate. (b) Undercut rate. (c) Isotropic ratio. The source power and substrate power were set to 1800 W and 30 W, respectively. The SF₆ flow rate was set to 300 sccm.

4.5.2 ICP source power

Figure 4.11 shows the plasma isotropic etching profiles as a function of ICP plasma source power. It was found that an increase in the ICP source power increased the etch rate and undercut rate (figures 4.11(a) and (b)). It has been reported that an increase in the ICP source power would produce a large number of electrons with higher energy for dissociation and ionization [63], which would create higher concentrations of reactive species and higher ion flux. These more reactive species would increase the bond breaking and desorption efficiency. In these experiments the etch rate increase was faster than the undercut rate when the plasma source power was increased. This resulted in a decrease of the isotropic ratio as the source power increased (figure

4.11(c)). The figure 4.11(c) can also be explained by a difference of physical etching influence between horizontal direction and vertical direction with the plasma density rising.

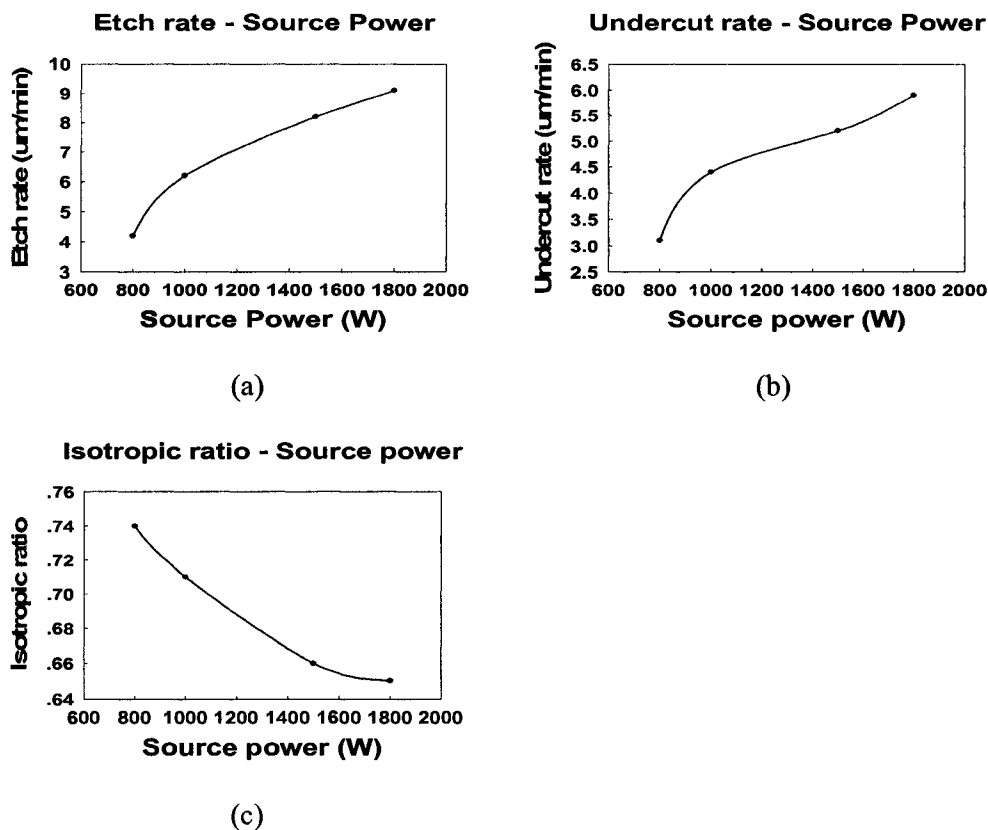


Figure 4.11 Silicon isotropic etching profiles as a function of plasma source power: (a) Etch rate. (b) Undercut rate. (c) Isotropic ratio. The pressure, substrate power, and SF_6 flow rate were set to 46 mTorr, 30 W, and 300 sccm, respectively.

4.5.3 Substrate power

Figure 4.12 shows the plasma isotropic etching properties as a function of substrate power. An increase in the substrate power applied to the wafer had no significant impact on the etch rate and undercut rate due to the fact that the fluorine ion density in the plasma area surrounding the wafer was almost independent of substrate power [61], [64]. A slight increase of etch rate and undercut rate from 10 to 20 W (figure 4.12(a) and (b)) may be due to an increase in the ion bombardment energy [64], which allows the

fluorine radicals to react with silicon more efficiently. The isotropic ratio also increased slightly when the substrate power was increased from 10 to 20 W, as shown in figure 4.12(c).

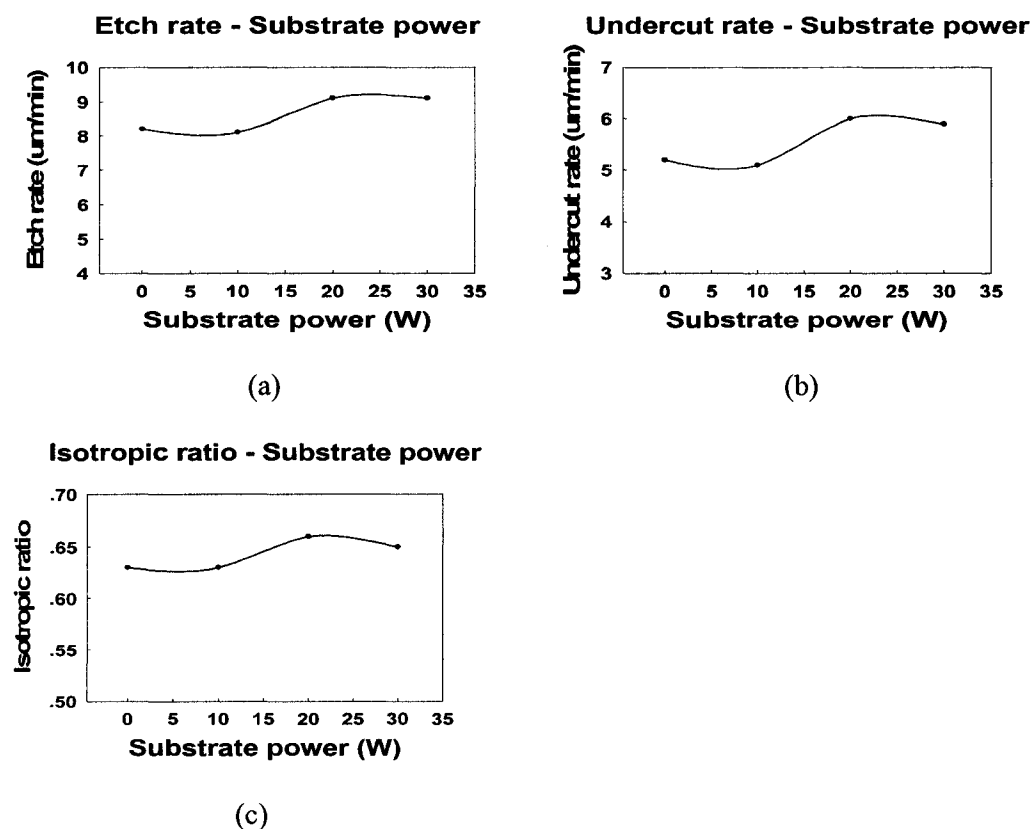


Figure 4.12 Silicon isotropic etching profiles as a function of substrate power: (a) Etching rate. (b) Undercut rate. (c) Isotropic ratio. The chamber pressure, source power, and SF₆ flow rate were set to 46 mTorr, 1800 W, and 300 sccm, respectively.

4.5.4 SF₆ flow rate

Figure 4.13 shows the etch rate, undercut rate, and isotropic ratio as a function of SF₆ flow rate. A linear increase was observed in etch rate and undercut rate with increasing SF₆ flow rate from 150 to 250 sccm. This indicated that an increase of the SF₆ flow rate contributes to an increase in the number of SF₆ molecules that produced more fluorine radicals and resulted in an increase in etch rate and undercut rate. At 300 sccm flow rate, the etch rate and undercut rate were saturated because of a) insufficient

source power to promote the dissociation of SF_6 and produce fluorine radicals and/or b) the recombination of radicals before reaching the sample surface [65]. The isotropic ratio decreased with increasing SF_6 flow rate (figure 4.13©) since the speed of increase of the undercut rate was slower than that of the etch rate, which was similar to the effect of source power, i.e. the plasma density increase resulted in a faster physical etching reaction in the vertical direction than in the horizontal direction.

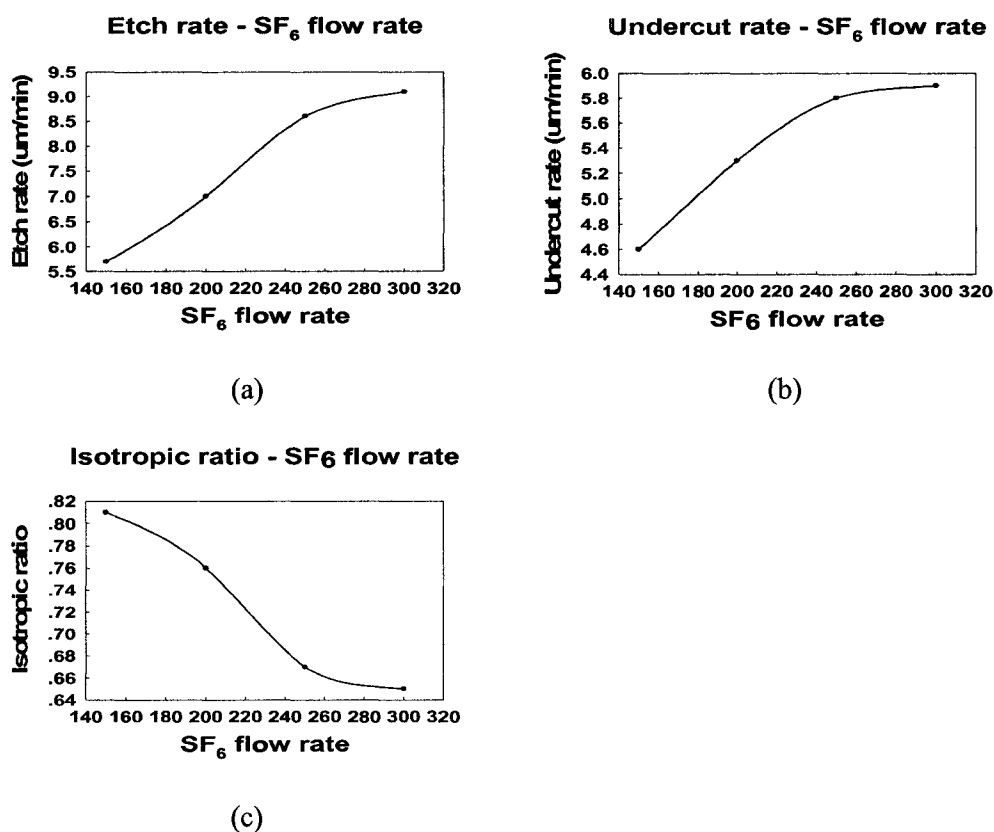


Figure 4.13 Silicon isotropic etching profiles as a function of SF_6 flow rate: (a) Etch rate. (b) Undercut rate. (c) Isotropic ratio. The chamber pressure, source power, and SF_6 flow rate were held constantly at 46 mTorr, 1800 W, and 300 sccm, respectively.

4.5.5 Comparison with traditional RIE

Compared to the traditional reactive ion etching (RIE) configuration, certain advantages for the ICP for isotropic etching can be expected. In an ICP configuration,

there is only a weak coupling between the acceleration of the ions and the plasma power as compared to the capacitively coupled plasma (CCP) configuration of RIE. In an ICP system the plasma is energized by radio frequency in a magnetic field, which accelerates the charged particles in spiralling trajectories; thus the ions only have thermal energies and an isotropic angular distribution inside the plasma. The ions are only accelerated toward the substrate over the sheath by the plasma potential. For the capacitively coupled plasma of the RIE, the acceleration of ions towards the etched surface is directly linked to the power of the plasma. An ICP etcher is equipped with a separate CCP source allowing independent control of the plasma power and the energy of the ions. Further advantages of the ICP include high etching rates and improved etching uniformity across the substrate [66].

4.6 Isotropic Etch Summary

The release of SiO₂ microcantilever beams using ICP isotropic etching and the effect of plasma etching properties on etching rate and undercut rate were investigated and discussed in this chapter. The results showed that the plasma density played a major role in the isotropic etching results, where higher plasma density would result in higher etch rate and higher undercut rate. The higher plasma density could be achieved by increasing pressure, source power, and SF₆ flow rate. One optimal recipe (recipe 13 in table 4.1) was found, whose parameters strike a balance between etch rate and isotropic ratio, for releasing the designed microcantilever beams using the isotropic dry etching process. The parameters for Recipe 13 are: 46 mTorr pressure, 1800 W source power, 20 W substrate power, 300 sccm SF₆ flow rate, and 20 °C chuck temperature. Using this recipe, a high 9.1 μm/min etch rate and a 6.0 μm /min undercut rate has been achieved. The ICP isotropic etching technology provides an excellent alternative approach to release SiO₂ microcantilever beams from a silicon substrate with low cost, high etching

rate and design flexibility.

CHAPTER FIVE

DESIGN AND MICROFABRICATION OF SiO_2

MICROCANTILEVER SENSORS

5.1 Introduction

Microfabrication of MEMS has been a subject of extensive research and development efforts over the past 25 years. The relevant microfabrication processes have been described in great detail in literature [1]-[72]. In general, fabrication of MEMS devices is based on two distinct micromachining strategies: (i) bulk micromachining and (ii) surface micromachining. Bulk micromachining involves removal of substantial portions (i.e., “bulk”) of the substrate. Bulk micromachining is often used to create devices with three dimensional (3D) architecture or suspended structures. Surface micromachining keeps the original substrate mostly intact and use it as a base for a device formed as a result of additive (deposition) and subtractive (etching) processes [67].

Although a variety of substrates and thin films can be used to fabricate microcantilever devices using bulk or surface micromachining, one of the most preferred substrates is single crystal silicon. In fact, MEMS fabrication relies heavily on approaches previously developed for microfabrication of conventional electronic devices. Silicon oxide, silicon nitride, polycrystalline silicon (polysilicon), and metal films are some of the most common films used in surface micromachining of both

MEMS[73] and more traditional microelectronic devices. As applied to microcantilever fabrication, low pressure chemical vapor deposition (LPCVD) and plasma-enhanced chemical vapor deposition (PECVD) techniques are widely used to form silicon dioxide and silicon nitride structural or sacrificial layers [67].

Typically, fabrication of suspended microstructures, such as a cantilever transducer, consists of deposition, patterning, and etching steps that define, thickness, lateral sizes, and the surrounding of the cantilever. One of the frequently used approaches in microcantilever fabrication involves deposition of a sacrificial layer on a prepatterned substrate followed by deposition of a structural material layer (such as a silicon nitride layer or a polysilicon layer) using an LPCVD or PECVD processes. By varying the conditions of these deposition processes, the stress and stress gradient in the deposited layers can be minimized so that suspended structures do not exhibit significant deformation after they are released by the etching of the sacrificial layer. The cantilever shapes can be defined by patterning the silicon nitride film on the top surface using photolithography followed by reactive ion etching (RIE). Photolithographic patterning of the structural material (silicon nitride or polysilicon) on the bottom surface is used to define the mask for anisotropic bulk etching of Si. The silicon substrate is then etched away to produce free-standing cantilevers.

5.2 Microfabrication Facilities and Process

5.2.1 Mask Design and Fabrication

Usually, mask design and fabrication are the first step in MEMS microfabrication. Device design, pattern design and process design are supposed to be accomplished before we start to draw our mask pattern using AutoCAD software or L-Edit software. Minimum feature size, pattern arrangement, uniformity, positive or negative tone

photoresist, alignment marks and bonding requirements, etc., needs to be taken into account for the mask design, just as what we have already demonstrated in chapter 4. After the mask design is finished, the mask fabrication would be started using the Pattern Generator (DWL66, Heidelberg Instruments) located in the IfM at Louisiana Tech University. Generally, photomasks consist of a square piece of flat glass of a specific type, coated with a metallic film in which the pattern is formed. A layer of sputtered Cr about 100 nm thick coats the glass plate. Resist is then spun on the plate, and the exposure is made. After development, the Cr is removed from the unprotected areas with an acid etch, and an image of the pattern is left in the Cr. The exposure can be made with either an optical or an electron beam lithography tool. Optical lithography allows you to make a mask faster, cheaper, and more easily than electron beam lithography, which writes patterns serially.

5.2.2 Photolithography

5.2.2.1 Photolithography Introduction

In the IC industry and MEMS fabrication, pattern transfer from a mask to the substrate is accomplished almost exclusively via photolithography. It is essentially the same process that is used in lithographic printing. Patterns are first transferred to an imagable photoresist layer. Photoresist is a liquid polymeric film that can be spread out onto a substrate, exposed with a desired pattern, and developed into a selectively placed layer for subsequent processing. Photolithography is a binary pattern transfer: there is no gray-scale, color, nor depth to the image. Standard photolithography process steps are described in detail as follows.

Step 1: Wafer surface preparation

Typical contaminants on the wafer surface must be removed prior to photoresist coating. The wafer could be simply cleaned by using acetone and isopropyl alcohol

(IPA). If simple cleaning proves ineffective, then nano-strip or oxide plasma etching will be considered as alternatives. Next, a dehydration bake step is necessary for drying the wafer surface, such that adhesion of the photoresist layer to the wafer surface could be promoted during the photoresist spinning process.

Step 2: Photoresist Coating

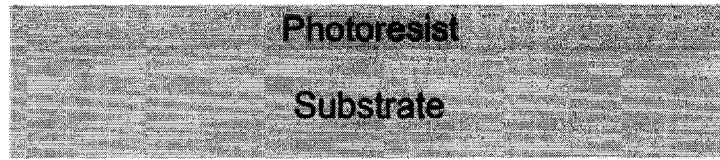
A substrate, an object onto which the image is transferred or projected, is coated with photoresist. The photoresist is the material that the image will be transferred to during the photolithography process. The coating process is typically performed by spinning the substrates at speeds between 1000 and 5000 rpm. Photoresist is deposited onto the substrate surface during this dynamic movement to ensure even coating over the entire substrate surface (figure 5.1a). Spin coating is generally regarded as the best way to deposit a uniform coating for many applications, such as photoresist coating and dielectric/insulating layer coating. The Brewer Science Cee Model 100 Spin Coating system was used for photoresist coating in IfM. Another alternative is to employ dry film photoresists which can be laminated into place to create the photo-patternable surface.

Step 3: Softbake

Once the substrate has been coated with photoresist, it is soft baked (also prebaked) in an oven or hot plate at temperatures between 100 to 120 °C. This process is called softbake. The softbake step drives off solvents, improves adhesion and anneals away stress that was introduced during the spin process.

Step 4: Exposure

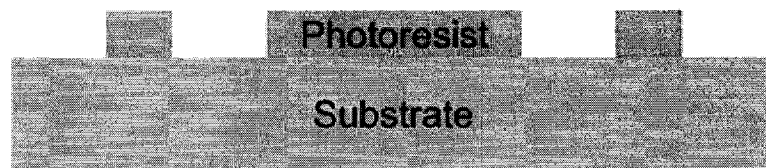
After soft baking, the substrate is then exposed on an exposure tool where the substrate is aligned with the features on the mask. For any lithographic technique to be of value, it must provide an alignment technique capable of a superposition



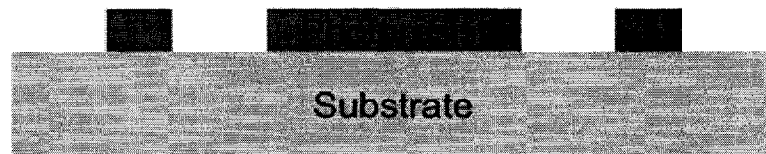
(a) A substrate coated with photoresist



(b) The photoresist coated substrate after exposure



(c) After development, the resist pattern is observed on the substrate



(d) After hardbaking the patterned substrate is chemically stable and ready for future processing.

Figure 5.1 Schematic of photolithography process

precision of mask and wafer that is a small fraction of the minimum feature size, especially in the mask design we described in chapter 4. In standard processes, the system shines UV light through a mask plate which is coated with a patterned chrome layer. This plate, termed a photomask or mask, has the master image of the device on it. By shining UV light through the mask and onto the substrate, individual areas of the photoresist are selectively exposed to light (figure 5.1(b)). This exposure causes a chemical change in the exposed areas of the photoresist, altering the solubility of the resist in a solvent either directly or indirectly via a sensitizer.

Step 5: Development

Once exposed, the substrate is then immersed in a developer solution. Developer solutions are typically aqueous and will dissolve away areas of the photoresist that were exposed to UV light. Therefore, after successful development, the photoresist is now patterned with the master image. This image formed on the photoresist will serve as a mask for further subtractive and additive steps (figure 5.1(c)).

Step 6: Hardbake

After development, the substrate is baked in an oven or hot plate at temperatures between 100 to 120 °C (figure 5.1(d)). This is needed to drive off liquids that may have been absorbed on the substrate during the development step and to crosslink the remaining photoresist. Crosslinking the polymer increases the mechanical and chemical stability of the material, allowing it to be used in further substrate processing.

The above process can be extended for use with many other photoactive materials, in addition to photoresists. Polyimides, SU-8, photoimageable ceramics, and photoimageable metals have been used successfully. The process flows for these materials is similar to that used for photoresists.

5.2.2.2 Resolution in Photolithography

Correct feature size must be maintained within a wafer and from wafer to wafer, as device performance depends on the absolute size of the patterned structures. The term critical dimension (CD) refers to a specific minimal feature size and is a measure of the resolution of a lithographic process.

In the shadow printing mode, including contact and proximity arrangements of mask and wafer, photolithography has a resolution with limits set by a variety of factors. These include diffraction of light at the edge of an opaque feature in the mask as the light passes through an adjacent clear area, alignment of wafer to mask, nonuniformities in wafer flatness, and debris between mask and wafer. Diffraction causes the image of a perfectly delineated edge to become blurred or diffused. The theoretical resolution, R , that is, the minimum resolved dimension (b_{min} for a line or a space) with a grating mask and employing a conventional resist, is given by:

$$R = b_{min} = \frac{3}{2} \sqrt{\lambda \left(s + \frac{z}{2} \right)} \quad (5.1)$$

Where b_{min} = half the grating period and the minimum feature size transferable

s = gap between the mask and photoresist surface

λ = wavelength of the exposing radiation

z = photoresist thickness

In contact printing (figure 5.2(a)), a photomask is pressed against the resist covered wafer with pressure in the range of 0.05 to 0.3 atm and s in Equation (5.1), is zero. Equation (5.1) in this case reduces to

$$R = b_{min} = \frac{3}{2} \sqrt{\frac{\lambda z}{2}} \quad (5.2)$$

In proximity printing (figure 5.2(b)), spacing of the mask away (at least 10 μm) from the substrate minimizes the defect resulting from contact. On the other hand, diffraction of the transmitted light reduces the resolution. The degree of reduction in resolution and image distortion depends on the wafer-to-substrate distance, which may vary across the wafer. For proximity printing, Equation (5.1), with $s \gg z$, can be rewritten as:

$$R = b_{min} = 3/2 \sqrt{\lambda s} \quad (5.3)$$

The practical limiting resolution R in projection printing (figure 5.2©) is given by:

$$R = k_1 \lambda / NA \quad (5.4)$$

where k_1 is an experimentally determined parameter that depends on resist parameters, process conditions, and mask aligner optics, λ represents the wavelength of the light used for the pattern transfer, and NA is the numerical aperture of the imaging lens system.

For simple contact, proximity, and projection systems, the mask is the same size and scale as the printed wafer pattern. i.e. the reproduction ratio is 1:1. Projection systems give the ability to change the reproduction ratio and offer higher resolution than proximity printing together with a large separation between mask and wafer. However, since our lithography system is a shadow printing system, there are only contact printing and proximity printing modes.

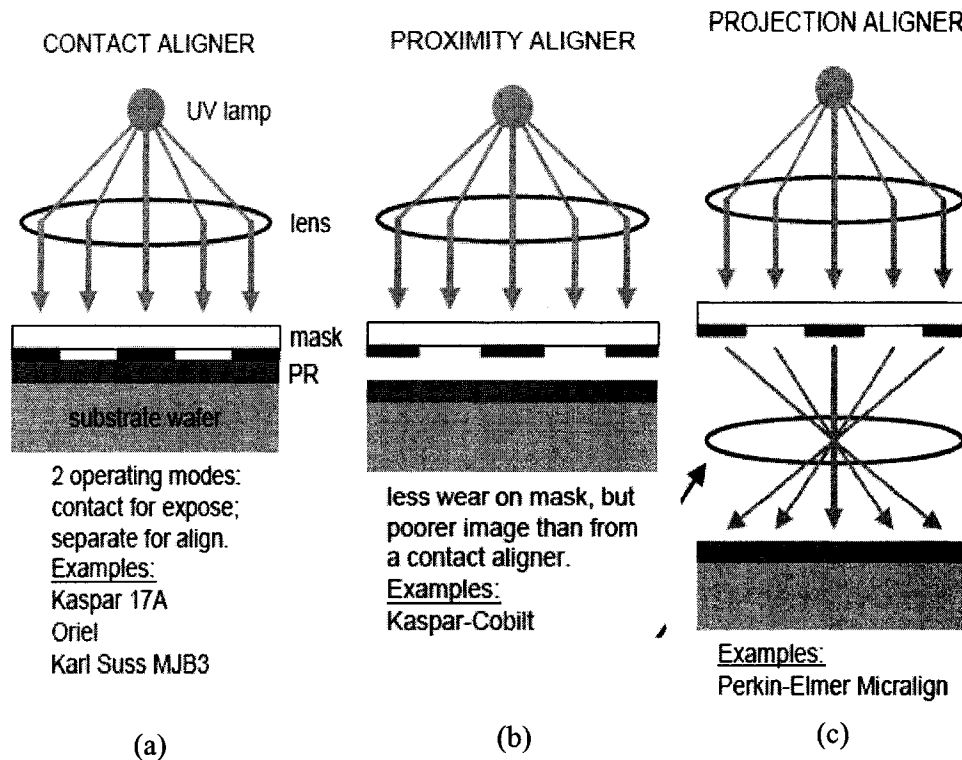


Figure 5.2 Modes of photolithography. (a) contact printing mode (b) proximity printing mode (c) project printing mode.

5.2.3 ICP Etching

ICP etching is a crucial step in MEMS fabrication including both bulk micromachining and surface micromachining. The ICP system has been described in detail in chapter 3.

5.2.4 Thin Film Deposition and Lift-off

5.2.4.1 Thin Film Deposition

In MEMS and IC fabrication, thin film depositions are required to be deposited on devices to achieve properties unattainable or not easily attainable in the devices alone. Besides the typical metal elements, MEMS fabrication also involves deposition of atypical elements such as Zr, Zn, Pt, Ag. Moreover, a plethora of exotic compounds ranging from enzymes to shape memory alloys and from hydrogels to piezoelectrics are

used. Usually, there are two types of processes get involved into thin film deposition. One is called chemical vapor deposition (CVD), the other is called physical vapor deposition (PVD). In CVD, thin film is formed by chemical reaction on the surface of substrate. In PVD, thin film is formed by atoms directly transported from source to the substrate.

Evaporation and sputtering, both of which are examples of PVD, are used to deposit many different kinds of thin films in IC and micromachine fabrication. Sputtering deposition is widely used in semiconductor and MEMS technology, and, as a result, is described in detail in literature. During sputtering, the target (a disc of the material to be deposited), at a high negative potential, is bombarded with positive argon ions (other inert gases such as Xe can be used as well) created in a plasma. The target material is sputtered away mainly as neutral atoms by momentum transfer and ejected surface atoms are deposited (condensed) onto the substrate placed on the anode (figure 5.3). Sputtering is preferred over evaporation in many applications due to a wider choice of materials to work with, better step coverage, and better adhesion to the substrate. Actually, sputtering is employed in laboratories and production settings, whereas evaporation mainly remains a laboratory technique.

During ion bombardment, the source is not heated to a high temperature, and the vapor pressure of the source is not a consideration as it is in vacuum-evaporation. The amount of material, W , sputtered from the cathode is inversely proportional to the gas pressure, P_T , and the anode-cathode distance, d :

$$W = kVi/P_T d \quad (5.5)$$

where V = working voltage

i = discharge current

k = a proportionality constant

Figure 5.3 shows a simplified RF magnetron sputter deposition system. In a typical sputter system, an inert gas, such as argon, is fed into the sputter chamber, which is at a low pressure. In DC sputtering, a voltage is applied across two parallel electrodes causing the argon to ionize, accelerating Ar^+ and e^- in opposite directions. Collisions between these charged particles and neutral Ar atoms cause further ionization, thereby generating plasma. The plasma contains neutral atoms, positive ions and free electrons. In a DC sputter system, the positive ions (the “steel balls”) in the plasma are accelerated toward the negative electrode which is conductive target material (the “concrete wall”). The energetic ions strike the target and dislodge or sputter the target atoms. These atoms are then free to travel through the plasma as vapor and strike the surface of the substrate where they condense and form the deposited film. The sputtered atoms are free to land anywhere within the deposition chamber which means the location of the substrate with respect to the target is critical.

When an insulating target is desired, a high frequency alternating voltage is coupled capacitively through the target to the plasma so that conductive electrodes are not necessary. This is known as radio frequency or RF sputtering. The frequency is chosen to be high enough so that a continuous plasma discharge is maintained. The conventional frequency is at 13.56 MHz.

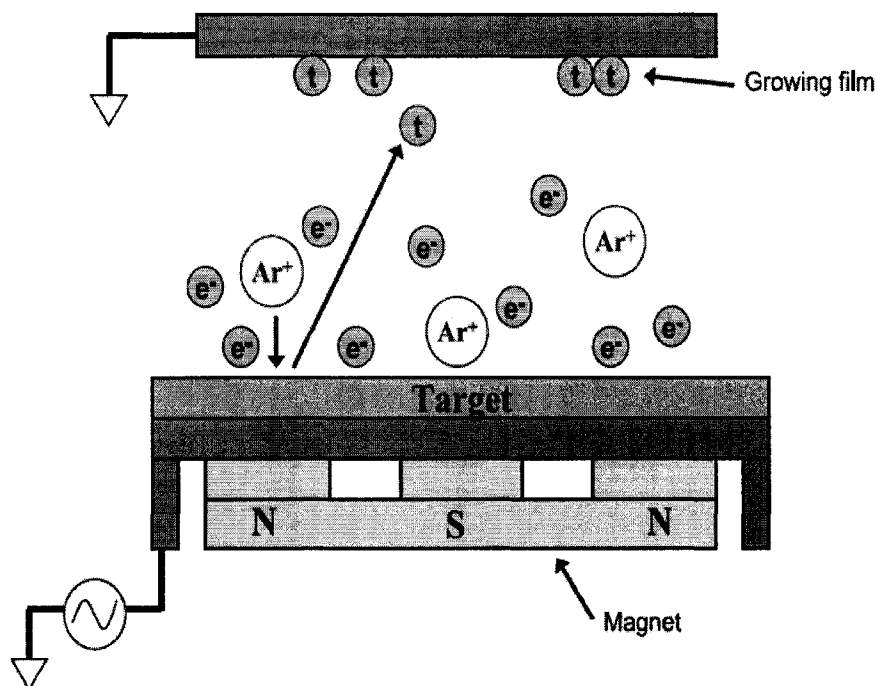


Figure 5.3 Simplified diagram of an RF magnetron sputter system. Electrons collide with gas atoms causing the atoms to ionize. These ionized atoms then bombard the target and dislodge target atoms which travel as vapor to the substrate or any other surface before condensing and forming a film.

In both DC and RF sputtering, the efficiency of ionization from energetic collisions between the electrons and gas ions is rather low. In some situations, magnets are used to confine the electrons near the target. This increases the percentage of electrons that take part in ionization events which increases the ionization efficiency. The addition of a magnetic field is known as magnetron sputtering. Usually, a magnet is placed behind the target to create a magnetic field that is perpendicular to the electric field. The electrons are then trapped near the surface of the target and are forced in a spiral motion until they collide with an argon atom. The effective increase in electrons increases the amount of argon ions which ultimately increases the sputtering rate.

5.2.4.2 Lift-off

Lift-off is very important for patterning thin films, usually catalytic metals such as

platinum (Pt), gold (Au), etc, that are frequently used in chemical sensors but not easily patterned directly. In the process sequence, a metallic thin film is deposited on the patterned positive photoresist. Next a solvent dissolves the photoresist and lifts off the metal, leaving only the metal that was directly deposited left on the substrate.

Standard photoresist processing is the easiest method for lift-off, because it involves only one mask and used completely standard photolithography. However, while using this method, there is no way that a discontinuity or gap in the metal deposition, which is very important for solvent to get at the uncoated photoresist wall, can be formed.

Usually a presoak process is chosen to develop an undercut on a positive photoresist prior to metal deposition. This step could be accomplished by soaking the resist-coated wafer into chlorobenzene solution for 5 minutes after its exposure in the mask aligner. The photoresist top layer would swell due to diffusion of chlorobenzene. A gel is formed to the depth of the diffusion, which develops much more slowly than the bulk of the resist. So undercut in photoresist structures is formed and the desired profile is produced. Although this process provides a discontinuity or gap in the metal deposition, it is proved in the long run to have small process latitude and to be very expensive to implement. The poor process latitude appears to be a function of the sensitivity of the resist structure to a wide variety of variables. These variables include exposure energies, developer concentrations, temperatures, and time and especially trace impurities in the chlorobenzene. A tiny variation in any of these variables tended to be catastrophic.

In our work, an advanced photoresist LOR was employed in the lift-off process. MicroChem's line of LOR lift-off resists are based on the PMGI (polydimethylglutarimide) platform and are well suited for a variety of critical and non-critical level lift-off processes. Used in combination with conventional positive resists, LORs are available in a wide range of film thicknesses and undercut rates.

LORs address the process requirements for GMR and MR heads, wireless devices, opto-electronics, such as semiconductor lasers and detectors, MEMS and many other microelectronic applications requiring easy process tuning, high yields and superb deposition linewidth control.

Advantages of LOR photoresist:

- Submicron linewidth control
- Finely tuned undercuts
- Does not intermix with imaging resists (no scum)
- Excellent adhesion to Si, NiFe, GaAs, InP and many other III-V and II-VI materials
- Simple bi-layer processing without extra flood exposure, develop, amine treatment or toxic chemical soak steps
- Formulations for deposition processes up to 5 μm

The LOR line of resists includes two series:

- LOR A series have relatively low dissolution rates and offer superb undercut control. They are ideally suited for thin-film processes with 0.26N metal-ion-free developers, such as Shipley's CD-26 and TOK's NMD-3.
- LOR B series have relatively high dissolution rates, which makes them ideally suited for thick-film processes. They are optimized for metal-ion-bearing developers, such as AZ 400K 1:4, as well as low normality metal-ion-free developers, such as Shipley's MF-319.

Figure 5.4 is a schematic representation of lift-off process using an LOR photoresist.

The details are described as follows.

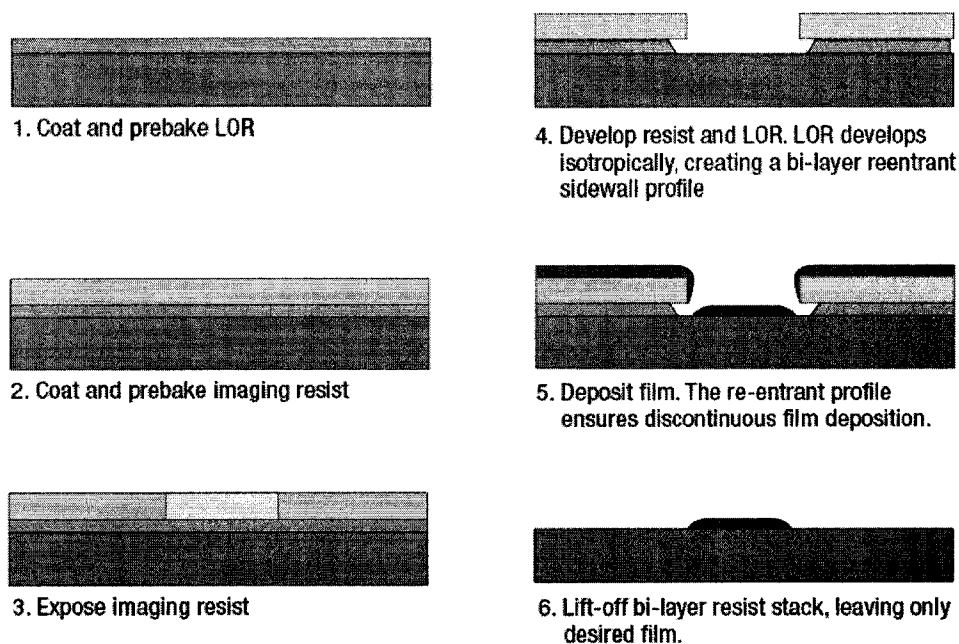


Figure 5.4 LOR lift-off process

1. Coat and prebake LOR. LOR 7B was employed in our research. Prebake temperature is the parameter with the greatest influence on undercut rate, although prebake time, exposure dose of the imaging resist, choice of developer, and develop time are also influential. For small feature sizes such as 2 μm , the prebake temperature is suggested at 190 $^{\circ}\text{C}$, and the prebake time should be no more than 1 minute, otherwise LOR 7B would be very hard to develop even though it has undergone the exposure process.
2. Coat and prebake imaging resist. Usually this process is similar to the softbake process in photolithography.
3. Expose imaging photoresist.
4. Develop resist and LOR. LOR develops isotropically, creating a bi-layer reentrant sidewall profile.
5. Deposit film. The re-entrant profile ensures discontinuous film deposition.
6. Lift-off bi-layer photoresist stack, only leaving desired film. MicroChem's EBR

PG effectively removes both edge beads and whiskers, and is designed specifically for LOR resist.

5.3 Design and Microfabrication of SiO₂ Cantilever

5.3.1 SiO₂ Microcantilever Introduction

Most of microcantilevers, which served as physical, chemical, and biological sensors, were made of silicon. Due to the relatively large Young's modulus of silicon material (169 GPa), the bending response of the silicon microcantilever is too weak to be measured when the surface stress change is rather small. In the previous works [1], we developed a silicon dioxide (SiO₂) cantilever sensor for better sensitivity [34], [68], [74], [75] by taking advantage of the smaller Young's modulus of SiO₂ (76.5-97.2 GPa) in comparison with a silicon or silicon nitride microcantilever. We used a plasma anisotropic dry etching process to release the SiO₂ microcantilever beams. To completely release the cantilever beam, the anisotropic dry etching must go through the 500- μ m-thick sacrificial silicon from the backside of the wafer. Common photoresist can not be used as an etching mask. The etching mask material must be carefully selected. In addition, SiO₂ microcantilever beams are fragile, such that they can be easily damaged by impact with other objects during handling. It would be better to build in some protective measures in the microcantilever structure design.

In this work, we developed an SiO₂ cantilever sensor fabrication process with a very high etching rate by using isotropic dry etching to completely release the cantilever beam from both sides of the substrate. For a better understanding of the isotropic etching process, the effects of reaction chamber pressure, ICP plasma source power, substrate power, and SF₆ flow rate on the etch rate, undercut rate, and isotropic ratio have been investigated.

5.3.2 SiO₂ Microcantilever Design

A 3-D schematic diagram of the SiO₂ microcantilever structure as designed is shown in figure 5.5. The device consists of two adjacent SiO₂ cantilever beams, connecting wings on both sides, and three guard arms. The dimensions of the designed SiO₂ microcantilever beams are 250 μm in length, 100 μm in width, and 1 μm in thickness. The connecting wings were connected with the adjoining cantilever bodies after the beams were released, so that all the cantilevers were retained on the substrate for further processing. The guard arm was designed to protect the microcantilever beam from damage by impact during separation and handling procedures.

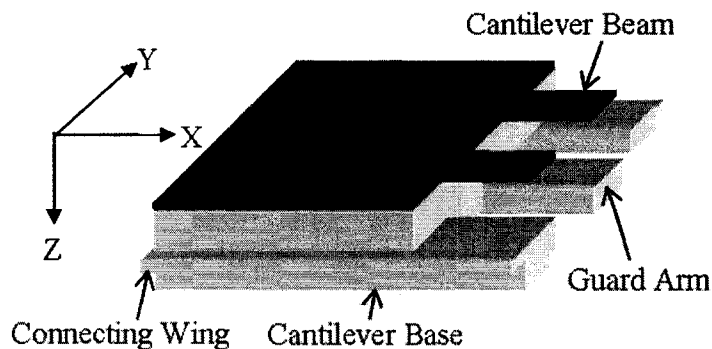


Figure 5.5 Schematic diagram of the novel SiO₂ microcantilever design

5.3.3 SiO₂ Microcantilever Fabrication

The starting material was a commercially available [Silicon Inc.] double side polished four-inch (100-mm), <100> silicon wafer 500 μm thick, and with a 1 μm thick SiO₂ layer on both surfaces. To achieve the microcantilever structure described previously, four masks were designed and applied. Among these, Mask 2 was specifically designed for cantilever beam release by isotropic plasma dry etching, which was described in detail in chapter 4, combined with the anisotropic etching process as illustrated in figure 5.6. The design of Mask 1 and Mask 2 was also

explained in Chapter 4. Figure 5.7 illustrates the main steps of the fabrication process.

The fabrication process is described as follows:

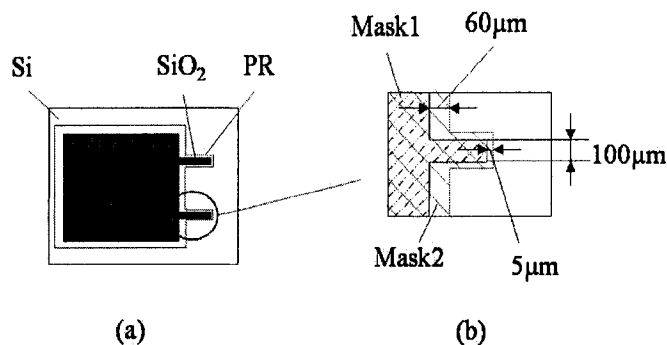


Figure 5.6 Pattern of the PR (photoresist) as a mask for cantilever beam release.

A. Pattern the SiO₂ cantilever beam

Shipley 1813 positive tone photoresist was spun on one surface of a silicon wafer. The spin speed was 3000 rpm for 50 seconds, and the thickness of photoresist layer was about 2 µm. A microcantilever beam pattern was transferred with Mask 1 to the photoresist layer on the front side of the wafer by a standard photolithography process and then the SiO₂ cantilever shapes were defined by wet etching with Buffered Oxide Etchant (BOE HF:NH₄F=1:6 in volume). In the mean time, the entire SiO₂ layer on the back side was etched off. The photoresist was then cleaned by acetone and DI water rinses (figure 5.7(a)).

B. Wafer backside etching 1: pattern cantilever base with guard arm

A 3 µm thick 1813 photoresist layer was spun on the backside of the wafer and then patterned with a photolithography process to form the base of the cantilever sensor. The photoresist pattern served as a mask for ICP plasma etching to create the guard arm in the next fabrication step. The wafer was etched to about 70 µm deep by the ICP anisotropic etching process (figure 5.7(b)). The etching depth of about 70 µm determined the thickness of the connecting arm. This etched area will be

completely opened through the wafer after releasing the cantilever beam.

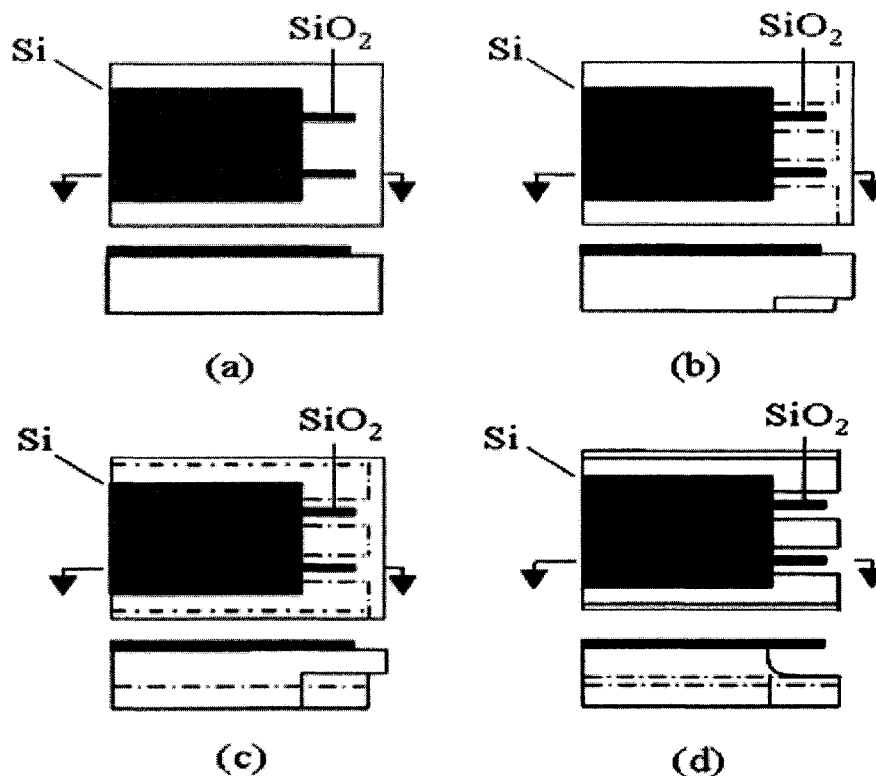


Figure 5.7 Process flow for SiO_2 microcantilever fabrication. (a) Pattern SiO_2 microcantilever beam by BOE etching (b) Pattern the guide arm by ICP etching (c) Pattern the connecting wing by ICP etching (d) Microcantilever beam released by ICP isotropic etching.

C. Wafer backside etching 2: pattern cantilever connecting wing and guard arm

A $3\ \mu\text{m}$ layer of photoresist 1813 was spun on the backside of the wafer again and then plasma anisotropic etching applied to etch about $260\ \mu\text{m}$ deep. This etching step is also applied to etch the connecting wings, guard arms, and open window from the backside of the substrate (figure 5.7(c)).

D. Cantilever beam release

A new process, which involves two steps, was developed to release the SiO_2 cantilever beam. The cantilever beam was first patterned by anisotropic dry etching and followed by the isotropic plasma dry etching to completely release the

cantilever beam. In the first step, anisotropic etching was applied to open a window and to ensure that the fluorine radicals can react efficiently with the silicon underneath the SiO₂ beam during isotropic plasma etching. Then, the isotropic plasma etching was applied to release the SiO₂ beam from the bulk silicon substrate.

A 3 μm thick film of photoresist 1813 was spun on the front side of the wafer and then the front side of the wafer was patterned with Mask 2 (figure 5.6). The photoresist pattern served as an etching mask for the ICP etching process to release the microcantilever beam from the bulk silicon. The cantilever beam was released by two plasma dry etching steps: 90-μm deep anisotropic etching and then isotropic etching until all microcantilever beams were released (figure 5.7(d)). The processing time for releasing the cantilever was 20 minutes. The optimal recipe for isotropic etching in this step was chosen by the following investigation and discussions.

Figure 5.8 shows the scanning electron microscopy (SEM) images of one cantilever. Figure 5.9 shows a 12 beam array on one microcantilever body. The configuration of the array of several devices is shown in figure 5.10. The connecting wing between two adjacent microcantilever bodies should be about 50-70 μm thick, so that the thickness is not only sufficient to connect them together, but also easily broken just by applying a little force. The cantilevers can easily be coated with a sensing polymer or films for different chemical or biological sensing applications.

Another advantage of this process is that it is easy for us to handle the problem associated with the photoresist mask, which occurred in our previous experiment. During anisotropic dry etching to go through an entire wafer with ICP, the photoresist mask was damaged or etched off because the ions bombard the surface of the photoresist. The fabrication process we developed calls for dividing the release process

into three dry etching steps. Meanwhile, the release time is greatly reduced at the higher isotropic etching rate ($9.1\mu\text{m}/\text{min}$). Therefore, the $3\mu\text{m}$ thick photoresist 1813 can be an appropriate masking layer for releasing the cantilever beam.

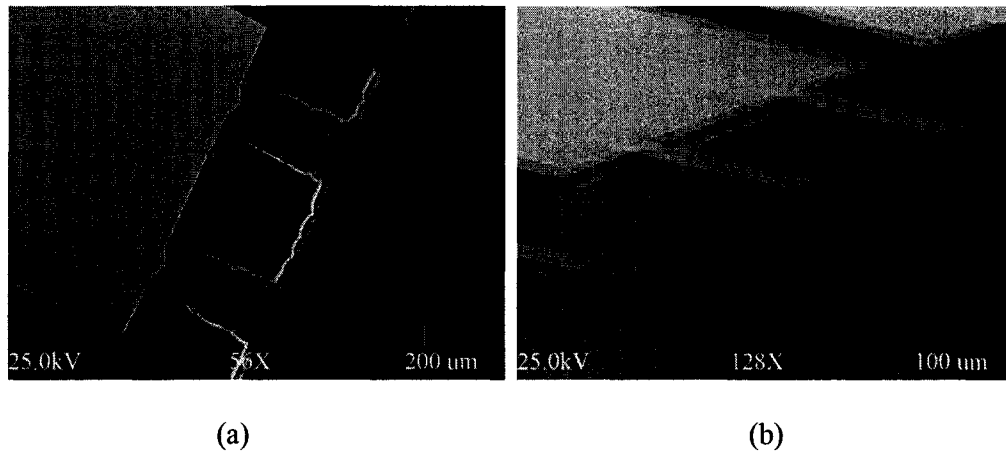


Figure 5.8 SEM image of rectangular cantilever beam.

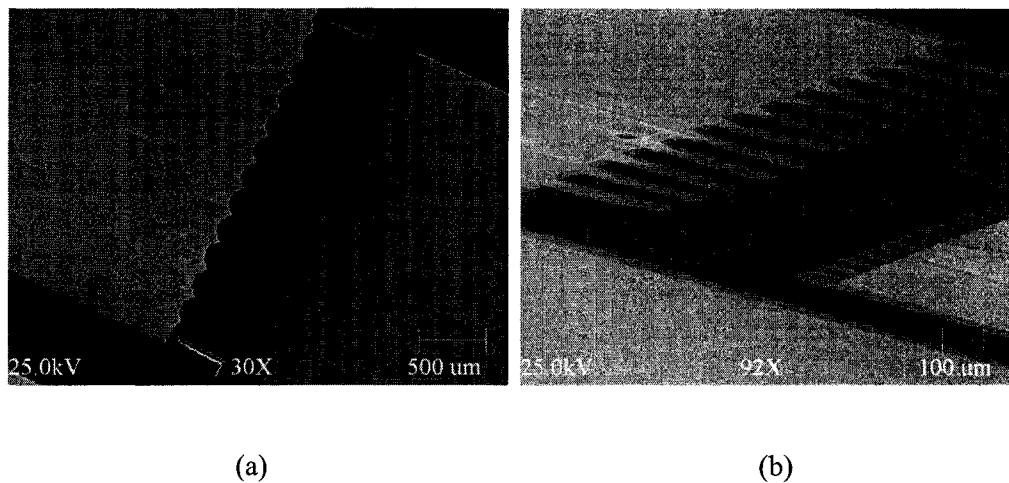


Figure 5.9 Rectangular microcantilever array

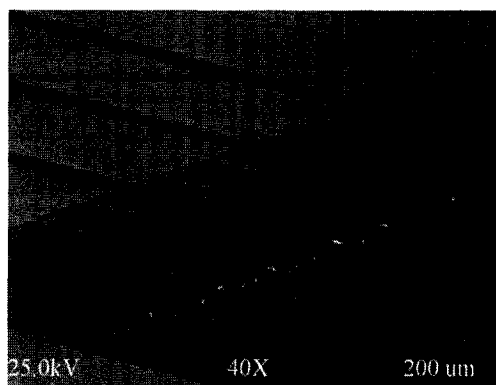


Figure 5.10 SEM image of SiO_2 microcantilevers.

CHAPTER SIX

MEASUREMENT OF SiO₂ MICROCANTILEVER AS MOISTURE

SENSORS

A comparison experiment between Si and SiO₂ microcantilevers was done by exposing both to the same concentration of aminoethanethiol solution. The experimental results also fit perfectly with the simulation results reported in Section 3.1. The moisture sensor based on the polymer surface modified SiO₂ cantilever beam showed a good response to one percent relative humidity. Moreover, Al₂O₃ coated SiO₂ microcantilevers demonstrated the capability of detecting moisture concentration level down to 30 ppm.

6.1 Measurement Equipment

The optical beam deflection method, which is commonly used for the microcantilever sensor, was reported to have excellent readout efficiency and sensitivity. The optical beam deflection measurement system is shown in figure 6.1. The experiments were performed in a flow-through liquid cell that held the microcantilever, whose surface was modified with a certain sensing material. A flow controller is able to control the flow rate of the analyte solution from the syringe or injection pump. Fast replacement of the liquid in contact with the cantilever can be ensured due to the very small volume (0.3ml) of the liquid cell. The deflection of the cantilever beam was detected with an AFM (Atomic Force Microscopy) apparatus,

where a laser beam is focusing at the free end of the cantilever beam. The corresponding displacement of the reflecting laser beam was detected by a position-sensitive photodetector. This particular optical detection scheme has already been described in Section 2.3.1.

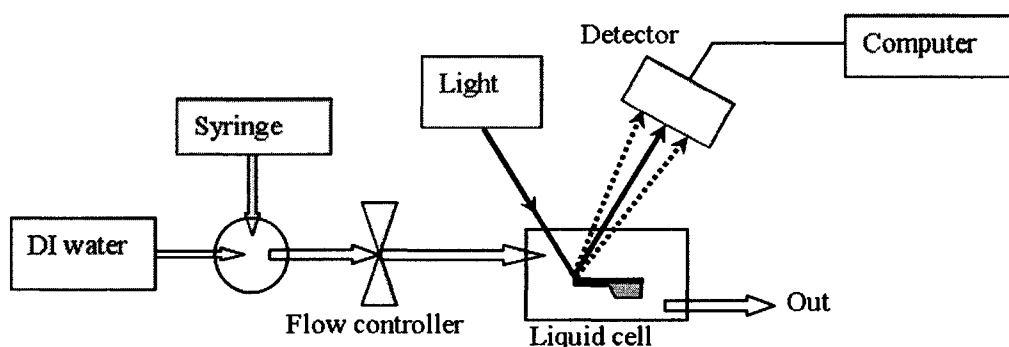


Figure 6.1 Measurement setup based on optical methodology.

6.2 Control Experiment

According to the simulation results discussed in Section 3.1.2, it is expected that an SiO_2 cantilever has the potential to give a 2.37 times larger deflection amplitude than a silicon cantilever as a chemical or biological sensors. To compare their deflections, an SiO_2 cantilever and a silicon cantilever of the same size were deposited with a 20nm thick layer of gold on one side for further measurements, because thiol compounds, such as aminoethanethiol solution, form a monolayer on the gold surface that would deflect the microcantilever on whose surface a gold layer has been deposited [34]. Figure 6.2 shows that the deflection of the SiO_2 microcantilever upon exposure to 10^{-5} M of aminoethanethiol solution, was approximately 220 nm, while that for the silicon microcantilever was approximately 90 nm. Therefore, the bending value of the SiO_2 microcantilever was 2.44 times larger than that of the silicon microcantilever under the same experimental surface-stress situation. This experimental result matched perfectly

with our above simulation result, in which the bending ratio was 2.37 times.

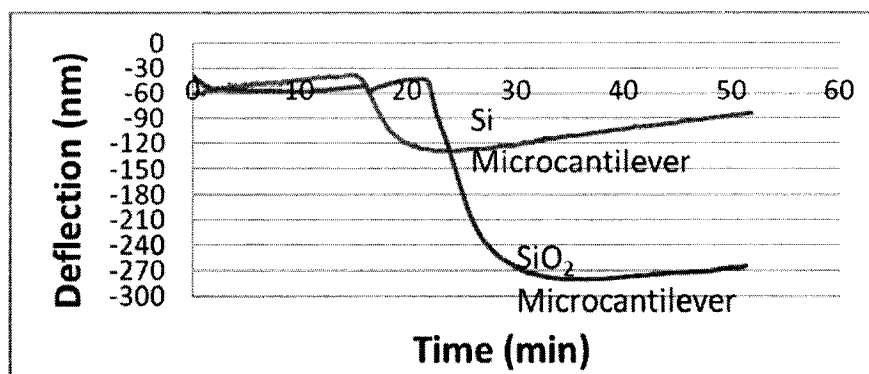


Figure 6.2 The bending response of the SiO₂ and Si microcantilevers upon exposure to a 10⁻⁵ M solution of aminoethanethiol in ethanol.

6.3 Moisture Measurement

6.3.1 Ethyl Acetate Modified SiO₂ Microcantilever

Moisture sensors have been widely used for measurement and control of humidity in an industrial or household environment. The relative humidity (RH), which is the ratio of actual vapor pressure of water to the saturated vapor pressure at a particular temperature, is commonly used to measure moisture. The sensor materials used are either polymeric or ceramic.

First of all, to measure the moisture, the experiments were performed in a flow-through gas cell that held the microcantilever which was coated by a layer of ethyl acetate as the sensing material. Before testing, N₂ was flowed overnight to dry the system chamber to a RH (Relative Humidity) << 1.0%. When the baseline was reached, a tiny amount of water ($\Delta RH=1.0$) was injected into the chamber. A humidity meter [HM34, The Vaisala Corporation] was online to monitor the relative humidity. As the moisture returned to the initial condition, the microcantilever relaxed from bending and moved back to its original position (figure 6.3).

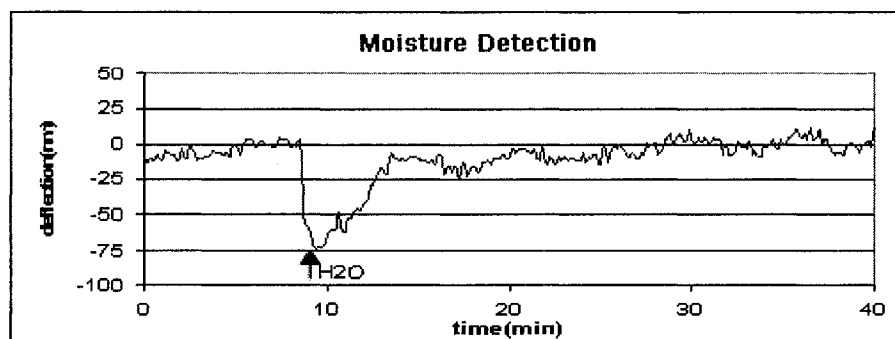


Figure 6.3 The response of cantilever beam coated with a layer of ethyl acetate to relative humidity of 1%.

Figure 6.3 shows that the new moisture sensor responds immediately with about a 75nm deflection when the humidity increases to 1% and releases bending spontaneously with a decrease in the humidity. The excellent real time monitoring property gives the device a promising application in environments requiring high sensitivity.

6.3.2 Aluminum Oxide Modified SiO₂ Microcantilever

6.3.2.1 Experiment Design

Metal oxide semiconductor sensors are the most promising devices among the solid-state chemical sensors, because they have many advantages, such as small dimensions, low cost, low power consumption, on-line operation, and high compatibility with microelectronic processing. They could be used in environmental monitoring, automotive applications, industry production control, and sensor networks. Hence, the metal oxide gas-sensing materials have been widely investigated for a long time. The sensing mechanism of metal oxide gas-sensing materials is based on the reaction between the adsorbed oxygen on the surface of the materials and the gas molecules to be detected. The state and the amount of oxygen on the surface of materials were strongly dependent on the microstructure of the materials, namely, specific area, particle size, as well as the film thickness of the sensing material.

Alcohol vapor is one of the most popular industrial concerned gases, which always exists together with water vapor. Recently, the interference of ethanol to moisture detecting attracts more and more attention because of the highly accurate and dedicated humidity-sensing requirement. Thus, the emergence of humidity sensors with no alcohol influence becomes a driving force for pursuing related research.

Our goal is to achieve an acceptable industrial moisture sensor for serving in the natural gas environment with negligible drift due to the existence of alcohol. Al_2O_3 coated SiO_2 microcantilevers have been applied as our experimental platform. As noted typically there are two main groups for the formation of Al_2O_3 : Al oxidation and direct deposition. In this measurement, the Al_2O_3 was attained by oxidizing the Al film for process simplicity and low cost. A 100nm thick Al thin film was deposited on the surface of the SiO_2 cantilevers by thermal evaporation. Next, those cantilevers were divided into two groups, which have been oxidized by using 100 °C pure O_2 thermal oxidation and room temperature plasma oxidation, respectively.

The experiment procedures were designed as follows:

1. Pure dry N_2 environment, flow rate varies between 70-80ml/min, waiting for baseline to be reached.
2. Inject N_2 saturated with moisture at a certain flow rate to provide environment with a certain moisture concentration, lasting for 2min.
3. Waiting for recovery, then inject saturated N_2 with $\text{C}_2\text{H}_5\text{OH}$ and provide an alcohol environment with same concentration as step 2;
4. Waiting for recovery, repeat step 2;
5. Waiting for recovery, inject mixture of H_2O and $\text{C}_2\text{H}_5\text{OH}$ with each concentration the same as above.

In order to determine the performance of the Al_2O_3 coated cantilevers in certain environment condition, we run experiments at various temperature and moisture concentrations. From the data list below, experiments are operated at temperatures of 20 °C, 30 °C, 40 °C and 50 °C with moisture ranging from 30ppm to 200ppm.

The sensing gas environment with certain moisture concentration, is created by the mixing of pure dry N_2 and saturated N_2 under its corresponding ratio as calculated from thermal equations, with the approximation of applying the air constant to the N_2 system and ideal gas assumption. The heater and thermometer, as well as a water bath provide the temperature control for the flow system. The gas flow loop is submerged in the water bath in order to attain the target temperature. Saturated gas is stored in a syringe and is kept in a heated cabinet. When the base line is reached, the syringe pumps saturated gas into the flow system at a certain flow rate of the mixture and pure dry and saturated gas forming an environment with certain moisture, or alcohol, or moisture mixed with alcohol, concentration.

6.3.2.2 Results and Discussion

Figure 6.4 compares the bending response of the modified microcantilever to various moisture levels in nitrogen at a 100 mL/min flow rate. The moist gas was switch in at the marked time. The microcantilevers underwent upward bending and the maximum deflection amplitude depended on the concentration of moisture. After approximately 3 min, the dry nitrogen was switched back through the fluid cell, and the microcantilever bent downward and back to their original positions. Figure 6.4 insert shows the reproducible response of the microcantilever to a 30 ppm level of moisture.

Figure 6.5 showed the microcantilever maximum deflection amplitude vs. the vapor concentration. The maximum deflection amplitudes of the microcantilevers

were proportional to the concentrations of moisture. The microcantilever deflection increased as the concentration of moisture increased. The lowest detectable concentration was obtained at 10 ppm, which was significantly improved over the

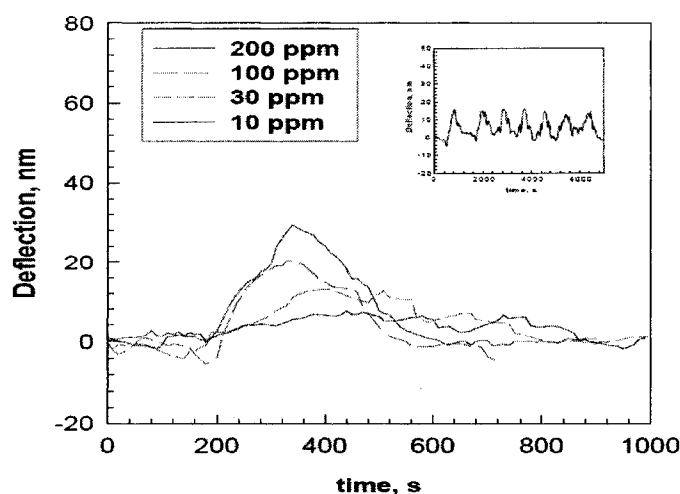


Figure 6.4 Deflection of Al_2O_3 modified microcantilevers versus time at various moisture level in nitrogen at 30 °C. The gas flow rate was 100 mL/min. Insert: Deflection of the microcantilevers versus time after repetitive exposure to 30 ppm moisture in nitrogen.

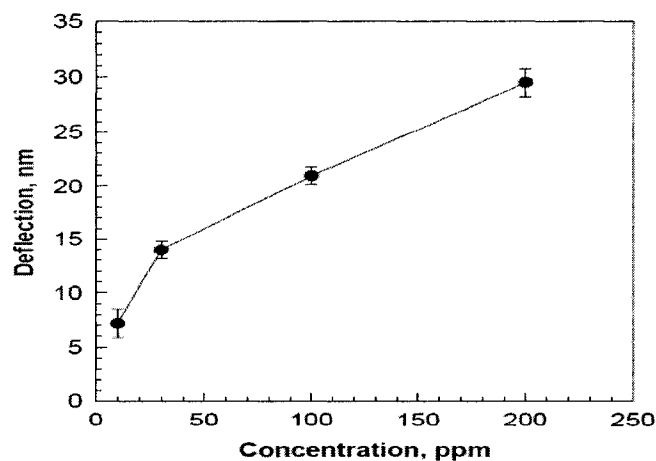


Figure 6.5 Deflection amplitude of Al_2O_3 modified microcantilevers versus the concentration of moisture in nitrogen.

SiO₂ and Si₃N₄ modified microcantilevers with detection limits at approximately 200 ppm [21], [76].

The larger microcantilever deflection suggests a larger surface stress change on the microcantilever surface at higher moisture concentrations. For a 32nm maximum deflection corresponding to 200 ppm of moisture, the surface stress change was 0.083 N/m.

Figure 6.6 shows the microcantilever deflection vs. time at different temperatures. The results showed that the microcantilever deflection amplitude increased at high temperatures, which is a typical phenomenon for metal oxide based sensors. Except for the bending amplitudes, the microcantilever response and recovery profiles were similar under different temperatures. These results suggested that temperature calibration is needed for accurate moisture measurement at different temperatures.

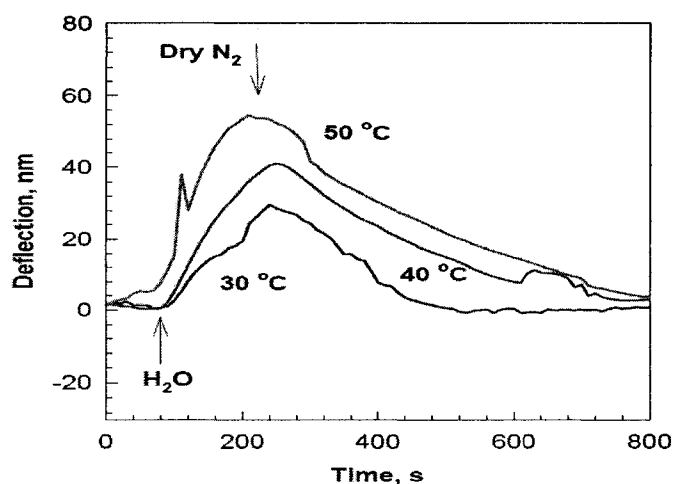


Figure 6.6 Deflection of Al₂O₃ modified microcantilevers versus time upon exposure to 200 ppm of moisture in nitrogen at different temperatures. The flow rate was 100 mL/min.

Selectivity over alcohol

The effect of alcohols is the major concern of many moisture meters for low level moisture detection since the alcohols generally interfere with moisture detection and

cause error. Alcohols cause significant error to IR devices and have relatively less effect on other devices [77], [78]. Our initial test showed that the SiO_2 and Si_3N_4 modified microcantilevers were largely affected by alcohols (figure not shown), which disqualify them for accurate moisture detection without calibration when alcohols exist in the environment.

The potential interference of alcohols on the Al_2O_3 modified microcantilevers was evaluated in this study as shown in figure 6.7. In these experiments, the microcantilever deflected 23.5nm upon exposure to 100 ppm moisture; no response to 100 ppm alcohol; deflected again 24nm upon exposure to 100 ppm moisture; and deflected 25nm upon exposure to 100 ppm moisture + 100 ppm alcohol. These results showed that a) the microcantilevers did not deflect upon exposure to alcohol; b) The microcantilevers response to moisture was not interfered with by alcohol after exposure to alcohol; c) The microcantilever responses to moisture were the same with and without alcohol in the environment.

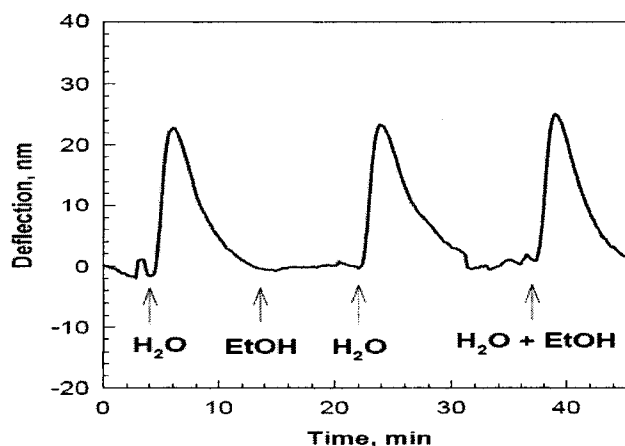


Figure 6.7 Deflection of Al_2O_3 modified microcantilevers versus time upon exposure to 100 ppm of moisture, 100 ppm of alcohol, 100 ppm of moisture, and 100 ppm moisture + 100 ppm of alcohol in nitrogen at 40 °C, respectively. The flow rate was 100 mL/min.

6.4 Conclusion

An experiment for comparing Si and SiO₂ microcantilevers was carried out, and its results confirmed that the SiO₂ cantilever can achieve a much higher sensitivity than the Si cantilever. Attributed to have high sensitivity, the SiO₂ cantilever was employed to detect low-level moisture. The feasibility of a technology for low-level moisture detection depends on many factors: sensitivity, response time, accuracy, long term stability, temperature coefficient, and susceptibility to contaminants, such as alcohol, and cost. Our results showed that Al₂O₃ coated microcantilevers are excellent sensors for low level moisture detection and may be used for moisture monitoring in a low level moisture environment, such as in pipelines, chambers to store moisture sensitive products, and high voltage engineering and accelerator systems. The characteristics include short response time (2 min), long term stability, and especially not affected by alcohol, make the cantilever approach very competitive. The detection limit may be further improved by fine tuning of the coatings.

CHAPTER SEVEN

DESIGN, FABRICATION AND TESTING OF PIEZOELECTRIC

MICROCANTILEVER AS A MOISTURE SENSOR

Although an optical readout system can meet the commercial requirement for measuring moisture levels ranging from 1ppm to 100ppm, for industrial applications, it still has some disadvantages, such as its alignment system is expensive and involves great precision and it is not compatible with IC technology and, consequently, is not portable. In chapter three, it was confirmed that the Al_2O_3 modified microcantilever, operating in dynamic mode can satisfy the requirement of low level moisture detection and can be compatible with IC circuitry. To make this device compatible with IC technology and improve its performance as well, the piezoelectric microcantilever is chosen as the platform for moisture sensing. A piezoelectric microcantilever vibrates at its resonant frequency upon applying an appropriate AC voltage and provides an electrical signal at the output via piezoelectric coupling, which can be fed back through a phase shift loop to relocate the changed resonant frequency caused by a change in mass. In this chapter, design and fabrication of the piezoelectric SiO_2 microcantilever are presented as well as the preliminary results of an investigation of its application as a moisture sensor.

7.1 Piezoelectric Zinc Oxide

7.1.1 Theory of Piezoelectricity

The direct piezoelectric effect refers to the generation of an electric polarization due to a mechanical stress. Conversely, the indirect piezoelectric effect refers to the generation of a strain in a material due to the application of an electric field. A simplified model of piezoelectricity involves the concept of anions (-) and cations (+) moving in opposite directions under the influence of an electric field or mechanical force. The forces generated by this motion cause lattice deformations for ionic crystals lacking a center of symmetry. Figure 7.1 shows what happens when a piezoelectric crystal is deformed. As a mechanical deformation (stress) is applied to the crystal, electric dipoles are generated due to the shifting of anions and cations and a potential difference develops. It should be noted that the potential difference in piezoelectric materials is a function of the changing stress; therefore, piezoelectric materials are typically used in dynamic situations.

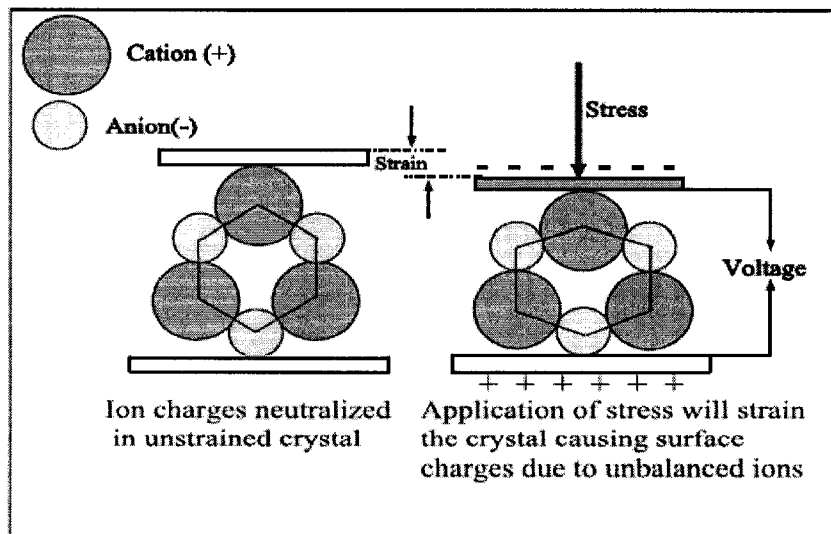


Figure 7.1 Piezoelectricity in an ionic crystal

7.1.2 Piezoelectricity of ZnO

ZnO is a II–IV semiconductor with a wide direct bandgap of 3.2 eV at room temperature and 3.44 eV at 4 °K, and a wurtzite structure [79]. Thin films of this oxide have many remarkable characteristics and are recently attracting great attentions [80]–[86]. As was mentioned above, one of the defining characteristics of a piezoelectric material is the lack of a center of symmetry in the unit cell. Figure 7.2 shows the crystal structure of zinc oxide. ZnO forms a hexagonal wurtzite structure with 6mm symmetry. It possesses the lack of center symmetry required for piezoelectric materials. The coupling coefficient for ZnO is also relatively high which makes ZnO an excellent material to use in a wide variety of piezoelectric applications.

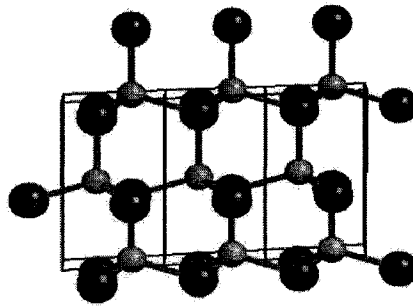


Figure 7.2 The Hexagonal wurtzite crystal Structure of ZnO. The large red atoms are zinc atoms while the smaller purple atoms are oxygen atoms.

7.1.3 ZnO Thin Film Deposition

Many techniques are being used for the fabrication of ZnO thin films [87]–[93], including chemical vapour deposition, sol–gel, spray-pyrolysis, molecular beam epitaxy, pulsed laser deposition, vacuum arc deposition and magnetron sputtering. Due to its flexibilities in the control of composition and microstructure, magnetron sputtering is widely employed. In our fabrication process, ZnO thin films were produced using reactive sputtering with the magnetron sputtering system in IfM at

Louisiana Tech, which has already been described in section 4.2.3.1.

A Zn target (99.999%) was employed in the sputtering system. After putting the wafer in the working chamber, which was pumped down to 8 mTorr, a mixture of 80% oxygen and 20% argon was introduced. Sputtering deposition was performed with a direct current power of 0.07A and -150V. The negative bias appeared to have certain effects on the film morphology. In comparison with deposition using other voltages, such as -50 V [94], the deposition at -150 V provided a more uniform and denser film composed of particles. ZnO thin film with 500 nm thick was deposited at a 30 nm/min deposition rate.

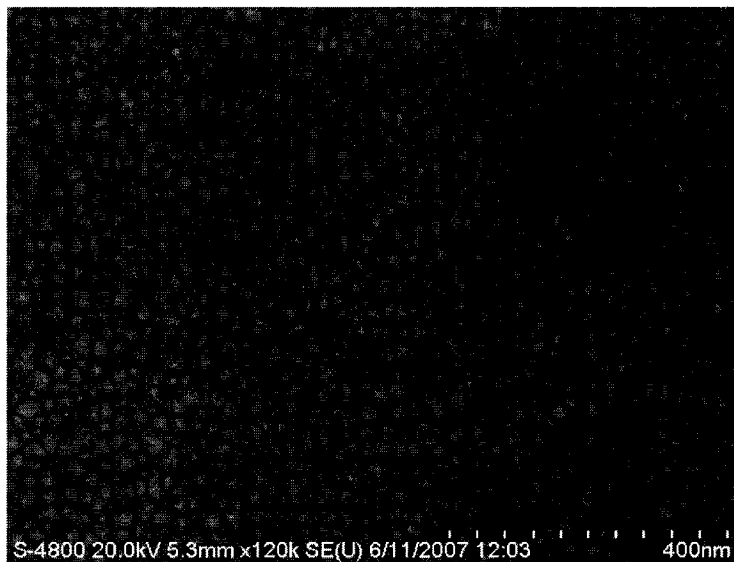


Figure 7.3 The SEM image of ZnO thin film

The surface and fracture cross-section morphologies of the thin films were observed with a field-emission scanning electron microscope (Hitachi, S-4800) in the IfM, and the elemental composition analysis of the thin film was also carried out using EDX (Energy Dispersive X-Ray). Figure 7.3 shows the surface of the ZnO thin films with DC reactive sputtering deposition. It could be seen that a film composed of

regularly shaped particles was formed. The EDX spectrum (figure 7.4) shows that only zinc and oxide exist in the thin film. The elemental composition analysis in table 7.1 shows that the atomic percentage of oxide is 44.36% and that of zinc is 55.64%. The result is close to the expected ratio of 1:1 and is acceptable for our project. As the chamber pressure increased, the generation of Zn species would be inhibited, whereas output of oxygen ions might be increased. Therefore, the deposition rate would be lower, a larger particle size could be formed and the ratio between O and Zn could be enhanced. In the future, more effort will be paid to the investigation of sputtering parameters to optimize ZnO thin film deposition.

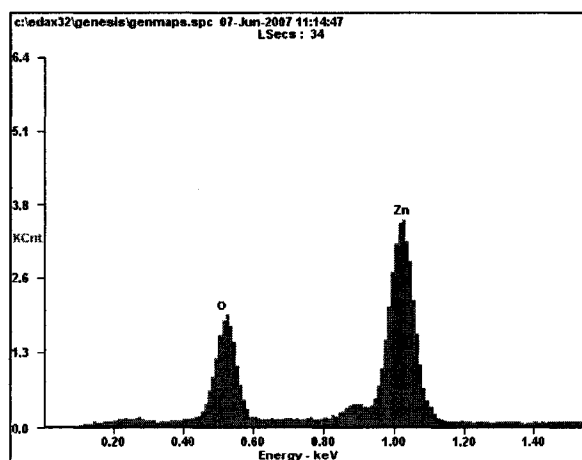


Figure 7.4 The EDX analysis spectrum

Table 7.1 Elemental composition of Zn and O in the thin film

<i>Element</i>	<i>Wt%</i>	<i>At%</i>
<i>OK</i>	16.33	44.36
<i>ZnL</i>	83.67	55.64

7.2 Design and Fabrication of Piezoelectric Microcantilever

7.2.1 Design of Si Piezoelectric Microcantilever

The design considerations for the piezoelectric microcantilever are more

complicated than the design considerations for the SiO₂ microcantilever. Figure 7.5 shows the cross-sectional view of the proposed piezoelectric microcantilever. Silicon was employed as the beam material while ZnO was used as the piezoelectric material and Cr/Pt or Ti/Au was used as the electrode material for this design. This design was based on the SOI wafer, where the end product requires a sandwich of a bottom electrode, ZnO and two top electrodes (one for sensing, the other for actuation) all sitting on top of the nitride cantilever beam. The sandwiched SiO₂ layer and top SiN, SiO₂ layer all serve as an insulating layer while the top Al layer will be modified later for the sensing application.

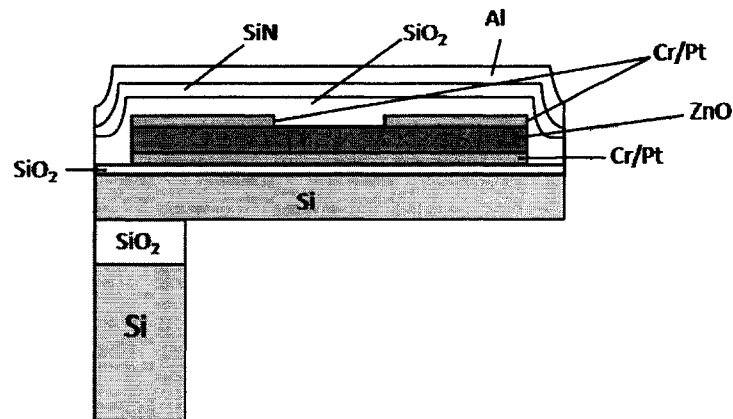


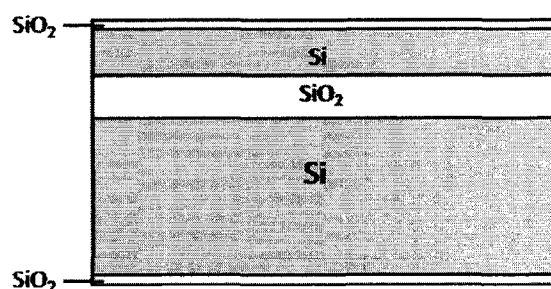
Figure 7.5 The schematic diagram of the piezoelectric microcantilever design.

7.2.2 Fabrication of Si Piezoelectric Microcantilever

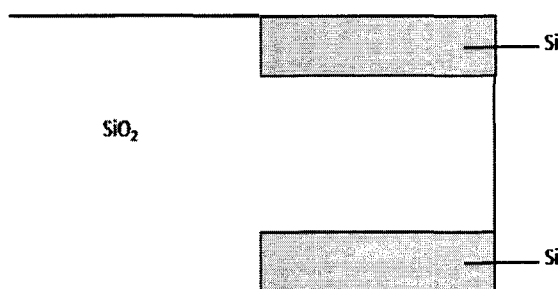
The process for piezoelectric microcantilever fabrication involved the deposition of the silicon dioxide layer, photolithography with front to back side mask alignment, and plasma etching of the front and back side silicon.

The fabrication process started with SOI (silicon on insulator) wafers, which have a silicon device layer, buried oxide as the insulator layer and a substrate silicon layer. First of all, SiO₂ was grown on both sides of the wafer by thermal oxidation for the

purpose of insulating the silicon layer from the following bottom electrode layer. Thereafter, a standard spin coating process was employed to spin photoresist 1813 on the surface of the device layers. The samples were soft-baked in a 110 °C oven for 1 min to remove any solvents from the photoresist and enhance the adhesion to the wafer. The wafers were then removed from the oven and aligned in the mask aligner. The wafers were exposed to UV light for 8-12 seconds, then developed using MF 319 Developer for a few seconds. The hard-bake step was then performed by placing the wafers in a 110 °C oven for 1 min. The SiO₂ was etched using BOE etching (figure 7.6). Finally, the photoresist was removed using acetone and methanol.



(a) Cross section view

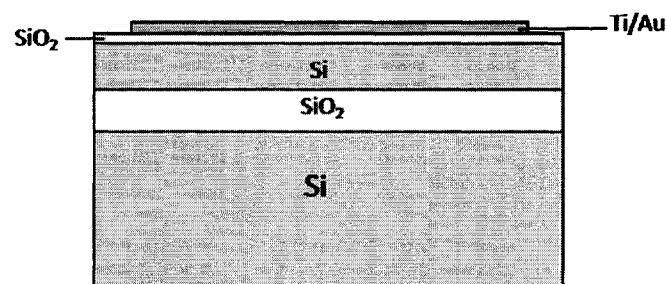


(b) Top view

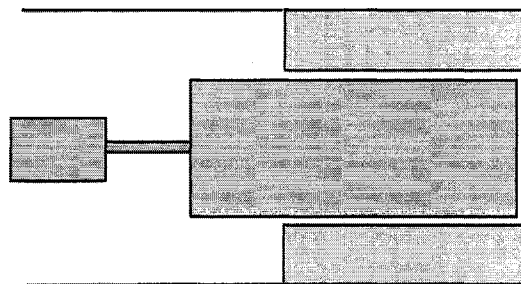
Figure 7.6 The process began with an SOI wafer. Both sides of the wafer have been thermally oxidized and patterned using the BOE process.

The next step in the process was to pattern the platinum or gold layer to form the bottom electrode using the lift-off process. In order to do the lift-off process, LOR 7B

was spin coated on the surface. The samples were then baked in a 170 °C oven for 1 min. Next, the samples were spincoated with photoresist 1813 and baked in a 110 °C oven for 1 min. The wafers were aligned and exposed in the mask aligner by UV light, and then developed using MF 319 Developer for a few seconds. An undercut profile was achieved because photoresist 1813 has a lower developing speed than LOR 7B. The samples were placed in the reaction chamber of the sputtering system to deposit a chromium thickness of 10 nm and a platinum thickness of 150 nm over the entire wafer. Since gold is not very good at adhering to other materials, an adhesion promoting layer, which is chromium with a thickness of 10 nm, was placed between the gold and the underlying substrate. An ultrasonic bath containing EBR solution was used to lift off the unexpected area, where the Cr/Pt sits on top of the photoresist, until the bottom electrode was achieved (figure 7.7).



(a) Cross section view

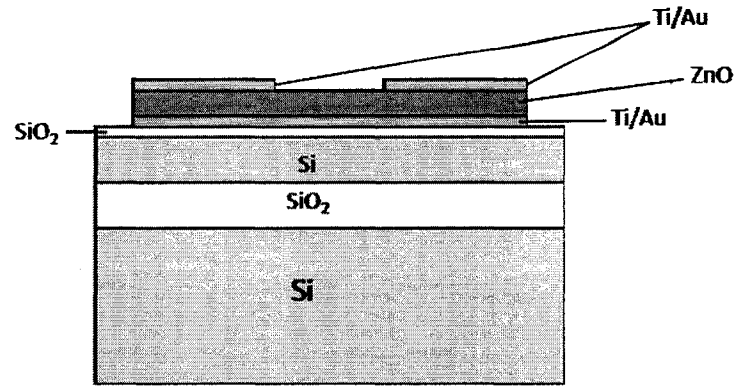


(b) Top view

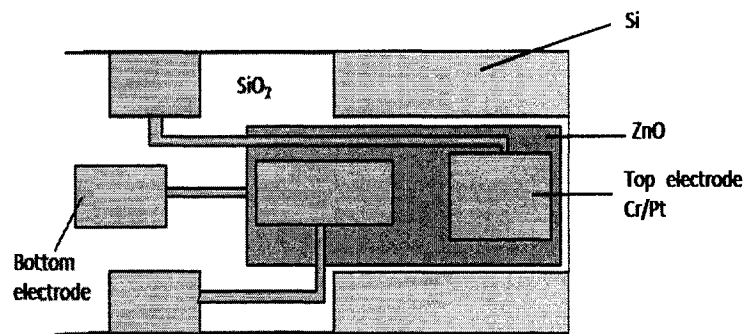
Figure 7.7 Bottom electrode (Cr/Pt layer) was patterned by lift-off process.

After the bottom electrode was patterned and lifted-off, the ZnO was deposited. A 500 nm thick ZnO thin film was deposited using a DC sputtering system. Details of the deposition are described in Section 7.1.3. After the ZnO deposition, an annealing step, which was run in vacuum for 12 hrs at a 400 °C annealing temperature, was performed to give lower stress ZnO and also improve the (002) c-axis orientation. Next, the ZnO layer needed to be patterned and etched using photolithography. This step will be described briefly since it is nearly the same as the photolithography process described previously. Photoresist was applied; the wafers were exposed to UV light through the ZnO mask and then developed in the developer solution. ZnO was etched in an 1:1:30 acetic acid : phosphoric acid: water solution with an etch rate of $\sim 5000 \text{ \AA}/\text{min}$.

After the ZnO was patterned and etched and the photoresist removed, the top electrode layer needed to be deposited and patterned. The lift-off process, which was described in patterning the bottom electrode, was employed to form the top gold electrode. After the lift-off process, the top electrode was formed on the sample's surface (Figure 7.8 ZnO thin film was sputtered on the wafer and patterned to form the piezoelectric layer. Afterwards, Cr/Pt were sputtered on the wafer and patterned by the lift-off process to form the top electrode.). The masks for the bottom and top electrode were designed for a negative tone photolithography process, which was required to complete the lift-off instead of the standard positive tone photolithography, as described previously.



(a) Cross section view

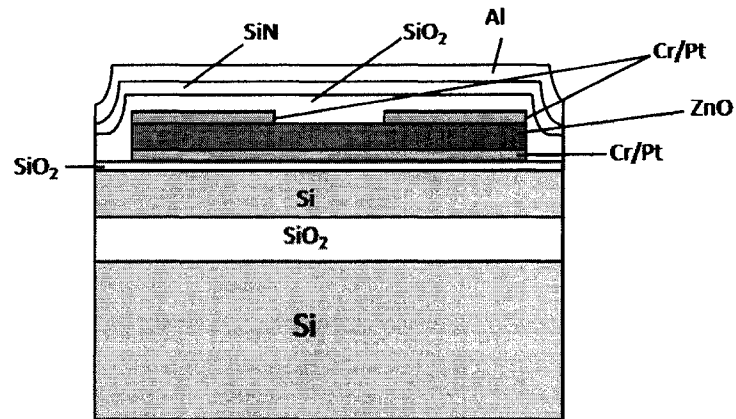


(b) Top view

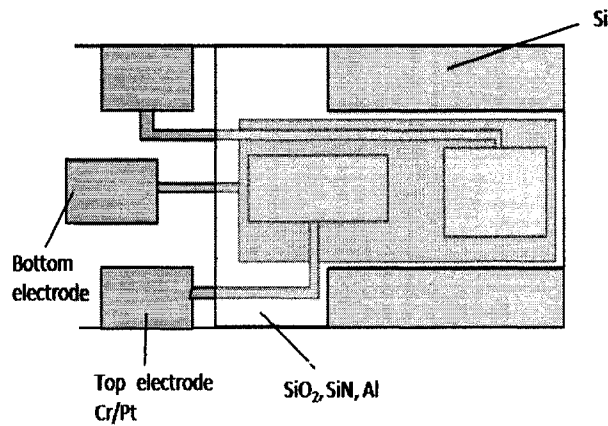
Figure 7.8 ZnO thin film was sputtered on the wafer and patterned to form the piezoelectric layer. Afterwards, Cr/Pt were sputtered on the wafer and patterned by the lift-off process to form the top electrode.

The next step in the process was to deposit and pattern SiO_2 and Si_3N_4 , which would serve as the insulating layer between the sensing alumina layer and the top electrode. The PECVD (plasma enhanced chemical vapor deposition) machine in IfM was used to deposit SiO_2 (150nm) and Si_3N_4 (100nm) on the surface of the samples. After finishing the deposition process, the wafers were patterned by standard photolithography process and then etched in BOE solution for about 3 to 4 mins. Once SiO_2 and Si_3N_4 were patterned, 500nm thick aluminum was deposited and patterned using a lift-off process similar to that used for the bottom and top electrode (Figure 7.9 SiO_2 and SiN were deposited on the wafer and patterned by BOE etching to insulate the top electrode from

the sensing Alumina layer. Next, Al was deposited on the wafer and patterned by the lift-off process.).



(a) Cross section view

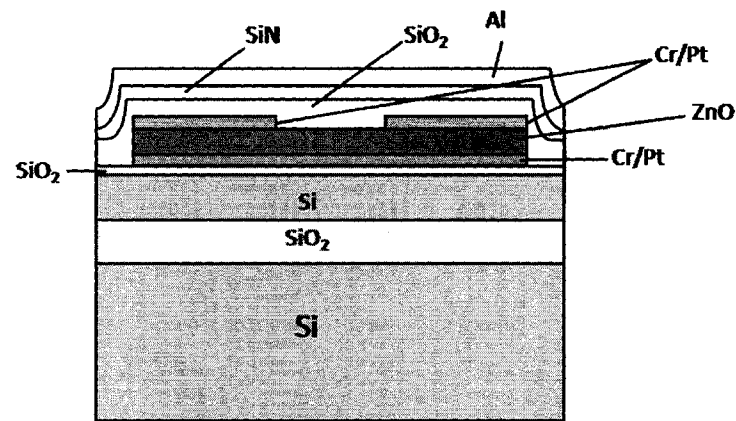


(b) Top view

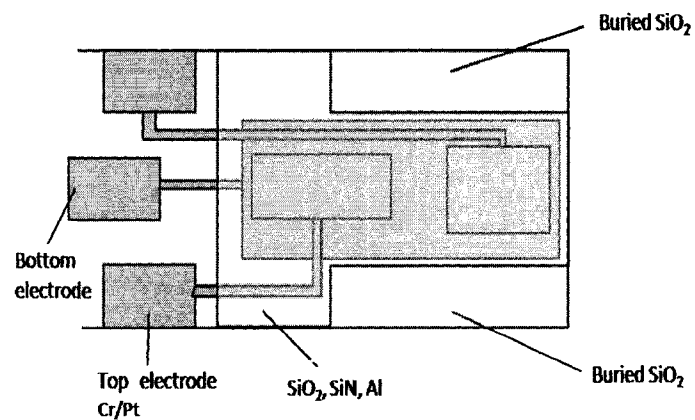
Figure 7.9 SiO₂ and SiN were deposited on the wafer and patterned by BOE etching to insulate the top electrode from the sensing Alumina layer. Next, Al was deposited on the wafer and patterned by the lift-off process.

The following step was used to pattern the silicon cantilever beam (figure 7.10). Since the thickness of the silicon beam layer chosen in our fabrication ranges from 2 to 5 μm, if the beam was defined at the beginning of the fabrication process, the uniformity of the following spin-coating processes would be compromised severely,

such that we made the beam defining step the final process on the front side. A $2\mu\text{m}$ thick 1813 photoresist film was achieved by using a 1500 rpm spin-coating speed and patterned by a standard photolithography process. The silicon cantilever beam was defined with ICP etching using a slow Bosch Big process (SF_6 flow rate 180 sccm, C_4F_8 flow rate 100 sccm, source power 1500 W), which was modified from the Bosch Big process while the photoresist layer served as the mask. The etching rate was estimated at $3\mu\text{m}/\text{min}$.



(a) Cross section view



(b) Top view

Figure 7.10 Top silicon layer was patterned by ICP etching, in which photoresist served as mask, to form microcantilever beam.

Next, the cantilever beam needed to be released from the substrate. Initially, a 150nm thick chromium layer was deposited on the backside of the wafers by e-beam evaporation and patterned in chromium etchant using a photolithography process. According to our previous experimental results, this chromium layer has proven to be a good masking layer for the silicon etching process in the ICP system. The deep reactive ion etching (DRIE) was run on the backside of the wafers while the chromium thin film served as the mask. For the wafers with a 500 μm thick substrate layer, it took approximately 120 mins to etch the silicon substrate until reaching the buried SiO_2 etch stop layer (figure 7.11).

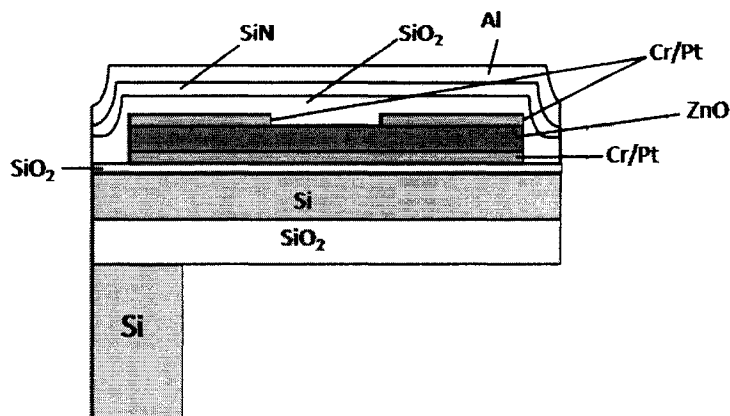


Figure 7.11 Silicon substrate was deeply etched in ICP system by utilizing Cr as a mask until reaching the buried SiO_2 etching stop layer.

The final step in the fabrication process was to remove the etch stop layer under the cantilever beam and completely release the silicon cantilever beam (figure 7.12). This was done by placing the samples in the reactive ion etching (RIE) system. In order to obtain the high etch selectivity of SiO_2 over Si using RIE etching, the parameters in the system were set up as shown in table 7.2.

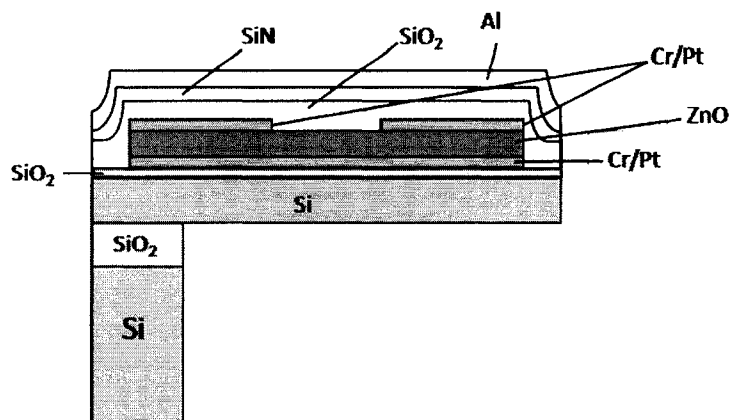


Figure 7.12 The buried SiO₂ layer was etched by RIE using CF₄ and H₂ to eventually release the silicon cantilever beam.

Table 7.2 Parameters in RIE system for buried SiO₂ layer etching

CHF ₃ flow rate (sccm)	O ₂ flow rate (sccm)	Pressure (mTorr)	Power (W)	DC bias (V)	Etch rate (Å/min)
50	7	40	150	440	400

Actually, a silicon dioxide-to-silicon etch rate ratio of 35 to 1 has been achieved by using a CF₄-H₂ etching gas mixture in an RIE system. However, in our RIE system, there is no CF₄ gas available for this experiment. In our experiment, if the proportion of the O₂ in the mixture is increased, the etch rate ratio of SiO₂ to Si also goes up. Considering the etch rate, etch selectivity and the real situation of our RIE system, the parameters shown in table 7.2 were chosen to etch the buried oxide layer. The piezoelectric microcantilevers were then separated individually from the wafer and were ready for the next processing and testing steps.

7.2.2 Fabrication of SiO₂ Piezoelectric Microcantilever

Meanwhile, an SiO₂ piezoelectric microcantilever was also fabricated in our lab by slightly modifying the fabrication process for the Si Piezoelectric Microcantilever. The fabrication process started with a double side polished four-inch (100-mm), <100> 500

μm thick silicon wafer, and a $2\ \mu\text{m}$ thick SiO_2 layer on both surfaces. Since the starting material was SiO_2 , the thermal oxidation step was not necessary in this fabrication. The bottom electrode, ZnO thin film, top electrode, SiO_2 and Si_3N_4 insulator layer, and Al sensing layer were all fabricated by following the same process described above. The cantilever beam defining process was changed to place the samples in BOE solution to pattern the SiO_2 layer. After the bulk silicon was etched away from the backside of the wafers, the SiO_2 cantilever beam was completely released.

7.3 Results

Both SiO_2 and Si piezoelectric microcantilevers were successfully fabricated. This chapter will examine the optical photos, SEM images, and preliminary testing results for moisture sensing as part of this project.

7.3.1 Fabrication Results

The optical photos of the nearly completed SiO_2 microcantilever are shown in figure 7.13 and figure 7.14. Both photos, in which the cantilever beam was not free standing, were taken prior to the backside silicon etch step. The photos do show that all the layers are aligned and there are no shorts existing between the top electrode and the bottom electrode.

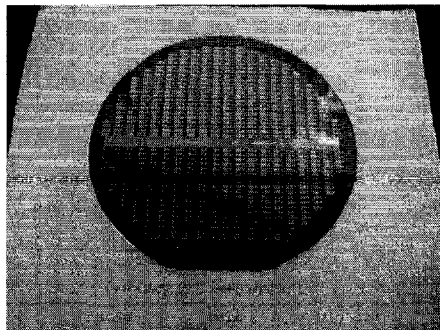


Figure 7.13 Top view of mass-produced SiO_2 piezoelectric microcantilevers taken by Canon digital camera.

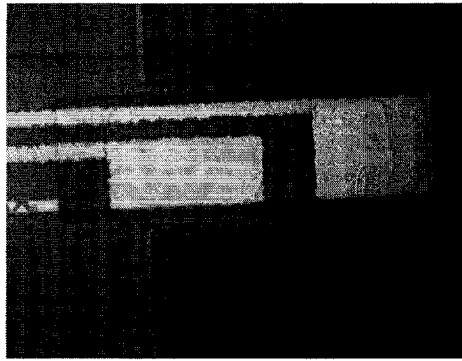


Figure 7.14 Top view of SiO_2 piezoelectric microcantilever beam prior to backside release taken by Sony microscope.

SEM images of the SiO_2 piezoelectric cantilever were also obtained. A top view and a side view of one of the cantilevers are shown in Figure 7.15 (a) and (b). The SEM images demonstrate that the fabricated devices are exactly what we designed and expected.

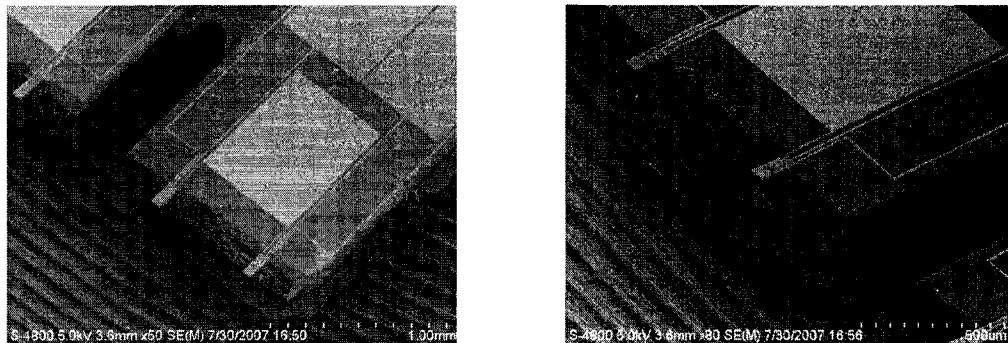


Figure 7.15 SEM images of the fabricated SiO_2 piezoelectric microcantilevers. (a) a top-down view (b) a side view.

7.3.2 Experimental Results and Discussion

After the microcantilevers were fabricated, 500nm thick aluminum was deposited on the back side of the cantilever beam and a commercial triangle microcantilever. Then the aluminum on the back side of both cantilevers was anodized using chemical-electrical method and the cantilevers were then ready to detect moisture. Figure 7.16 shows the experimental setup of the moisture detection system used to

measure the deflection of the cantilevers. The experimental set-up consists of only a tygon pipe and chamber to which a relative humidity (%RH) measuring meter is attached. Initial moisture levels are measured in terms of %RH. The deflection is detected using the optical deflection method of Atomic Force Microscopy.

Both cantilevers coated with anodized alumina, were subjected to the sensitivity tests. The results are shown in table 7.3. Our fabricated cantilever shows that its resonant frequency is about 36 kHz and resonant frequency shift is 1.25 Hz/ppm. It presents a higher natural resonant frequency and better moisture sensitivity compared with the commercial triangle cantilever, whose natural resonant frequency changes range from 0.5 to 1 Hz/ppm. It is expected that our fabricated piezoelectric cantilever operating in resonant mode would have a potential application for moisture sensing, even if it is integrated into an IC board.

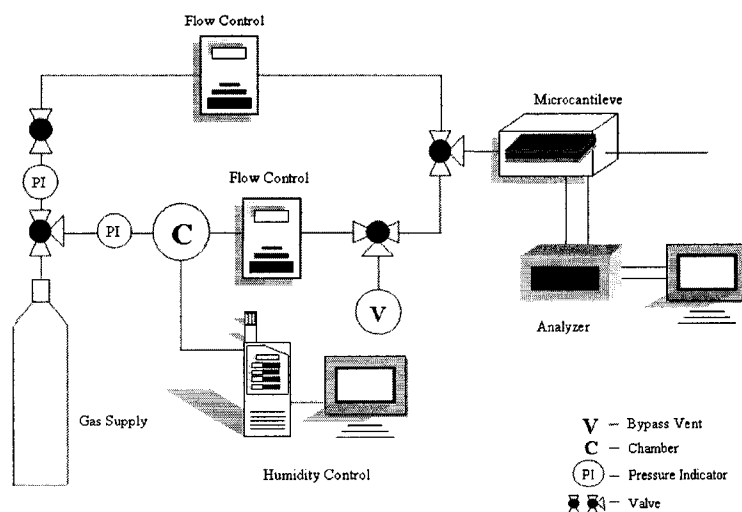




Figure 7.16 Experimental setup of moisture detection system measuring moisture absorption in terms of cantilever deflection.

Table 7.3 Comparison of moisture sensing between our microcantilever and commercial microcantilever

Type of Cantilevers	Trial Number	Initial Value		Measure Value		Calculate the frequency change caused by the 1 PPM moisture (Hz/PPM)	
		Natural Resonance Frequency	Initial PPM	Resonance Frequency Shift	Time		
 (type 1)	1	35500	12	35250	6'50"	1.25	
	2	36625	20	36375	11'33"	1.25	
	3	36750	20	36500	8'05"	1.25	
 (type 2)	No.1	23875	40	23750	10'04"	0.625	
	No.2	1	24725	39	24525	9'25"	1
		2	24700	25	24500	28'10"	1
	No.3	1	24375	10	24250	12'40"	0.625
		2	20425	36	20325	17'40"	0.5

In fact, the spring constant for a cantilever is

$$k = \frac{Ewt^3}{4L^3} \quad (7.1)$$

where L , w and t is length, width and thickness of a cantilever, respectively, and E is Young's modulus of the cantilever. Therefore, the thickness of a cantilever plays an important role in the spring constant. In spite of the difference in the geometrical size between our fabricated microcantilever and the commercial samples, the former one has a larger spring constant due to its $2\mu\text{m}$ thickness in comparison with $1\mu\text{m}$ thickness of commercial samples. According to equation (2.1), the fabricated one has a higher resonant frequency and a relatively larger change in its resonant frequency under the same moisture condition.

CHAPTER EIGHT

CONCLUSION AND FUTURE WORK

8.1 Conclusions

The purpose of this research project was to establish a sensor platform based on the microcantilever to detect ultra-low moisture concentration. In an attempt to commercialize the device for moisture measurement, there are three steps that need to be taken. First of all, according to our existing optical readout system, it needs to be confirmed that the microcantilever is capable of detecting low moisture concentration 1-100 ppm. Due to its low spring constant, an SiO₂ microcantilever displays greater deflection and, thus, better sensitivity in chemical sensing compared to current commercially available microcantilevers. In order to fabricate the SiO₂ microcantilever, we developed a dry isotropic plasma etching process with ICP for a front-side released cantilever beam. The effects of chamber pressure, ICP plasma source power, substrate power, and SF₆ flow rate on the etch rate, undercut rate, and isotropic ratio had been investigated in this dissertation. This process was valuable for fabricating SiO₂ cantilever beams and releasing other suspended parts from the silicon substrate with high etch rate and good processing control. Both simulation and experimental results were applied to prove that the SiO₂ microcantilever can achieve higher sensitivity than the equivalent silicon microcantilever due to its lower Young's modulus. With coating Al₂O₃ on the beam surface, the SiO₂ microcantilever, operating in optical method, have been shown experimentally to detect moisture concentration levels at 30 ppm with not

only quick response time, high reproducibility and good recovery rate, but negligible interference from ethanol. Secondly, the readout method, which should be sensitive enough as well as easily integrated with IC technologies, needs to be selected for the microcantilever based moisture sensor. A large number of simulations and experiments were completed to compare piezoresistive, capacitive, MOSFET-Embedded and frequency readout methods. Eventually, the frequency mode was chosen, since both experimental and simulation results proved that the Al_2O_3 modified microcantilever possesses the ability to detect moisture at very low levels. Thirdly, the overall sensor system needs to be fabricated, tested and optimized. So far, the piezoelectric microcantilever, which vibrates at its resonant frequency upon applying an appropriate AC voltage and provides an electrical signal at the output via piezoelectric coupling, was fabricated as the platform for moisture sensing. Its resonant frequency shift is measured as 1.25 Hz/ppm, based on the experimental optical setup.

8.2 Future Work

8.2.1 Future Application of ICP Isotropic Dry Etching

In fact, combined with ICP anisotropic dry etching, ICP isotropic dry etching is able to be utilized not only for surface micromachining, but also for bulk micromachining. This microfabrication technique could also be developed to fabricate other MEMS devices, such as metal microcantilever, capacitive microcantilever, metal microbridge, etc. Next, we will discuss the basic probable fabrication steps for metal microcantilever and capacitive microcantilever.

8.2.1.1 Metal Microcantilever Fabrication

One major concern about the SiO_2 cantilever beam is that it is too vulnerable to damage to be worked in resonant mode as a mass sensor. In this case, the most

frequently used Ti-Ni shape memory alloy, which is not only superelastic but also biocompatible, is more likely to be chosen as an alternative beam material. Based on the fabrication techniques developed in our lab, the fabrication process can be demonstrated as follows (figure 8.1).

The starting material is also a commercially available [Silicon Inc.] double side polished four-inch (100-mm), <100> silicon wafer, 500 μm thick, and a 1 μm thick SiO_2 layer on both surfaces (figure 8.1 (A)). Next, LOR 7B and photoresist needs to be deposited and patterned before starting to do the lift-off process. Using a Co-sputtering technique, the Ti/Ni alloy, which consists of 44.4% Ti and 55.6% Ni, can be deposited on the front-side of the wafer (figure 8.1 (B)), the sputtering parameters for this deposition was described in detail by H. Takagi et al. [95]. According to H. Takagi et al. [95], the Ni-rich TiNi alloy film is able to change to a convex curvature, and has a very fast response to frequency change, thus becoming a prospective candidate for a number of MEMS applications. Using the lift-off process aforementioned in Section 5.2.3.2, we can pattern the Ti/Ni alloy film (figure 8.1 (C)). The SiO_2 layer can be patterned by BOE etching (figure 8.1 (D)). Afterwards, ICP isotropic dry etching would be applied to release the Ti/Ni alloy microcantilever beam from the bulk silicon (figure 8.1 (E)). ICP anisotropic dry etching could be employed to remove the leftover silicon from under the microcantilever beam (figure 8.1 (F)), the SiO_2 layer serves as a stop layer in this process. Eventually, the metal cantilever can be accomplished after etching the SiO_2 layer under the beam in the RIE machine using CF_4 and H_2 gas.

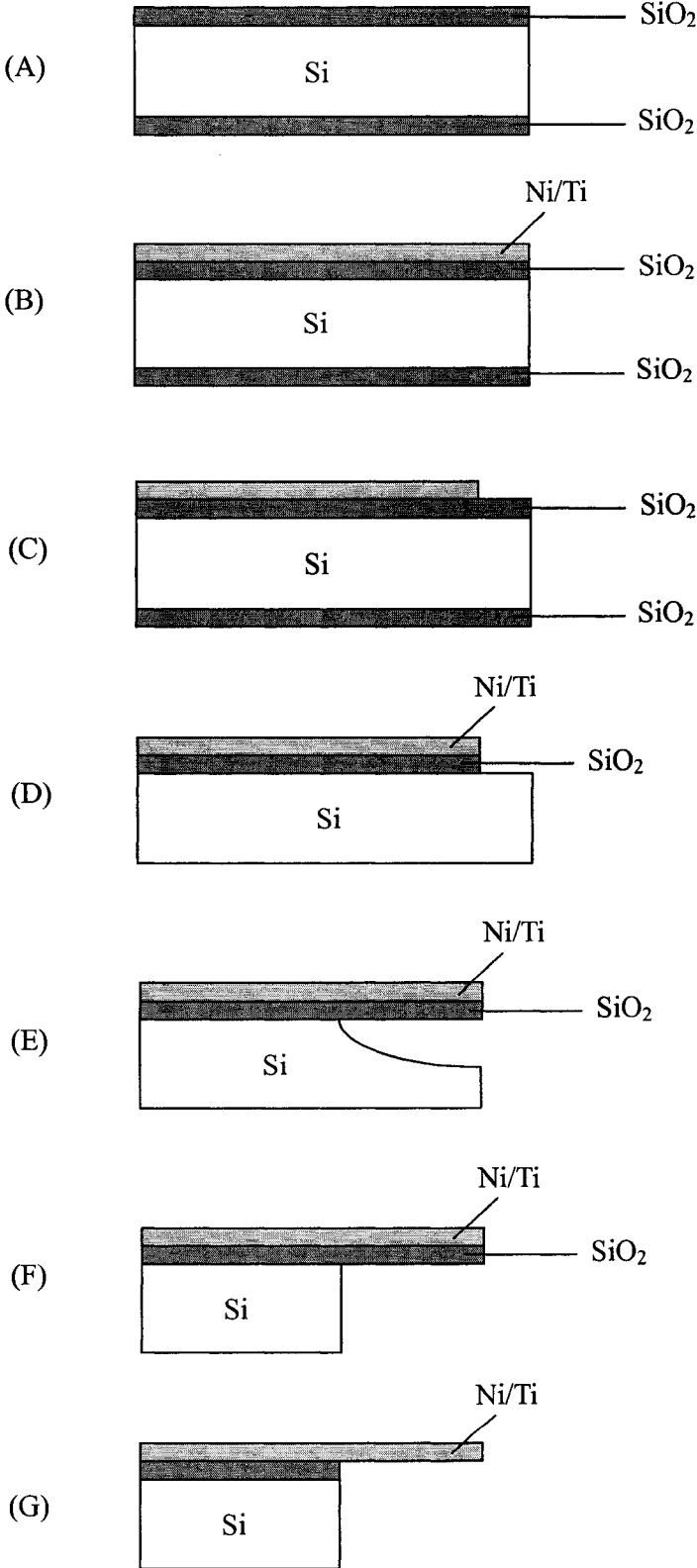


Figure 8.1 Fabrication process for Metal Microcantilever.

8.2.1.2 Capacitive Microcantilever Fabrication

The capacitance change of the parallel capacitor as function of beam deflection was simulated using ConvectorWare. The distance between cantilever beam and another parallel electrical plate is assumed to be 5 μ m. The simulation results were shown in Table 8.1, and the initial static capacitance was $C_0=5.046631e-2$ (pf). A linear increase of the change rate with increasing deflection of the microcantilever beam was observed in figure 8.2, which is consistent with the following equation:

$$C = \epsilon \frac{A}{d} \quad (8.1)$$

where C is the capacitance in farads, ϵ is the permittivity of the insulator used (or ϵ_0 for a vacuum), A is the area of each plate, measured in square metres, d is the separation between the plates, measured in metres. Actually, compared to the change rate in the resistance of the piezoresistive cantilever, which has already been presented previously, the capacitive microcantilever has a much larger change rate, thus it can offer higher sensitivity than the piezoresistive cantilever.

Table 8.1 Simulation results of capacitance microcantilever

Deflection(nm)	Capacitance (pf)	Capacitance Change
50	5.075378e-02	0.005696
100	5.098711e-02	0.0103196
150	5.122389e-02	0.0150116
200	5.146425e-02	0.0197744
250	5.170828e-02	0.02461
300	5.195607e-02	0.0295199

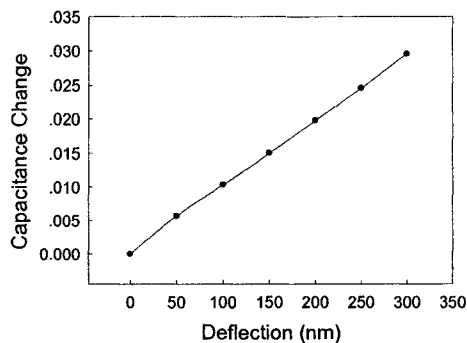


Figure 8.2 The change rate of capacitance as a function of deflection of microcantilever beam.

The fabrication process for the capacitive microcantilever is shown in figure 8.3. First of all, SiO_2 should be sputtered onto the wafer surface after the bottom metal (Au or Pt) electrode is patterned using the lift-off process (figure 8.3(A)). Secondly, we can deposit polysilicon as a sacrificial layer after patterning the SiO_2 layer (figure 8.3(B)). The top metal electrode is sputtered onto the surface of the wafer and patterned as a cantilever beam using the lift-off process (figure 8.3(C)). The polysilicon sacrificial layer is able to be removed by employing ICP isotropic dry etching, and both top and bottom electrodes are all released (figure 8.3(D)). ICP anisotropic dry etching should be utilized to remove the leftover bulk silicon underneath the bottom electrode beam (figure 8.3(E)). Taking wire bonding into account, a thin Al film can be deposited on the backside of microcantilever body (figure 8.3(F)).

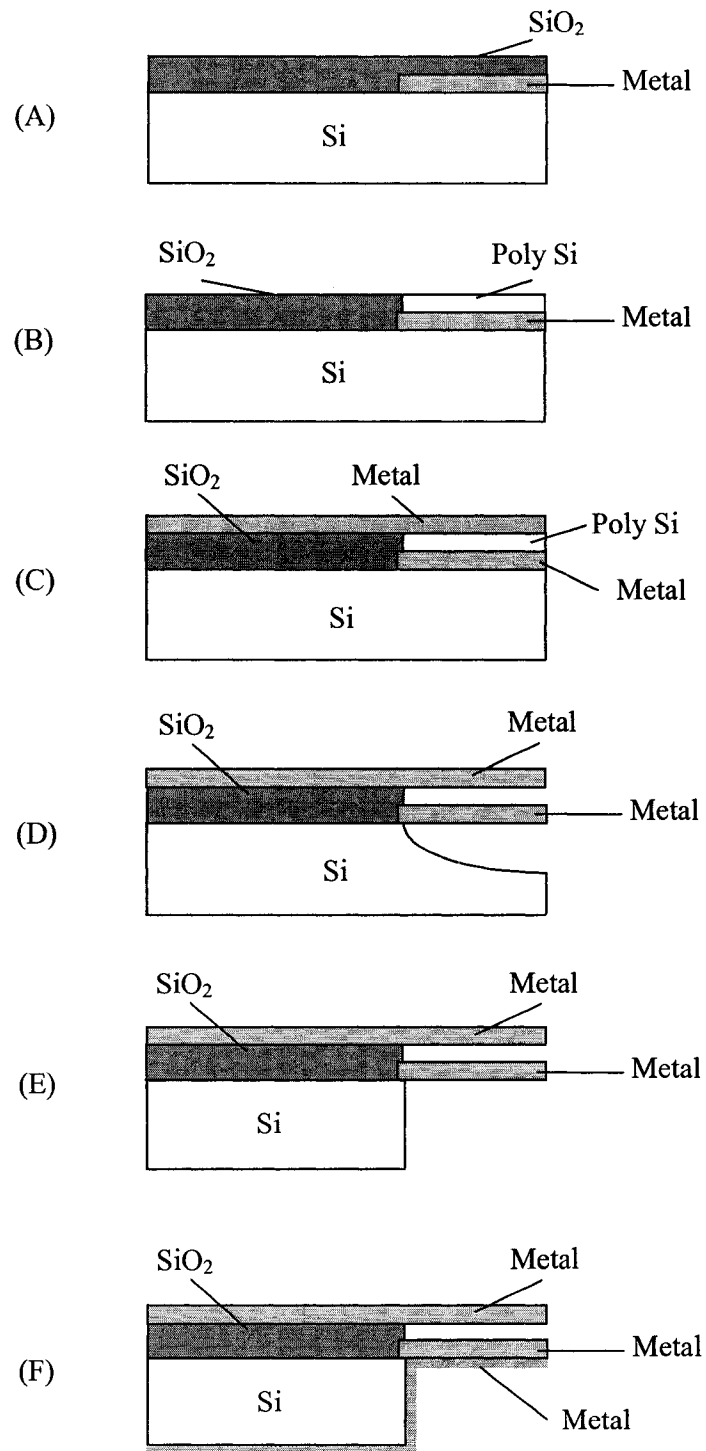


Figure 8.3 Fabrication process for capacitive microcantilever

8.2.2 Future Work of Moisture Sensor Project

Since the piezoelectric cantilevers that were fabricated in this project were only measured by an optical method in our lab, there are still some work that is needed to be done to develop portable cantilever moisture sensors for commercial purposes. The electrodes of the cantilevers need to be connected to the PCB board by wire bonding, and then the devices should be tested with a special phase shift circuit designed for actuation and feedback of the vibration of the piezoelectric microcantilever. In order to improve the sensitivity, one needs to search for a recipe to increase the aluminum anodization effect and, consequently, increase the moisture absorbing capacity. On the other hand, the thickness of cantilever beam will influence the resonant frequency shift with respect to any change in moisture level. Increasing the thickness of the cantilever beam would cause an increase in the natural resonant frequency and resonant frequency shift under certain moisture concentrations. Therefore, piezoelectric microcantilever with thicker beams is needed to be fabricated and tested in the near future. In addition, the quality and piezoelectricity of the ZnO thin film deposited by the sputtering system is required to be tested by X-Ray diffraction and a certain network analyzer.

If this sensor device works well, many different kinds of gas sensing system could be built up based on this moisture sensor system by just changing the modification material on the beam surface.

REFERENCE

- [1] T. J. Lechner-Fish, Electrolytic measurement of Moisture in Natural Gas, *Sensors Magazine*, September (1997).
- [2] Z. Chen & C. Lu, "Humidity Sensors: A Review of Materials and Mechanisms" *Sensor Letters* **3**, 274–295 (2005).
- [3] <http://www.specgasreport.com/archive/moisture602.htm>.
- [4] T. Maddanimath, I. S. Mulla & S. R. Sainkar, Humidity sensing properties of surface functionalized polyethylene and polypropylene films, *Sensors and Actuators, B*, **81**, 141-151 (2002).
- [5] M. Viviani, M. T. Buscaglia & L. P. Nanni, Barium perovskites as humidity sensing materials, *Journal of European Ceramic Society*, **21**, 1981-1984 (2001).
- [6] G. Y. Chen, T. Thundat, E. A. Wachter & R. J. Warmack, Adsorption-induced surface stress and its effects on Resonance frequency of microcantilevers, *Journal of Applied Physics*, **77**, 3618-3622 (1995).
- [7] P. I. Oden, P. G. Datskos & T. Thundat, Uncooled infrared imaging using a Piezoresistive microcantilever, *Appl. Phys. Lett.*, **69**, 3277-3279 (1996).
- [8] M. D. Chabot & J. Moreland, Micrometer-scale magnetometry of thin Ni-Fe films using ultra-sensitive microcantilevers, *J. Appl. Phys.*, **93**, 7897–7899 (2003).
- [9] T. Thundat, P. I. Oden & R. J. Warmack, Microcantilever sensors, *Microscale Thermophys. Eng.*, **1**, 185-199 (1997).
- [10] X. Xu, T. Thundat, G. M. Brown & H.-F. Ji, Detection of Hg²⁺ using microcantilever sensors, *Anal. Chem.*, **74**, 3611-3615 (2002).
- [11] H.-F. Ji, T. Thundat, R. Dabestani, G. M. Brown, P. F. Britt & P. V. Bonnesen, Ultrasensitive detection of CrO₄²⁻ using a microcantilever sensor, *Anal. Chem.*, **73**, 1572-1576 (2001).
- [12] K. M. Hansen, H.-F. Ji, G. Wu, R. Datar, R. Cote, A. Majumadar & T. Thundat, Cantilever-based optical deflection assay for discrimination of DNA single nucleotide mismatches, *Anal. Chem.*, **73**, 1567-1571 (2001).

- [13] G. Wu, H.-F. Ji, K. Hansen, T. Thundat, R. Datar, R. Cote, M. F. Hagan, A.K. Chakraborty & A. Majumdar, Nanomechanical signatures of biomolecular recognition and interactions, *Proc. Natl. Acad. Sci. U.S.A.*, **98**, 1560-1564 (2001).
- [14] H.-F. Ji & T. Thundat, Trace Ca^{2+} microcantilever sensor, *Biosens. Bioelectron.*, **17** 337-343 (2002).
- [15] P. Belaubre, M. Guirardel & G. Garcia, Fabrication of biological microarrays using microcantilevers, *Apply Physics Letters*, **82**, 3122-3124 (2003).
- [16] J. Fritz, M. K. Baller, H. P. Lang, H. Rothuizen, P. Vettiger, E. Meyer, H. Güntherodt, C. Gerber & J. K. Gimzewski, Translating biomolecular recognition into nanomechanics, *Science*, **288**, 316-318 (2000).
- [17] W. Y. Shih, X. P. Li & H. M. Gu, Simultaneous liquid viscosity and density determination with piezoelectric unimorph cantilevers, *J. Appl. Phys.*, **89**, 1497-1505 (2001).
- [18] P. I. Oden, P. G. Datskos & T. Thundat, Uncooled infrared imaging using a Piezoresistive microcantilever, *Appl. Phys. Lett.*, **69**, 3277-3279 (1996).
- [19] F. Quist & A. Badia, Nanomechanical cantilever motion generated by a Surface-confined Redox Reaction, *J. Phys. Chem. B*, **107**(39), 10691-10695 (2003).
- [20] C.-Y. Lee & G.-B. Lee, Micromachine-based humidity sensors with integrated temperature sensors for signal drift compensation, *J. Micromech. Microeng.*, **13**, 620-627 (2003).
- [21] A. C. Stephan, E. L. Finot, H.-F. Ji, T. Thundat, L. F. Miller & R. J. Warmack, Micromechanical Measurement of Active Sites on Silicon Nitride Using Free Surface Energy, *Ultramicroscopy*, **91**, 1-8 (2002).
- [22] J. Brugger, M. Despont, C. Rossel, H. Rothuizen, P. Vettiger & M. Willemin, Microfabricated Ultrasensitive Piezoresistive cantilevers for torque Magnetometry, *Sensors and Actuators, A*, **73**, 235-242, (1999).
- [23] R. D. Piner, J. Zhu, F. Xu, S. Hong & C. A. Mirkin, Dip-pen Nanolithography, *Science*, **283**, 661-663 (1999).
- [24] T. Thundat, S. Sharp & W. G. Fisher, Micromechanical Radiation Dosimeter, *Appl. Phys. Lett.*, **66**, 1563-1565 (1995).
- [25] G. Meyer & N. M. Amer, Novel optical approach to atomic force microscopy, *Appl. Phys. Lett.*, **53**(12), 1045-1047 (1988).
- [26] N. Lavrik, M. J. Sepaniak & P. G. Datskos, Cantilever transducers as a platform for chemical and biological sensors, *Rev. Sci. Instrum.*, **75**(7), 2229-2253 (2004).
- [27] J. Thaysen, A. Boisen, O. Hansen & S. Bouwstra, Atomic force microscopy probe with piezoresistive read-out and highly symmetrical Wheatstone bridge arrangement, *Sens. Actuators, A*, **83**, 47-53 (2000).

- [28] M. Yang, X. Zhang, K. Vafai & C. S. Ozkan, High sensitivity piezoresistive cantilever design and optimization for analyte-receptor binding, *J. Micromech. Microeng.*, **13**, 864-72 (2003).
- [29] R. Marie, H. Jensenius, J. Thaysen, C. B. Christensen & A. Boisen, Adsorption kinetics and mechanical properties of thiol-modified DNA-oligos on gold investigated by microcantilever sensors, *Ultramicroscopy*, **91**, 29-36 (2002).
- [30] <http://www.azonano.com/details.asp?ArticleID=1927>
- [31] S. Shin and J. Lee, Fabrication & Sensing Behavior of Ultrasensitive Piezoelectric Microcantilever-Based Precision Mass Sensor, *J. Korean Phys. Soc.*, **45**, 227 (2004).
- [32] G. Shekhawat, S.-H. Tark & V. Dravid, MOSFET-Embedded Microcantilevers for Measuring Deflection in Biomolecular Sensors, *Science*, **311**, 1592-1595, (2006).
- [33] Y. Tang, J. Fang, X. Yan & H. F. Ji, Fabrication and characterization of SiO₂ microcantilever for microsensor application, *Sensors and Actuators, B*, **97** 109-13 (2004).
- [34] M. H. Bao, *Micro mechanical transducers (Handbook of Sensors and Actuators)*, editor S. Middelhoek (Amsterdam: Elsevier) (2000).
- [35] <http://www.memsnet.org/material>
- [36] S. D. Senturia, *Microsystem Design*, Springer Science+Business Media, Inc (2001).
- [37] C. A. Klein, How accurate are Stoney's equation and recent modifications, *J. Appl. Phys.*, **88** 5487-5489 (2000).
- [38] L. B. Freund, J. A. Floro & E. Chason, Extensions of the Stoney formula for substrate curvature to configurations with thin substrates or large deformations, *Appl. Phys. Lett.*, **74** 1987-1989 (1999).
- [39] Y. Zhang, Q. Ren & Y. Zhao, Modelling an analysis of surface stress on a rectangular cantilever beam, *Journal of Physics D: Applied Physics* **37**, 2140-2145 (2004).
- [40] J. E. Sader, Surface stress induced deflections of cantilever plates with applications to atomic force microscope: rectangular plates, *J. Appl. Phys.*, **89**, 2911-2921 (2001).
- [41] T. Ivanov, T. Gotszalk, T. Sulzbach & I. W. Rangelow, Quantum size aspects of the piezoresistive effect in ultra-thin piezoresistors, *Ultramicroscopy*, **97**, 377-384 (2003).
- [42] J. L. Egley & D. Chidambarrao, Strain Effects on Device Characteristics: Implementation in Drift-Diffusion Simulators, *Solid-State Electronics*, **36**(12), 1653-1664 (1993).

- [43] G. L. Bir & G. E. Pikus, *Symmetry and Strain-Induced Effects in Semiconductors*, Wiley, New York (1974).
- [44] H. Mikoshiba, Stress-sensitive properties of silicon-gate MOS devices, *Solid-State Electron.*, **24**, 221–232 (1981).
- [45] T. Chen & Y. Huang, Evaluation of MOS devices as mechanical stress sensors, *IEEE Transactions on components and packaging technologies*, **25**(3), 511–517, (2002)
- [46] R. C. Jaeger, J. C. Suhling, R. Ramani, A. T. Bradley & J. Xu, CMOS stress sensors on (100) silicon, *IEEE journal of solid-state circuits*, **35**(1), 85–95, (2000).
- [47] S. Chatzandroulis, A. Tserepi, D. Goustouridis, P. Normand & D. Tsoukalas, Fabrication of single crystal Si Cantilevers using a dry release process and application in a capacitive-type humidity sensor. *Microelectronic Engineering*, **61-62**, 955–961 (2002).
- [48] http://www.adixen.com/adixen_avt/download/docs/news/doc114.pdf.
- [49] B. Bahreyni & C. Shafai, Investigation and simulation of XeF₂ isotropic etching of silicon, *J. Vac. Sci. Technol. A*, **20**, 1850–54 (2002).
- [50] M. J. Madou, *Fundamentals of microfabrication (The science of miniaturization)*, CRC press, (2002).
- [51] M. Boufnichel, S. Aachboun, F. Grangeon, P. Lefauchaux & P. Ranson, Profile control of high aspect ratio trenches of silicon. I. Effect of process parameters on local bowing, *J. Vac. Sci. Technol. B*, **20**(4), 1508 - 12 (2002).
- [52] M. Boufnichel, P. Lefauchaux, S. Aachboun, R. Dussart & P. Ranson, Origin control and elimination in silicon deep plasma etching in the cryogenic process, *Microelectronic Eng.*, **77**, 327–36 (2005).
- [53] R. D. Mansano, P. Verdonck, H. S. Maciel & M. Massi, Anisotropic inductively coupled plasma etching of silicon with pure SF₆, *Thin Solid Film*, **343-344**, 378–80 (1999).
- [54] S. Aachboun & P. Ranson, Deep anisotropic etching of silicon, *J. Vac. Sci. Technol. A*, **17**, 2270–73 (1999).
- [55] S. Aachboun, P. Ranson, C. Hibert & M. Boufnichel, Cryogenic etching of deep narrow trenches in silicon, *J. Vac. Sci. Technol., A*, **18**, 1848–52 (2000).
- [56] <http://web.utk.edu/~prack/MSE%20300/SEM.pdf>
- [57] F. Laermer & A. Schilp, *Method of anisotropically etching silicon*, US Patent 5501893 (1996).
- [58] F. Laermer, A. Schilp, K. Funk & M. Offenberger, Bosch deep silicon etching: improving uniformity and etch rate for advanced MEMS applications, *Technical*

Digest MEMS'99 (Florida, USA), 211-16 (1999).

- [59] E. Quevy, B. Parvais, J. P. Raskin, L. Buchaillet, D. Flander & D. Collard, A modified Bosch-type process for precise surface micromachining of polysilicon, *J. Micromech. Microeng.*, **12**, 328-33 (2002).
- [60] J. H. Min, G. R. Lee, J. K. Lee, & S. H. Moon, Angular dependence of etch rates in the etching of poly-Si and fluorocarbon polymer using SF₆, C₄F₈, and O₂ plasmas, *J. Vac. Sci. Technol. A*, **22**, 661-669 (2004).
- [61] F. Gaboriau, M. C. Peignon, G. Cartry, L. Rolland, D. Eon, C. Cardinaud & G. Turban, Langmuir probe measurements in an inductively coupled plasma: Electron energy distribution functions in polymerizing fluorocarbon gases used for selective etching of SiO₂, *J. Vac. Sci. Technol. A*, **20**, 919-927 (2002).
- [62] K. R. Williams & R. S. Muller, Etch rates for micromachining process, *IEEE Journal of Microelectromechanic Systems*, **5**, 256-269 (1996).
- [63] S. Frederico & C. Hibert, Silicon sacrificial layer dry etching (SSLDE) for free-standing RF MEMS architectures, *proceedings of the IEEE Micro Electro Mechanical Systems (MEMS)*, 570-73 (2003).
- [64] B. Kim, S. M. Kong & B. T. Lee, Modeling SiC etching in C₂F₆/O₂ inductively coupled plasma using neural networks, *J. Vac. Sci. Technol. A*, **20**, 146-52 (2001).
- [65] K. M. Robb, J. Hopkins, G. Nicholls & L. Lea, Plasma sources for high-rate etching of SiC, *Solid State Technology*, **48**, 61-64 (2005).
- [66] K.P. Larsen, J. T. Ravnkilde & O. Hansen, Investigations of the isotropic etch of an ICP source for silicon microlens mold fabrication, *J Micromech. Microeng.*, **15**, 873-82 (2005).
- [67] G. T. A. Kovacs, *Micromachined Transducers* (McGraw-Hill, New York, 1998).
- [68] A. K. Deisingh, MEMS technology in analytical chemistry, *Analyst* (Cambridge, U.K.) **128**, 9-11 (2003).
- [69] R. Maboudian, Surface processes in MEMS technology, *Surf. Sci. Rep.* **30**, 209-269 (1998).
- [70] J. Buhler, E. Fitzer & D. Kehre, The Rate Controlling Process in the Oxidation of Hot Pressed Silicon Nitride, *J. Electrochem. Soc.*, **124**, C299 (1977).
- [71] J. Buhler, F. P. Steiner & H. Baltes, Silicon dioxide sacrificial layer etching in surface micromachining, *J. Micromech. Microeng.* **7**, R1 (1997).
- [72] M. Madou, *Fundamentals of Microfabrication*, CRC Press, New York, (1997).
- [73] J. W. Gardner, V. K. Varadan & O. O. Awadelkarim, *Microsensors, MEMS and Smart Devices*, Wiley, New York, (2001).
- [74] P. Li & X. Li, A single-sided micromachined piezoresistive SiO₂ cantilever

- sensor for ultra-sensitive detection of gaseous chemicals, *Journal of Micromechanics and Microengineering*, **16**, 2539-2546, (2006).
- [75] P. Li, X. Li, G. Zuo, J. Liu, Y. Wang, M. Liu & D. Jin, Silicon dioxide microcantilever with piezoresistive element integrated for portable ultrasensitive gaseous detection, *Appl. Phys. Lett.*, **89**(7), 074104, (2006).
- [76] H.-J. Butt, A Sensitive Method to Measure Changes in the Surface Stress of Solids, *J. Colloid Interface Sci.*, **180**, 251 (1996).
- [77] M. J. McDonough, Device for water vapor & hydrocarbon dew point determination, *Proceedings of the International School of Hydrocarbon Measurement*, **75**, 512 (2000).
- [78] a) B. J. Mychajliw, Determination of hydrocarbon dew point in natural gas, *Proc. Internation. Sch. Hydrocarbon Measurement*, **79**, 111 (2004). b) B. J. Mychajliw, Devices for water vapor and hydrocarbon dew point determination in Natural Gas, *Proc. International School Hydrocarbon Measurement*, **78**, 501 (2003).
- [79] L.I. Berger, *Semiconductor Materials*, CRC Press, Boca Raton, (1997).
- [80] F.R. Blom, F.C.M. Van de Pol, G. Bauhuis & T.J.A. Popma, R.F. planar magnetron sputtered ZnO films II: Electrical properties, *Thin Solid Films*, **204**, 365-376 (1991).
- [81] W.E. Devaney, W.S. Chen, J.M. Stewart & R.A. Mickelsen, Structure and properties of high efficiency ZnO/CdZnS/CuInGaSe₂ solar cells, *IEEE Trans. Electron Devices*, **37**, 428-433 (1990).
- [82] F. S. Mahmood, R. D. Gould & M. H. Salih, D.C. properties of ZnO thin films prepared by r.f. magnetron sputtering, *Thin Solid Films*, **270**, 376-379 (1995).
- [83] C. R. Gorla, N. W. Emanetoglu, S. Liang, W. E. Mayo, Y. Lu, M. Wraback & H. Shen, Structural, optical, and surface acoustic wave properties of epitaxial ZnO films grown on (01 $\bar{1}$ 2) sapphire by metalorganic chemical vapor deposition, *J. Appl. Phys.*, **85**, 2595-2602 (1999).
- [84] Y. F. Chen, D. Bagnall & T. Yao, ZnO as a novel photonic material for the UV region, *Mater. Sci. Eng., B*, **75**, 190-198 (2000).
- [85] D.C. Look, Recent advances in ZnO materials and devices, *Mater. Sci. Eng., B*, **80**, 383-387 (2001).
- [86] M. Chen, Z.L. Pei, C. Sun, J. Gong, R.F. Huang & L.S. Wen, ZAO: an attractive potential substitute for ITO in flat display panels, *Mater. Sci. Eng., B*, **85**, 212 (2001).
- [87] B.S. Li, Y.C. Liu, Z.S. Chu, D.Z. Shen, Y.M. Lu, J.Y. Zhang & X.W. Fan, High quality ZnO thin films grown by plasma enhanced chemical vapor deposition, *J. Appl. Phys.*, **91**, 501-505 (2002).
- [88] M. J. Alam & D. C. Cameron, Preparation and properties of transparent

conductive aluminum-doped zinc oxide thin films by sol-gel process, *J. Vac. Sci. Technol., A*, **19**, 1642-1646 (2001).

- [89] A.J.C. Fiddes, K. Durose, A.W. Brinkman, J. Woods, P.D. Coates & A.J. Banister, Preparation of ZnO films by spray pyrolysis, *J. Cryst. Growth*, **159**, 210-213 (1996).
- [90] T. Ohgaki, N. Ohashi, H. Kakemoto, S. Wada, Y. Adachi, H. Haneda & T. Tsurumi, Growth condition dependence of morphology and electric properties of ZnO films on sapphire substrates prepared by molecular beam epitaxy, *J. Appl. Phys.*, **93**, 1961-1965 (2003).
- [91] Y.R. Ryu, S. Zhu, J.D. Budai, H.R. Chandrasekhar, P.F. Miceli & H.W. White, Optical and structural properties of ZnO films deposited on GaAs by pulsed laser deposition, *J. Appl. Phys.*, **88**, 201-204 (2000).
- [92] T. Minami, S. Ida & T. Miyata, High rate deposition of transparent conducting oxide thin films by vacuum arc plasma evaporation, *Thin Solid Films*, **416**, 92-96 (2002).
- [93] K.H. Kim, K.C. Park & D.Y. Ma, Structural, electrical and optical properties of aluminum doped zinc oxide films prepared by radio frequency magnetron sputtering, *J. Appl. Phys.*, **81**, 7764-7772 (1997).
- [94] Z. Li & W. Gao, ZnO thin films with DC and RF reactive sputtering, *Materials Letters*, **58**, 1363-1370 (2004).
- [95] H. Takagi, K. Okano, S. Juodkazis, S. Matsuo & H. Misawa, Two-Directional TiNi Shape Memory Alloy Film, *Advanced Engineering Materials*, **5**(10), 732-735, (2003)